ISSN 2587-1366

TUJE

TURKISH JOURNAL OF ENGINEERING

VOLUME 5 ISSUE 2 APRIL 2021

Dr. Ghazi DROUBI
Robert Gordon University Engineering Faculty
Scotland, UK

JOURNAL SECRETARY

Nida DEMİRTAŞ
nidademirtas@mersin.edu.tr

TURKISH JOURNAL OF ENGINEERING (TUJE)

Turkish Journal of Engineering (TUJE) is a multi-disciplinary journal. The Turkish Journal of Engineering (TUJE) publishes the articles in English and is being published 4 times (January, April, July and October) a year. The Journal is a multidisciplinary journal and covers all fields of basic science and engineering. It is the main purpose of the Journal that to convey the latest development on the science and technology towards the related scientists and to the readers. The Journal is also involved in both experimental and theoretical studies on the subject area of basic science and engineering. Submission of an article implies that the work described has not been published previously and it is not under consideration for publication elsewhere. The copyright release form must be signed by the corresponding author on behalf of all authors. All the responsibilities for the article belongs to the authors. The publications of papers are selected through double peer reviewed to ensure originality, relevance and readability.

AIM AND SCOPE

The Journal publishes both experimental and theoretical studies which are reviewed by at least two scientists and researchers for the subject area of basic science and engineering in the fields listed below:

Aerospace Engineering
Environmental Engineering
Civil Engineering
Geomatic Engineering
Mechanical Engineering
Geology Science and Engineering
Mining Engineering
Chemical Engineering
Metallurgical and Materials Engineering
Electrical and Electronics Engineering
Mathematical Applications in Engineering
Computer Engineering
Food Engineering

PEER REVIEW PROCESS

All submissions will be scanned by iThenticate® to prevent plagiarism. Author(s) of the present study and the article about the ethical responsibilities that fit PUBLICATION ETHICS agree. Each author is responsible for the content of the article. Articles submitted for publication are priorly controlled via iThenticate ® (Professional Plagiarism Prevention) program. If articles that are controlled by iThenticate® program identified as plagiarism or self-plagiarism with more than 25% manuscript will return to the author for appropriate citation and correction. All submitted manuscripts are read by the editorial staff. To save time for authors and peer-reviewers, only those papers that seem most likely to meet our editorial criteria are sent for formal review. Reviewer selection is critical to the publication process, and we base our choice on many factors, including expertise, reputation, specific recommendations and our own previous experience of a reviewer's characteristics. For instance, we avoid using people who are slow, careless or do not provide reasoning for their views, whether harsh or lenient. All submissions will be double blind peer reviewed. All papers are expected to have original content. They should not have been previously published and it should not be under review. Prior to the sending out to referees, editors check that the paper aim and scope of the journal. The journal seeks minimum three independent referees. All submissions are subject to a double blind peer review; if two of referees gives a negative feedback on a paper, the paper is being rejected. If two of referees gives a positive feedback on a paper and one referee negative, the editor can decide whether accept or reject. All submitted papers and referee reports are archived by journal Submissions whether they are published or not are not returned. Authors who want to give up publishing their paper in TUJE after the submission have to apply to the editorial board in written. Authors are responsible from the writing quality of their papers. TUJE journal will not pay any copyright fee to authors. A signed Copyright Assignment Form has to be submitted together with the paper.

PUBLICATION ETHICS

Our publication ethics and publication malpractice statement is mainly based on the Code of Conduct and Best-Practice Guidelines for Journal Editors. Committee on Publication Ethics (COPE). (2011, March 7). Code of Conduct and Best-Practice Guidelines for Journal Editors. Retrieved from http://publicationethics.org/files/Code%20of%20Conduct_2.pdf

PUBLICATION FREQUENCY

The TUJE accepts the articles in English and is being published 4 times (January, April, July and October) a year.

CORRESPONDENCE ADDRESS

Journal Contact: tuje@mersin.edu.tr

CONTENTS

Volume 5 – Issue 2

ARTICLES

Turkish Journal of Engineering

Turkish Journal of Engineering (TUJE)
Vol. 5, Issue 2, pp. 51-61, April 2021
ISSN 2587-1366, Turkey
DOI 10.31127/tuje.669566
Research Article

CLASSIFICATION OF UAV POINT CLOUDS BY RANDOM FOREST MACHINE LEARNING ALGORITHM

Mustafa Zeybek *[1]

[1] Artvin Coruh University, Engineering Faculty, Geomatics Engineering, Artvin, Turkey
ORCID ID 0000-0001-8640-1443
mzeybek@artvin.edu.tr

* Corresponding Author
Received: 02/01/2020 Accepted: 07/03/2020

ABSTRACT
Today, unmanned aerial vehicle (UAV)-based images have become an important data sources for researchers who deals with mapping from various disciplines on photogrammetry and remote sensing. Reconstruction of an area with three-dimensional (3D) point clouds from UAV-based images are an essential process to be used for traditional 2D cadastral maps or to produce a topographic maps. Point clouds should be classified since they subjected to various analyses for extraction for further information from direct point cloud data. Due to the high density of point clouds, data processing and gathering information makes the classification of point clouds a challenging task and may take a long time. Therefore, the classification processing allows an optimal solution to acquire valuable information. In this study, random forest machine learning algorithm for classification processing is applied with radiometric features (Red band, Green band and Blue band) and geometric characteristics derived from covariance feature (curvature, omnivariance, flatness, linearity, surface variance, anisotropy and normalized terrain surface) of points. In addition, the case study is presented in order to test applicability of the proposed methodology to acquire an accuracy and performance of random forest method on the UAV based point cloud. After the classification processing, a class assigned each point from the model was compared with the reference data class. Lastly, the overall accuracy of the classification was achieved as 96% and the Kappa index was reached to 91% on data set.

Keywords: *Unmanned aerial vehicle, point cloud, classification, random forest.*

1. INTRODUCTION

Three-dimensional (3D) high spatial accuracy point cloud has become an important data source for various disciplines such as urban planning, simulation, mapping, visualization, and emergency response. Satellite-based methods, aerial camera and laser systems and terrestrial methods are used in the production of these models (Pandey *et al.*, 2019). The area size is very important criteria. Larger area requires a greater number of quantified persons which leads more cost and labour force.

Difficulties arise in the production of traditional 2D urban maps from unmanned aerial vehicle (UAV) data, especially due to the existence of complex structures. So, it is difficult to obtain information from 3D dense point cloud data. One of the basic processing in solving these problems is classification of point clouds (Özbay, 2016; Zeybek and Şanlıoğlu, 2019a).

Over the last decade UAV map production systems have become an important technology for different disciplines (Akgül et al., 2016; Öztürk et al., 2017; Ulvi, 2018; A. Ulvi and Toprak, 2016; Ali Ulvi et al., 2020). The main reason for the spread of this system is the availability of flight platforms and technology for civilian users, as well as reductions in costs. Moreover, the high resolution and density of the data allow to use the data in analyses that can be adapted for different purposes for researchers and civilian users. Besides easy access to 3D data, problems have arisen in processing intensive data and to extract necessary information (Karakaş, 2018). The classification procedures play a vital role for solving these problem (Zeybek and Şanlıoğlu, 2019a).

In addition to UAV systems, airborne (ALS) and terrestrial (TLS) based LiDAR applications are widely for mapping purposes used (Canaz Sevgen, 2019; Demir, 2015). Laser scanning devices, global navigation satellite system (GNSS) and inertial measurement unit (IMU) sensors are synchronized systems that integrated on the moving (MLS) platforms, such as aircraft, helicopters and satellites. Point cloud densities vary according to the altitude and flight speed of the platform to the ground surface. However, acquired data still requires classification processing for map production.

In general, each point in the point clouds obtained with a LiDAR system contain several information such as incidence angle, slope distance, and intensity values (Shan and Toth, 2018). Laser signal intensity has been used in various applications such as classification of natural and built materials, urban pavement surfaces, determination of snow covered areas, soil and rock properties, coastal, land cover and flood modelling, road and road marking extractions (Kashani et al., 2015). The surface type can be recognised using the reflected laser signal intensity, i.e. the measure of the return signal strength (Yadav and Singh, 2017). On the other hand, a considerable research group worked on the development of various filtering methods for classification of LiDAR point clouds such as interpolation-based (Kraus and Pfeifer, 1998), slope-based (Vosselman, 2000), segmentation-based (Tóvári and Pfeifer, 2005) and morphological (K. Q. Zhang et al., 2003).

Multispectral LIDAR, which is a new remote sensing technology is able to measure both spectral and spatial information simultaneously and has proven to be usable method in various fields today (Chen et al., 2017; de Almeida et al., 2019; Gong et al., 2012; Guyot et al., 2019; Luo et al., 2019; Niu et al., 2015; Pan et al., 2018). The first commercial aerial multispectral LiDAR, Optech Titan (532, 1,064 and 1,550 nm), has been brought new advantageous to the multispectral LiDAR land cover classification process (Wichmann et al., 2015).

It is stated that the filtering methods produce effective results bot only for LIDAR data classification but also UAV data classification (Zeybek and Şanlıoğlu, 2019a). In addition, new approaches and methods have been proposed constantly (Şahin et al., 2018). It is possible to classify point clouds by utilizing of the geometrical properties as well as multispectral band properties. Machine learning and deep learning algorithms have been also used to classification of dense point cloud data (Özdemir and Remondino, 2019).

Depending on the application, supervised and unsupervised classification approaches are proposed (Zou et al., 2017), and all approaches are based on descriptive characteristics. Some well-known image processing techniques were applied for classification purposes by examining the geometric properties on the 3D point cloud data (K. Q. Zhang et al., 2003).

The Markov random field (MRF) classifier was used for power line and building classification using the local linear and planar characteristics of points in city model data acquired from ALS for classification (Sohn et al., 2012).

In some paper, multi-source optical image and LiDAR data features for urban scene classification has been studied (Guo et al., 2011). Hyperspectral imaging in individual tree detection with UAV based classifications were also investigated (Nevalainen et al., 2017). Niemeyer et al. (2014) proposed a context-based conditional random forest classification method for urban LiDAR point clouds. Çömert et al. (2019) studied the performance of the random forests algorithm for mapping of burned forest areas from remotely sensed images.

In this article, Random Forest (RF) classification algorithm on 3D dense UAV point clouds have been investigated for classification feasibility and accuracy for urban area.

2. MATERIAL AND METHOD

The proposed methodology consists of three steps; automatic classification of each point with the machine learning algorithm RF, utilizing radiometric and geometric properties for point clouds. The general workflow of the proposed methodology is given in Fig. 1.

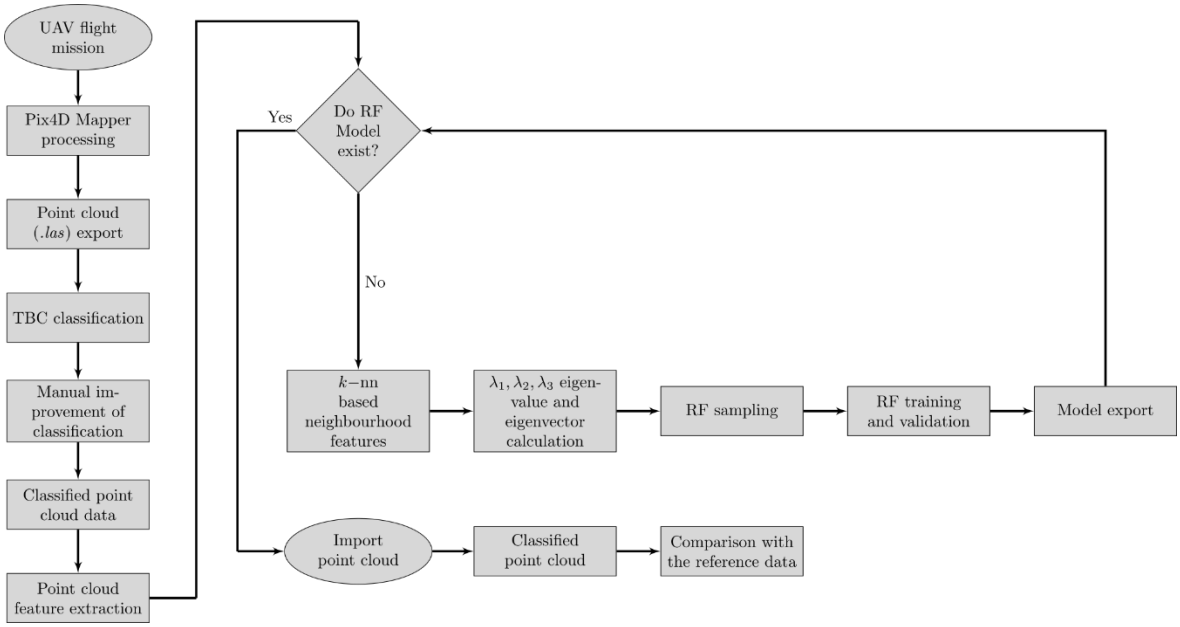

Fig. 1. General work flow chart

2.1. Study Area

Artvin Coruh University Seyitler Campus has been selected as the study area. The total surveyed area is 87.2641 ha. The boundaries of the study area are in the range of latitude (41.8440,41.8560) and longitude (41.1940, 41.2100). The average ellipsoidal height (GRS80) value is around 567 m. Details of the study area are given in Fig. 2.

Several major buildings (Engineering, and Vocational school and Rectorate) and President's Office are located in the study are. The general topographic structure of Artvin is rugged. However, the study area has a flat topographic feature.

2.2. UAV Point Cloud

2D images were acquired from the UAV platform to produce the UAV point cloud.

UAV platform used in this study was Phantom 4 RTK brand and model 4 motorized. Thanks to the real-time kinematics (RTK) system, which is one of the main features of the UAV platform, images are obtained directly in georeferenced. In the EXIF information, global navigation satellite system (GNSS) information is integrated in detail. Therefore, ground control point (GCP) is not mandatory or third-party data processing software is not required for georeferencing purposes.

PIX4DMapper software was used in this study, which is a commercial software and commonly used for image processing. (https://www.pix4d.com/). This software package with an easy-to-use interface consists of two stages to produce dense point cloud. The first stage is a keypoint image feature extraction process which is similar to scale invariant feature transform (SIFT) (Lowe, 2004). Algorithm identifies the specific points in each image with similar structure for allowing the images to match image pairs corresponding these keypoints (Alignment) (Zeybek and Şanlıoğlu, 2019b). After the image matching stage, the camera calibration optimization step is performed to update the camera parameters to improve the estimation of lens distortion parameters with physical lens properties.

The next processing stage is the dense point matching, whereby the point clouds are densified by starting similar location or point matching operations on the images whose camera location and orientation parameters are calculated. In this stage the density of the points are increased which leads accurate representation of the surface. A more dense and accurate surface model is produced when compared to the sparse point clouds.

2.3. Random Forest Classifier

Breiman (2001) proposed a new approach, which is called random forest (RF) classification algorithm, by adding a layer of randomness to the bagging method. It is very easy to use since only two parameters the number of variables in the random subgroup of each node and the number of trees in the forest) are required. In addition, the RF classification algorithm is not sensitive to outliers.

It is an ensemble tree-based learning algorithm. The RF classifier contains set of decision trees in a subset of a randomly selected training set. For decision-making, the final class of the test object is given aggregated votes from different decision trees (Akar and Güngör, 2012; Canaz Sevgen, 2019; Ok et al., 2011). This algorithm is preferred in this study because the classification accuracy is higher than most other decision trees.

The basic working principle of the random forest algorithm is as follows (Ramasubramanian and Singh, 2017),

1. Several inputs are required in this algorithm such as number of observations (N), number of decision three (ntree) and number of variables in the dataset (M). Users can select number of decision three (ntree) input then other two inputs are selected automatically by algorithm.
2. A subset of the number of predictors sampled for splitting at each node (mtry) (Kuhn, 2008; Liaw and Wiener, 2002) variable is selected from M,

where mtry << M and a random set of mtry variables are created in the decision tree,

3. Each tree should be as large as possible,
4. The majority vote is used to assign the class of observation.

To form each decision tree, a randomly selected subset of N observations is used without any changes (normally 2/3). For more stable models and accurate generation of variable importance estimations, a large number of trees (ntree) is recommended. However, large number of trees (ntree) leads more memory and longer processing times. For small data sets, 50 trees may be sufficient, while larger data sets may require 500 or more. Therefore, parameter tuning can be made in the field using trial and error (Cutler et al., 2007). There is a wide discussion in the literature about the effect of mtry and ntree parameters. It is also reported that models of different mtry values do not affect the correct classification rates and other performance metrics are fixed under different mtry values (Cutler et al., 2007).

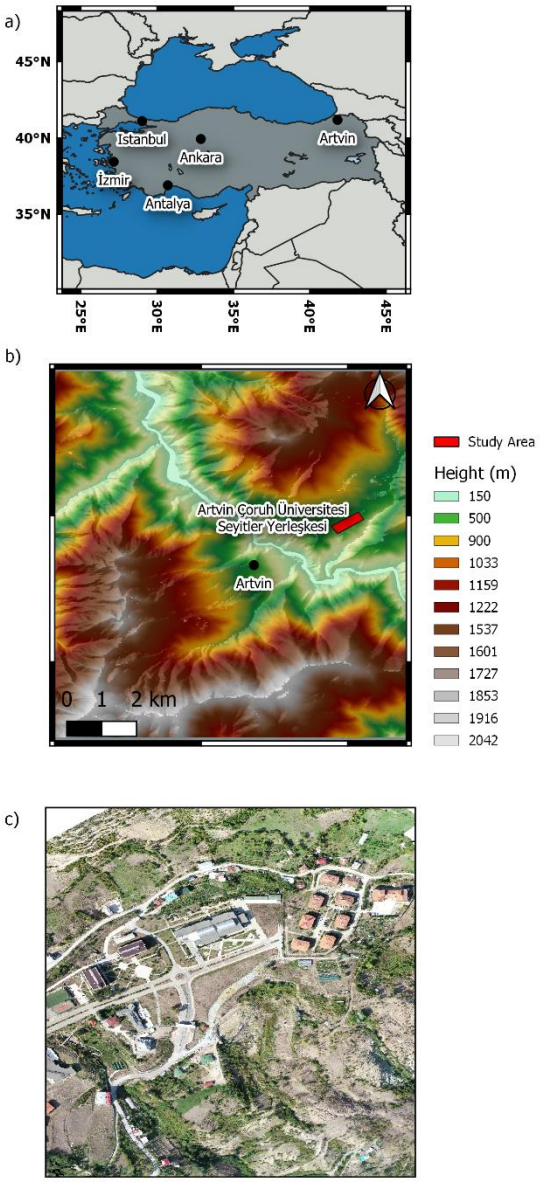

Fig. 2. Study area, a) location of Artvin province, b) height values of Artvin region, c) orthomosaic image of the study area

The first step for the generation of the RF model is the preparation of training data. In the creation of reference data, which is also known as ground-truth data, manual classification is performed in a specific field. The number of classes should be determined according to the relevant field characteristics. In this study, the relevant area was divided into 3 different classes namely, ground, vegetation and building classes.

The geometric characteristics of the points representing to these classes were calculated with the help of eigenvalues and eigenvectors according to the covariance matrix in k-nearest neighbourhood (*k-nn*) criteria and values (Blomley *et al.*, 2014; Canaz Sevgen, 2019; Hackel *et al.*, 2017; Taşcı and Onan, 2016).

Ground points at the point cloud were determined using a cloth simulation filtering (CSF) algorithm (W. M. Zhang et al., 2016). The digital terrain model (DTM) was created with the ground points. The distance of the non-ground points to the DTM surface was calculated. Thus, the normalized feature, which is also known as above ground level (AGL) is computed.

Calculated geometric and radiometric thirteen different features, which is used to produce the model with the highest accuracy for reference data, have been created. Hence, a classifier model is produced which can be adapted to the whole area or different study area.

For the RF model training, 20000-point sample data that including all classes were used for learning stage. The sample data was partitioned as 70% and 30% for training and validation stage, respectively.

The RF models are various, and the algorithm randomly selects the mtry variables from the set of available estimators when creating each node in a tree. Therefore, while creating a node, a different set of random variables in which is presenting the best separation point is selected. Since there are thirteen variables, thirteen random mtry values are examined. The number of trees (ntree) is commonly considered as 500 in the classification studies. The parameters specified for the RF classifier are left to the user's preference. However, it is known that it does not affect accuracy after certain values (Ok et al., 2011).

2.4. Accuracy Assessment Criteria

Accuracy analysis in the classification of point cloud shows the consistency between the reference data class and the model based assigned class of each point. Reference data classification was done with point clouds classification module using the Trimble Business Center (TBC) commercial software. After the reference classification, cross-sectional analyses were performed with the help of the operator, and improvements were obtained in the classification. Thus, the comparison with the model classification was made more accurately.

Accuracy assessment procedure is performed to determine the classification accuracy of the model produced by RF based on the reference data. The process is the statistical evaluation of each point in the point cloud after the RF model classification by comparing it with reference class.

The commonly used statistical methods in accuracy

evaluations are relative values obtained according to error matrix (confusion matrix, contingency table) (Çetinkaya and Toz, 2007). Error matrices show the correlation between reference data from binary or more classes and model classification results (Table 1).

Table 1. Error matrix

		Reference	
		Class 1	Class 2
Model	Class 1	A	B
	Class 2	C	D

The quality of classification accuracy is based on the values calculated from the error matrix (Table 1) and the criteria given in Eq. (1)-(11).

$$Sensivity = A / (A + C) \quad (1)$$

$$Specificity = D / (B + D) \quad (2)$$

$$Prevalence = (A + C) / (A + B + C + D) \quad (3)$$

$$PPV = (Sensivity * Prevalence) / ((Sensivity * Prevalence) + ((1\text{-}Specificity) * (1\text{-}Prevalence))) \quad (4)$$

$$NPV = (Specificity * (1 - Prevalence))) / \begin{pmatrix} ((1 - Sensivity) * Prevalence) + \\ ((Specificity) * (1 - Prevalence)) \end{pmatrix} \quad (5)$$

$$Detection\ Rate = A / (A + B + C + D) \quad (6)$$

$$Detection\ Prevalence = (A + B) / (A + B + C + D) \quad (7)$$

$$Balanced\ Accuracy = (Sensitivity + Specificity) / 2 \quad (8)$$

$$Precision = A / (A + B) \quad (9)$$

$$Recall = A / (A + C) \quad (10)$$

$$F1 = (1 + beta^2) * Precision * Recall / ((beta^2 * Precision) + Recall) \quad (11)$$

In Eq. (11), beta was set as 1.

2.5. Implementation

Pix4DMapper commercial software was used to convert UAV images to point clouds. Then, Open-source CloudCompare (CloudCompare, 2013) for visualization, R Programming language (Team, 2019) for RF application and commercial TBC software were used for analysis on point clouds. A prototype framework was developed for the proposed RF-based point cloud classification method using R programming language.

3. RESULTS AND DISCUSSIONS

Totally 142 images were taken in the study area and 23155722 three-dimensional point data were generated (Fig. 3). The flight height was approximately 200 m which was suitable with the topographic rugged terrain and the ground sampling interval was obtained as 5.93 cm.

RTK system on the platform was connected to Continuously Operating Reference Station (Cors-TR) network. Thus, the images were directly geolocated without using any ground control point. The root mean square errors for X, Y, Z coordinates were 1.3 cm, 1.4 cm and 1.4 cm, respectively. The GNSS positional errors for the camera locations are given in Fig. 3 and the distributions in Fig. 4. The generated dense point cloud was georeferenced in the TUREF / TM42 (EPSG:5258) coordinate system. The point density was obtained as 12 points/m^3. This value can be increased in SfM software. However, in general, the density values where obtained in this study provide to draw traditional map with accuracy standards. The distance between the points is set at 10 cm in order to provide pattern of the point cloud and improve the data processing performance. As a result, 20294012-point data was processed.

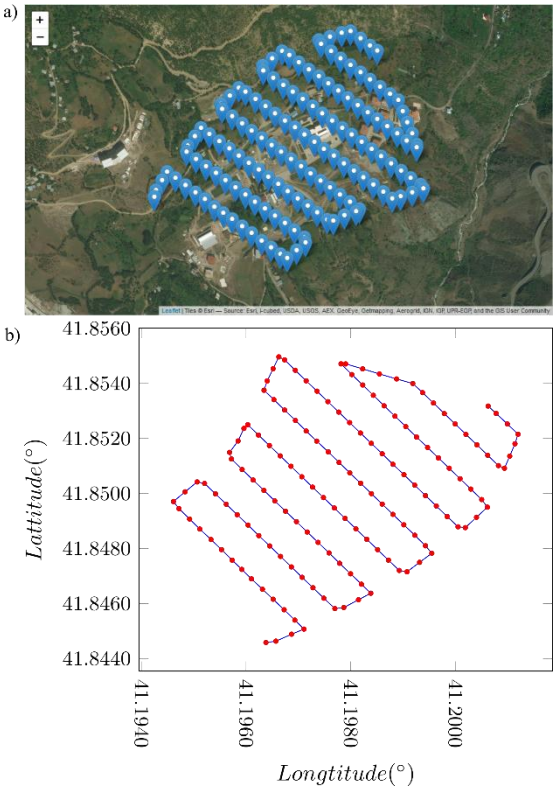

Fig. 3. Camera locations according to the GNSS coordinate (WGS 84) in the EXIF data a) camera locations on Leaflet satellite image and b) camera locations on map (red dots: indicating camera locations on WGS-84 coordinate system)

In the study, the test area was determined for the RF model to evaluate the effectiveness of the applied methodology.

Classification of the reference data set was automatically classified using the TBC point cloud module (Fig. 5). The TBC uses the default settings and the geometry between points when extracting ground points. This avoids a long trial and error process, especially for the observations involving noisy and outlier points in a point cloud. This feature is effective on rough ground or dense vegetation areas because more than one iteration can eliminate more noisy points. It also saves time for users who are only interested in ground points, such as contour maps production from ground points. It classifies buildings, trees, power transmission lines and poles based on similar geometric features in above ground points. Due to the commercial software, the evaluation of parameters and algorithms related to classification is limited. Exported point clouds were obtained in *las* format.

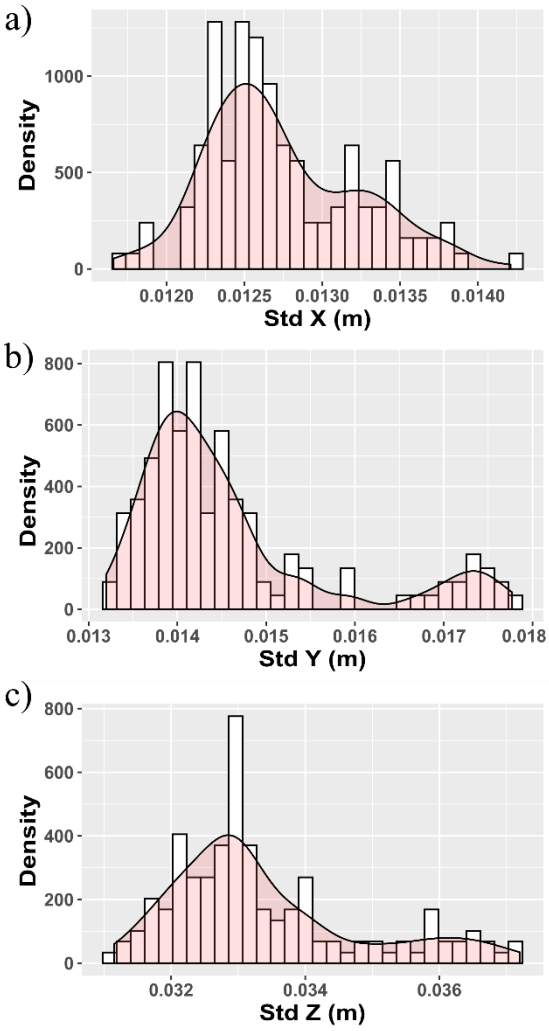

Fig. 4. GNSS RMSE's for camera locations a) X-axis direction, b) Y-axis direction and c) Z-axis direction.

According to the American Society for Photogrammetry and Remote Sensing (ASPRS), classification fields are standardized in the point cloud file format *las* extension as ground points class to 2, vegetation points class to 5 and building points class to 6. This file format is designed to contain records of point cloud data from LiDAR or different sensors. Point cloud data is usually converted to this format from software that combines GPS, IMU and laser signal information to generate X, Y and Z point coordinates. The main purpose of the data format is to provide an open format that allows different LiDAR hardware and software tools to input or output data in a common format (ASPRS, 2019).

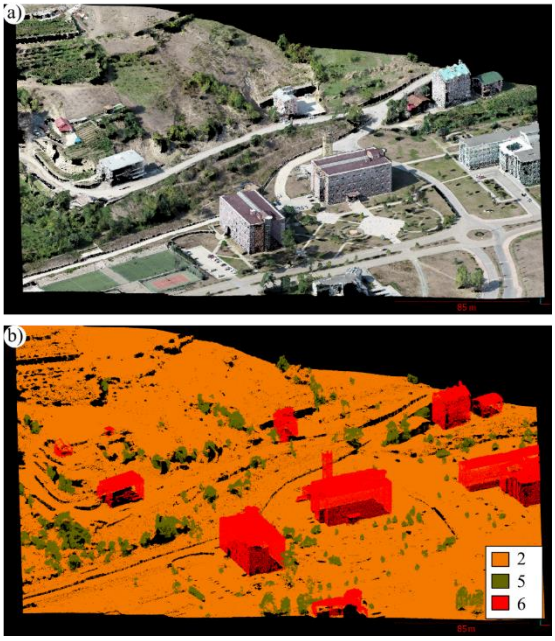

Fig. 5. Reference data classification on TBC software a) view of dense point cloud in RGB band values, b) automatic classified and manually corrected point cloud classes by TBC (ground:2, vegetation:5 and building:6)

After automatic classification, classification quality was improved by manual correction. This process was performed again with the help of TBC sectioning at cross-sectional intervals of 5 m (Fig. 6).

In the R programming language, the *lidR* package was used to read the *las* file format without corruption. With the *readLAS* function, the path where the *las* file is located was determined and the required fields were selected and imported. This function supports the LAS formats 1.1 to 1.4 (Roussel and Auty, 2017). An imported file stored in LAS object which inherits from a spatial object from sp package (Bivand *et al.*, 2008). Since there will be applications related to the neighbourhood relations, a certain number of neighbourhood distances must be calculated for each point. For this purpose, considering the dense point clouds, a fast distance calculation should be applied. The *nn2* function included in the *RANN* package has been implemented in this application (Arya *et al.*, 2019).

In the machine learning step, parallel computation has been applied to use the hardware performances at high capacity for intensive training process. The *makeCluster* function included in the *parallel* package uses multiple

processors to solve problems. Simultaneous training and calculations are divided into different parts. In this way, each part is divided into different command series and the given commands are run on different processors at the same time.

The *CreateDataPartition* function included in the *caret* package (Kuhn, 2008) is used to create balanced partitions of the training data that will be used to create the model. The class value is evaluated as a factor data type at the result of this function in R. Random sampling takes place within each class, and the overall class distribution of the data is preserved. The RF model is trained with 20000 points obtained from the reference data, which includes all classes for classification.

In this study, a k-fold CV was used to randomly split the training dataset into k parts, and then each of the k parts evaluated as a test dataset for the trained model in the other k-1. The average of k error is calculated for all evaluated parts. Then k-fold CV was repeated 3 times. In order to determine the model accuracy criteria, the k-fold cross-validation was performed and the k value was taken as 10. *trainControl* function was used for this implementation.

The *predict* function was applied for the estimation of new data of the parameters obtained from the results of RF model fitting functions. The *predict* function performs predictions by calling certain methods that depend on the class of the first data object.

Cross tabulation of classes observed and estimated with related statistics was calculated with the *confusionMatrix* function.

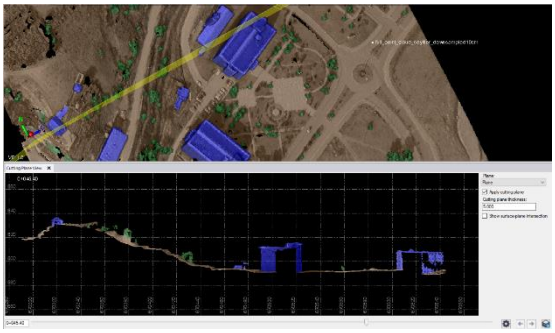

Fig. 6. Improvement on the automated classified reference data by means of sections and operator

The resulted accuracy values in the sub-groups were obtained. The obtained maximum accuracy values were calculated for each group. The number of variables available for division in each tree node was randomly calculated for thirteen different variables (Table 2). The mtry value was taken as 10 because it produces the optimum model accuracy at 10. The accuracy of the classification with the various mtry feature variable is differed by approximately 1%. Without the normalizing geometric and radiometric features, RF classifier model produced the 96% overall accuracy. The most applicable or "true" value for the ntree is not usually very unstable, because it is clear that the predictions from the model are not change much after a certain number of trees.

After the verification process is completed and the accuracy criteria are met, the produced RF model must be stored. The ".rds" file was used to save and load a single R object, which is the RF model, to a link (usually a file) for later use in various data. This process provides to store a more model parameters with specific format than just saving and reading parameter lists. For the produced model, ".rds" file extension is used. *saveRDS* and *readRDS* functions are used to save and read the files in ".rds".

Table 2. Model accuracy values for RF model subsets (* mtry subset variable number)

*mtry	Accuracy	Kappa
1	0.9500038	0.8846614
2	0.9537180	0.8932820
3	0.9570273	0.9009979
4	0.9593365	0.9063616
5	0.9607650	0.9096831
6	0.9614077	0.9111628
7	0.9623363	0.9132596
8	0.9632884	0.9154454
9	0.9634072	0.9157523
10	0.9635027	0.9159197
11	0.9631454	0.9151173
12	0.9629550	0.9146240
13	0.9625026	0.9135558

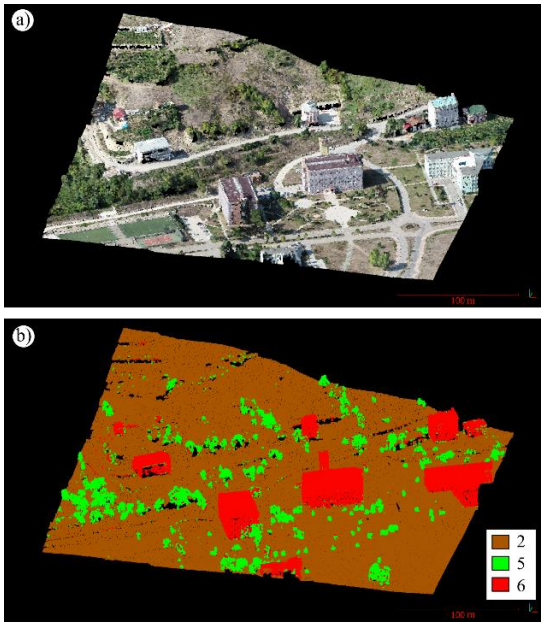

Fig. 7. The classification obtained as a result of RF classifier, a) point clouds indicated by RGB bands, b) point clouds classified according to RF model (ground:2, vegetation:5 and building:6)

The method applied to calculate the importance of the variables used for the objects produced by methods specific to train and method was made with the *varImp* function. When the importance levels of neighbourhood-related covariance characteristics were examined, the most important parameter was the above ground level (AGL) (Fig. 8). Radiometric B band and vertical directional surface normal value were also other two parameters that are important classifier features. AGL

was the only topographic feature that helps to distinguish between ground and surface classes. Another important feature can be explained to be effective in determining the above-ground points.

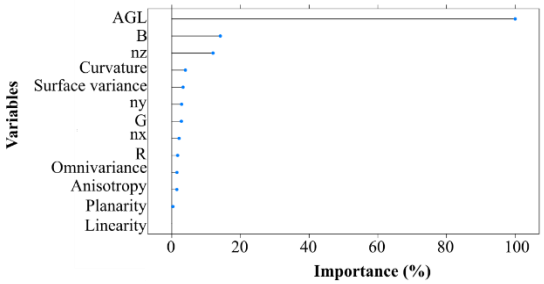

Fig. 8. Importance ratios of covariance and radiometric properties evaluated in RF model.

RF classifier has been performed to distinguish between three class. A confusion matrix summarized the results of the RF classifier algorithm for further inspection. The confusion matrix are presented in Table 3. According to the confusion matrix, defective points are more likely in ground and vegetation classes. For the vegetation class, it is found that the 3D UAV points are not sufficiently detailed, due to they have a ground-like feature at the peaks of the trees and also the ground points could not be reconstructed from the leaves and branches of the trees as the main reasons for these errors. In addition, the presence of steep slopes prevents sharp curves between the ground and trees. In this context, tree points become the point feature that ensures the continuity of the ground points.

Statistical validation criteria on the test area are given in Table 4 regarding section 2.4. It is found that it is difficult to classify small plants especially close to the ground. Therefore, small vegetation points often complicated for 3D data. As a result, vegetation points in confusion matrices are classified as ground points and reduced the classification accuracy of other classes. The RF classification framework and obtained parameters of RF produce an overall accuracy of 0.96, and a Kappa coefficient of 0.91.

During the classification, some of the common errors encountered the detection of planar points near the ground. Moreover, high points of the vegetation was classified as ground points, and the results of some decreases in accuracy values due to errors such as the scattering characteristic of on building facades. In order to avoid such errors and increase the accuracy values, it is necessary to reduce the noise points, to optimize the better neighbouring values expressing the surface characteristics and to improve the clustering analysis.

Table 3. Error matrix (confusion)

		Reference data (Class)		
		2	**5**	**6**
Model data (Class)	**2**	4269	93	45
	5	50	565	34
	6	11	30	902

Table 4. Classification statistical metrics

	Class		
	2	**5**	**6**
Sensitivity	0.9882	0.82887	0.9287
Specificity	0.9311	0.98574	0.9908
PPV	0.9738	0.87994	0.9526
NPV	0.9682	0.97857	0.9859
Precision	0.9738	0.87994	0.9526
Recall	0.9882	0.82887	0.9287
F1	0.9810	0.85364	0.9405
Prevalence	0.7220	0.11200	0.1660
Detection rate	0.7135	0.09283	0.1542
Detection prevalence	0.7327	0.10550	0.1618
Balanced accuracy	0.9596	0.90730	0.9598

When investigating the error source, it is significant whether the errors are occurred inly model-based or irregularities in point clouds and systematic errors. While the geometric properties of dense point clouds are detected in certain areas of measurement errors, it is almost impossible to detect for irregular objects (trees, vegetation near the ground etc.). Different studies are required to examine and eliminate these details. These errors in this study have not been studied.

Studies on the classification of point clouds can be applied to increase RF model classifier performances and accuracy criteria in parallel with the robust algorithms developed in future periods. Robust methods can be developed that are more optimized for geometric features and are not affected by the density changes of the points. However, some confusion computation stages and time may increase in the calculated point features. For this, optimization and hardware requirements may increase. Different results are produced according to different studies and examples (Canaz Sevgen, 2019; Nevalainen et al., 2017). Overall accuracy value is obtained as 96% in this study. For instance, when looking at the accuracy criteria in other studies, the accuracy values obtained are close and high accuracy. Kim and Sohn (2012) achieved a result of the experiment, 93.9% with RF model.

R codes containing the methods applied in this article can be examined and used freely from the link https://github.com/mzeybek583/PCL-RandomForest-Classification.

5. CONCLUSIONS

The random forest machine learning algorithm has a comprehensive adaptability in the industry and in many research studies. Decision tree-based designs make it easier to interpret the model and the result, while intuitively approaching actual classification problems, increasing the correct estimation rate. To compare the proposed methodology directly with different methods, point clouds of similar structure and application parameters are needed. However, the adequacy of the model can be tested more accurately by applying the generated RF model of the obtained point clouds from different areas.

It has been shown in this study that UAV based dense

point clouds can be classified according to their geometric characteristics and radiometric features. Although high accuracy values are obtained, there may still be incorrect classification points in some areas of the data. Therefore, it is necessary to improve this classification data with the help of operators after automatic classification. Further studies should be conducted to increase the accuracy model and improve its performance with robust feature estimation.

ACKNOWLEDGEMENTS

We would like to acknowledge the financial support of Artvin Coruh University Scientific Research Projects Coordinatorship for the project number "2019.F40.02.02"

REFERENCES

Akar, Ö., Güngör, O. (2012). Rastgele orman algoritması kullanılarak çok bantlı görüntülerin sınıflandırılması. *Jeodezi ve Jeoinformasyon Dergisi*. doi: 10.9733/jgg.241212.1t

Akgül, M., Yurtseven, H., Demir, M., Akay, A. E., Gülci, S., Öztürk, T. (2016). İnsansız hava araçları ile yüksek hassasiyette sayısal yükseklik modeli üretimi ve ormancılıkta kullanım olanakları. *İstanbul Üniversitesi Orman Fakültesi Dergisi, 66*(1). doi:10.17099/jffiu.23976

Arya, S., Mount, D., Kemp, S., Jefferis, G. (2019). RANN: Fast nearest neighbour search (wraps ANN library) using l2 metric. *R package version 2.6, 1*.

ASPRS. (2019). *LAS Specification 1.4 - R14*. Retrieved from http://www.asprs.org/wp-content/uploads/2019/03/LAS_1_4_r14.pdf

Bivand, R. S., Pebesma, E. J., Gomez-Rubio, V., Pebesma, E. J. (2008). *Applied spatial data analysis with R* (Vol. 747248717): Springer.

Blomley, R., Weinmann, M., Leitloff, J., Jutzi, B. (2014). Shape distribution features for point cloud analysis – a geometric histogram approach on multiple scales. *ISPRS Annals of Photogrammetry, Remote Sensing and Spatial Information Sciences, II-3*, 9-16. doi:10.5194/isprsannals-II-3-9-2014

Breiman, L. (2001). Random forests. *Machine learning, 45*(1), 5-32.

Canaz Sevgen, S. (2019). Airborne Lidar Data Classification in Complex Urban Area Using Random Forest: A Case Study of Bergama, Turkey. *International Journal of Engineering and Geosciences*. doi:10.26833/ijeg.440828

Chen, B., Shi, S., Gong, W., Zhang, Q., Yang, J., Du, L., Sun, J., Zhang, Z., Song, S. (2017). Multispectral LiDAR Point Cloud Classification: A Two-Step Approach. *Remote Sensing, 9*(4), 373. doi:10.3390/rs9040373

CloudCompare. (2013). Telecom ParisTech (version 2.4) [GPL software]. EDF R&D. Retrieved from http://www.danielgm.net/cc/

Cutler, D. R., Edwards, T. C., Jr., Beard, K. H., Cutler, A., Hess, K. T., Gibson, J., Lawler, J. J. (2007). Random forests for classification in ecology. *Ecology, 88*(11), 2783-2792. doi:10.1890/07-0539.1

Çetinkaya, B., Toz, G. (2007). Coğrafi veri seçim işlemi sonuçlarının değerlendirilmesinde hata matrisinin kullanımı. *İTÜDERGİSİ/d, 6*(5-6), 59-68.

Çömert, R., Küçük Matci, D., Avdan, U. (2019). Object Based Burned Area Mapping with Random Forest Algorithm. *International Journal of Engineering and Geosciences, 4*(2), 78-87. doi:10.26833/ijeg.455595

de Almeida, C. T., Galvao, L. S., Aragao, L. E. D. E., Ometto, J. P. H. B., Jacon, A. D., Pereira, F. R. D., Sato, L. Y., Lopes, A. P., Graca, P. M. L. D., Silva, C. V. D., Ferreira-Ferreira, J., Longo, M. (2019). Combining LiDAR and hyperspectral data for aboveground biomass modeling in the Brazilian Amazon using different regression algorithms. *Remote Sensing of Environment, 232*. doi:10.1016/j.rse.2019.111323

Demir, N. (2015). Görüntü ve LiDAR verisinden bina tespitinde farklı yöntemler. *HAVACILIK VE UZAY TEKNOLOJİLERİ DERGİSİ, 8*(1), 55-65.

Gong, W., Song, S. L., Zhu, B., Shi, S., Li, F. Q., Cheng, X. W. (2012). Multi-wavelength canopy LiDAR for remote sensing of vegetation: Design and system performance. *ISPRS Journal of Photogrammetry and Remote Sensing, 69*, 1-9. doi:10.1016/j.isprsjprs.2012.02.001

Guo, L., Chehata, N., Mallet, C., Boukir, S. (2011). Relevance of airborne lidar and multispectral image data for urban scene classification using Random Forests. *ISPRS Journal of Photogrammetry and Remote Sensing, 66*(1), 56-66. doi:10.1016/j.isprsjprs.2010.08.007

Guyot, A., Lennon, M., Thomas, N., Gueguen, S., Petit, T., Lorho, T., Cassen, S., Hubert-Moy, L. (2019). Airborne Hyperspectral Imaging for Submerged Archaeological Mapping in Shallow Water Environments. *Remote Sensing, 11*(19). doi:10.3390/rs11192237

Hackel, T., Wegner, J. D., Schindler, K. (2017). Joint classification and contour extraction of large 3D point clouds. *ISPRS Journal of Photogrammetry and Remote Sensing, 130*, 231-245. doi:10.1016/j.isprsjprs.2017.05.012

Karakaş, G. (2018). *Lidar Nokta Bulutu Verisi ve Yüksek Çözünürlüklü Ortofotolar Kullanarak Bina Çıkarımı İçin Bir Yaklaşım.* Fen Bilimleri Enstitüsü,

Kashani, A. G., Olsen, M. J., Parrish, C. E., Wilson, N. (2015). A Review of LIDAR Radiometric Processing: From Ad Hoc Intensity Correction to Rigorous

Radiometric Calibration. *Sensors, 15*(11), 28099-28128. Retrieved from https://www.mdpi.com/1424-8220/15/11/28099 https://res.mdpi.com/d_attachment/sensors/sensors-15-28099/article_deploy/sensors-15-28099-v2.pdf

Kim, H. B., Sohn, G. (2012). Random Forests Based Multiple Classifier System for Power-Line Scene Classification. *ISPRS - International Archives of the Photogrammetry, Remote Sensing and Spatial Information Sciences, XXXVIII-5/W12*, 253-258. doi:10.5194/isprsarchives-XXXVIII-5-W12-253-2011

Kraus, K., Pfeifer, N. (1998). Determination of terrain models in wooded areas with airborne laser scanner data. *ISPRS Journal of Photogrammetry and Remote Sensing, 53*(4), 193-203. doi:10.1016/S0924-2716(98)00009-4

Kuhn, M. (2008). Building predictive models in R using the caret package. *Journal of Statistical Software, 28*(5), 1-26.

Liaw, A., Wiener, M. (2002). Classification and regression by randomForest. *R news, 2*(3), 18-22.

Lowe, D. G. (2004). Distinctive Image Features from Scale-Invariant Keypoints. *International Journal of Computer Vision, 60*(2), 91-110. doi:10.1023/b:Visi.0000029664.99615.94

Luo, L., Wang, X. Y., Guo, H. D., Lasaponara, R., Zong, X., Masini, N., Wang, G. Z., Shi, P. L., Khatteli, H., Chen, F. L., Tariq, S., Shao, J., Bachagha, N., Yang, R. X., Yao, Y. (2019). Airborne and spaceborne remote sensing for archaeological and cultural heritage applications: A review of the century (1907-2017). *Remote Sensing of Environment, 232*. doi:10.1016/j.rse.2019.111280

Nevalainen, O., Honkavaara, E., Tuominen, S., Viljanen, N., Hakala, T., Yu, X. W., Hyyppa, J., Saari, H., Polonen, I., Imai, N. N., Tommaselli, A. M. G. (2017). Individual Tree Detection and Classification with UAV-Based Photogrammetric Point Clouds and Hyperspectral Imaging. *Remote Sensing, 9*(3). doi:10.3390/rs9030185

Niemeyer, J., Rottensteiner, F., Soergel, U. (2014). Contextual classification of lidar data and building object detection in urban areas. *ISPRS Journal of Photogrammetry and Remote Sensing, 87*, 152-165. doi:10.1016/j.isprsjprs.2013.11.001

Niu, Z., Xu, Z. G., Sun, G., Huang, W. J., Wang, L., Feng, M. B., Li, W., He, W. B., Gao, S. (2015). Design of a New Multispectral Waveform LiDAR Instrument to Monitor Vegetation. *Ieee Geoscience and Remote Sensing Letters, 12*(7), 1506-1510. doi:10.1109/Lgrs.2015.2410788

Ok, A. Ö., Akar, Ö., Güngör, O. (2011). *Rastgele Orman Sınıflandırma Yöntemi Yardımıyla Tarım Alanlarındaki Ürün Çeşitliliğinin Sınıflandırılması.* Paper presented at the TUFUAB 2011 VI. Teknik Sempozyumu.

Özbay, E. (2016). Nokta bulutu verilerinden nesne ayırt etme/Distinguishing objects on point cloud data. *Afyon Kocatepe Üniversitesi Fen Ve Mühendislik Bilimleri Dergisi, 16*(Özel Sayı), 128 - 136.

Özdemir, E., Remondino, F. (2019). Classification pf Aerial point clouds with deep learning. *International Archives of the Photogrammetry, Remote Sensing & Spatial Information Sciences*.

Öztürk, O., Bilgilioğlu, B. B., Çelik, M. F., Bilgilioğlu, S. S., Uluğ, R. (2017). İnsanız Hava Aracı (İHA) Görüntüleri İle Ortofoto Üretiminde Yükseklik Ve Kamera Açısının Doğruluğa Etkisinin Araştırılması. *Geomatik, 2*(3), 135-142. doi:10.29128/geomatik.327049

Pan, Y. F., Zhang, X. F., Cervone, G., Yang, L. P. (2018). Detection of Asphalt Pavement Potholes and Cracks Based on the Unmanned Aerial Vehicle Multispectral Imagery. *Ieee Journal of Selected Topics in Applied Earth Observations and Remote Sensing, 11*(10), 3701-3712. doi:10.1109/Jstars.2018.2865528

Pandey, P. C., Koutsias, N., Petropoulos, G. P., Srivastava, P. K., Ben Dor, E. (2019). Land use/land cover in view of earth observation: data sources, input dimensions, and classifiers-a review of the state of the art. *Geocarto International*. doi:10.1080/10106049.2019.1629647

Ramasubramanian, K., Singh, A. (2017). *Machine learning using R*: Springer.

Roussel, J.-R., Auty, D. (2017). lidR: Airborne LiDAR Data Manipulation and Visualization for Forestry Applications. *(https://github.com/Jean-Romain/lidR).*

Shan, J., Toth, C. K. (2018). *Topographic Laser Ranging and Scanning*.

Sohn, G., Jwa, Y., Kim, H. B. (2012). Automatic Powerline Scene Classification and Reconstruction Using Airborne Lidar Data. *ISPRS Annals of Photogrammetry, Remote Sensing and Spatial Information Sciences, I-3*, 167-172. doi:10.5194/isprsannals-I-3-167-2012

Şahin, B., Güzel, C., Baş, S., Türker, M. (2018). *3DETECTOR-LIDAR nokta bulutu verisinden otomatik ağaç konumu belirleme sistemi.* Paper presented at the VII. Uzaktan Algılama-CBS Sempozyumu, Eskisehir.

Taşcı, E., Onan, A. (2016). K-en yakın komşu algoritması parametrelerinin sınıflandırma performansı üzerine etkisinin incelenmesi. *Akademik Bilişim*.

Team, R. C. (2019). R: A Language and Environment for Statistical Computing In *R Foundation for Statistical Computing* (Vol. Vienna, Austria).

Tóvári, D., Pfeifer, N. (2005). Segmentation based robust interpolation-a new approach to laser data filtering. *International Archives of Photogrammetry, Remote Sensing and Spatial Information Sciences, 36*(3/19), 79-84.

Ulvi, A. (2018). Analysis of the Utility of the Unmanned Aerial Vehicle (Uav) in Volume Calculation by Using Photogrammetric Techniques. *International Journal of Engineering and Geosciences*. doi:10.26833/ijeg.377080

Ulvi, A., Toprak, A. S. (2016). Investigation of Three-Dimensional Modelling Availability Taken Photograph of the Unmanned Aerial Vehicle; Sample of Kanlidivane Church. *International Journal of Engineering and Geosciences*, *1*(1), 1-7. Retrieved from <Go to ISI>://WOS:000439136300001

Ulvi, A., Yakar, M., Yiğit, A. Y., Kaya, Y. (2020). İha ve Yersel Fotogrametrik Teknikler Kullanarak Aksaray Kızıl Kilisenin 3b Modelinin Ve Nokta Bulutunun Elde Edilmesi. *Geomatik*, *5*(1), 22-30. doi:10.29128/geomatik.560179

Vosselman, G. (2000). Slope Based Filtering Of Laser Altimetry Data. *Arch. Photogramm. Remote Sens., 3*, 935–942.

Wichmann, V., Bremer, M., Lindenberger, J., Rutzinger, M., Georges, C., Petrini-Monteferri, F. (2015). Evaluating the Potential of Multispectral Airborne Lidar for Topographic Mapping and Land Cover Classification. *Isprs Geospatial Week 2015*, *Ii-3*(W5), 113-119. doi:10.5194/isprsannals-II-3-W5-113-2015

Yadav, M., Singh, A. K. (2017). Rural Road Surface Extraction Using Mobile LiDAR Point Cloud Data. *Journal of the Indian Society of Remote Sensing*. doi:10.1007/s12524-017-0732-4

Zeybek, M., Şanlıoğlu, İ. (2019a). Point cloud filtering on UAV based point cloud. *Measurement*, *133*, 99-111. doi:10.1016/j.measurement.2018.10.013

Zeybek, M., Şanlıoğlu, İ. (2019b). Topoğrafik Yüzey Değişimlerinin Görüntü İşleme Teknikleriyle Belirlenmesi Üzerine Bir Araştırma. *Doğal Afetler ve Çevre Dergisi*, *5*(2), 350-367.

Zhang, K. Q., Chen, S. C., Whitman, D., Shyu, M. L., Yan, J. H., Zhang, C. C. (2003). A progressive morphological filter for removing nonground measurements from airborne LIDAR data. *IEEE Transactions on Geoscience and Remote Sensing*, *41*(4), 872-882. doi:10.1109/Tgrs.2003.810682

Zhang, W. M., Qi, J. B., Wan, P., Wang, H. T., Xie, D. H., Wang, X. Y., Yan, G. J. (2016). An Easy-to-Use Airborne LiDAR Data Filtering Method Based on Cloth Simulation. *Remote Sensing*, *8*(6), 501. doi:10.3390/rs8060501

Zou, X., Cheng, M., Wang, C., Xia, Y., Li, J. (2017). Tree classification in complex forest point clouds based on deep learning. *Ieee Geoscience and Remote Sensing Letters*, *14*(12), 2360-2364.

Turkish Journal of Engineering

Turkish Journal of Engineering (TUJE)
Vol. 5, Issue 2, pp. 62-68, April 2021
ISSN 2587-1366, Turkey
DOI 10.31127/tuje.672888
Research Article

INVESTIGATION OF EFFICIENCY OF R717 REFRIGERANT SINGLE STAGE COOLING SYSTEM AND R717/R744 REFRIGERANT CASCADE COOLING SYSTEM

Ahmet Erhan, Akan *[1], Fatih, Ünal [2] and Derya Burcu, Özkan [3]

[1] Namık Kemal University, Çorlu Vocational School, Machinery and Metal Technologies, Tekirdağ, Turkey
ORCID ID 0000-0003-1806-7943
aeakan@nku.edu.tr

[2] Mardin Artuklu University, Mardin Vocational School, Machinery and Metal Technologies, Mardin, Turkey
ORCID ID 0000-0001-6660-9984
funal81@hotmail.com

[3] Yildiz Technical University, Mechanical Engineering, İstanbul, Turkey
ORCID ID 0000-0002-8964-3015
tumer@yildiz.edu.tr

* Corresponding Author
Received: 09/01/2020 Accepted: 02/03/2020

ABSTRACT
This study is an adaptation of ammonia cascade cooling systems using carbon dioxide on ice cream production machines and includes thermodynamic analysis of R717/R744 cascade refrigeration system with R717 refrigerant single-stage refrigeration system and investigation of its efficiency. As a result of the analyses, the COP value of the single-stage system was 3.67, the Carnot efficiency was 0.57, the second law efficiency was 0.19 and the power required to operate the compressor was 27.55 kW. In the cascade cooling system, the COP value was 4.46, the Carnot efficiency 0.59 and the compressor power 22.7 kW in the high-temperature part, while the COP value was measured as 14.65, the Carnot efficiency 0.58 and the compressor power 6.4 kW in the low-temperature part. For the whole cascade system, the COP 3.24 and the second law efficiency were found to be 0.43. When the results were compared, it was concluded that although the COP value of the cascade cooling system was 0.43 points lower than the single-stage ammonia system, when our country's climate conditions and the thermophysical properties carbon dioxide gas were considered together, one of the most suitable designs was the cascade cooling system.

Keywords: *Cooling, Cascade systems, Refrigerant, Efficiency, Thermodynamic analysis.*

1. INTRODUCTION

Ice cream is known as a popular nutrient for people because of its superior nutritional value, easy digestion, popular taste, aroma and refreshing effect. Today, the ice cream industry is developing rapidly. In this study, ice cream production processes to be examined are shown in Figure 1.

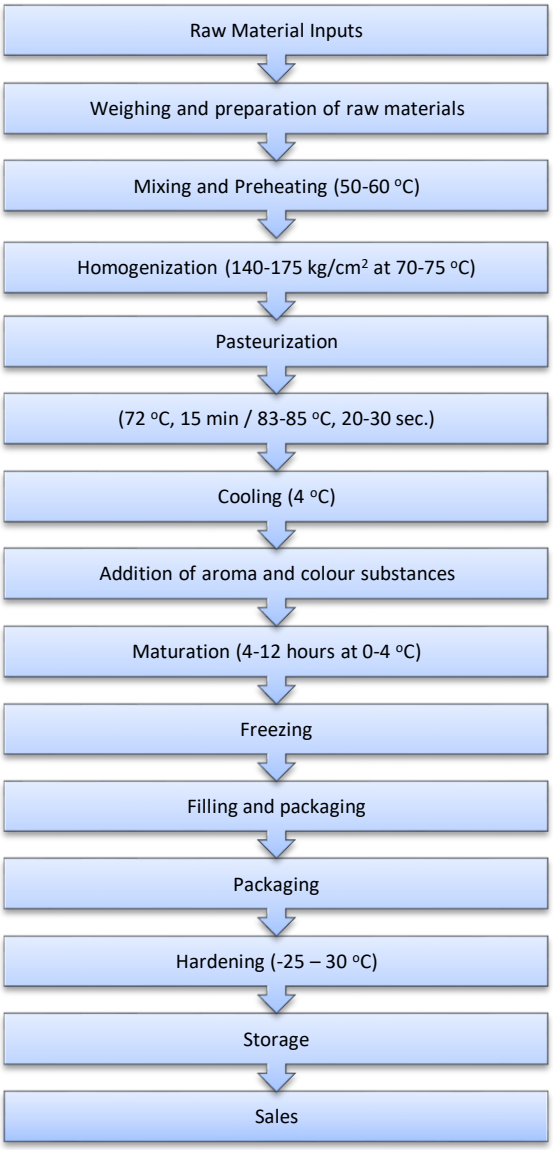

Fig. 1. Schematic representation of industrial ice cream production process

The mixture, which has matured, must be frozen in special machines in order to become freeze. The function of freezing is to freeze some of the water in the mixture. The freezing temperature varies depending on the type of freezer and the composition of the mixture but is generally between -3.5°C and -5.5°C. The freezing process is the most important stage of industrial ice cream production. However, this process needs to be studied in terms of energy consumption and efficiency. As an alternative to the single-stage mechanical compression cooling system used in the freezing process, cascade cooling systems can be preferred. The cascade cooling systems are suitable for use in industrial applications, especially in the supermarket refrigeration industry, where the evaporation temperature of frozen food cabinets varies from -30ºC to -50ºC (Getu et al., 2007). Prepare your manuscript and illustrations in appropriate format, according to the instructions given below. Please also be sure that your paper conforms to the scientific and style instructions of the Journal, given below here.

When the studies in the literature on cascade cooling systems examined;

Dopazo et al., (2009), analyzed a CO_2/NH_3 cascade cooling system and determined the optimum CO_2 condensation temperature from the energy and exergy perspectives. The effects of operating parameters on the performance of a CO_2/NH_3 cascade cooling system were experimentally investigated by Bingming et al. (Bingming et al., 2009). The researchers observed that the COP value of the system was only slightly sensitive to the degree of overheating, but also was greatly affected by the temperature, evaporation, and condensation of the temperature differences in the graded heat exchanger. Dopazo et al., (2011), experimentally evaluated the CO_2/NH_3 cascade cooling system in an industrial freezer with an evaporation temperature of -50ºC. They also investigated the effect of operating parameters on system performance and compared the results of common NH_3 two-stage cooling systems under the same operating conditions. They found that the COP of the cascade system had about 20% higher COP than a two-stage ammonia system with economizer and intercooler. Rezayan et al, (2011), developed a thermo economic optimization for a simple CO_2/NH_3 cascade cooling system without considering environmental analysis. They also investigated the effect of design parameters on the total annual cost of the system where ambient temperature, cooling capacity, and cold space temperature were limited. Ozyurt et al., (2016), conducted a thermodynamic analysis of the cooling system operating under two-stage and subcritical conditions using R717 (ammonia) in the high-temperature cycle and R744 (carbon dioxide) in the low-temperature cycle in their study. They carried out energy and exergy analyses in order to improve the optimum working conditions, performance coefficient and the efficiency of the second law in the cascade condenser of the cooling system and each equipment. By calculating the mass, energy, and exergy equations of the cascade cooling system, they calculated the optimum cascade condenser temperature. Moreover, researchers showed that increasing the evaporation temperature, superheating value, and super cooling value had a positive effect on the performance coefficient value. In a master's study, which was conducted by Alan (2011), the energy-saving potential of the two-stage overcritical CO_2 cycle was theoretically examined. Evaporator and gas cooler pressures were taken with variable parameters and how the performance coefficient is affected in the case of expansion turbines instead of the expansion valve was observed.

As can be seen from the aforementioned researches, studies are being carried out to find environmentally compatible refrigerant solutions instead of chlorofluorocarbons (CFC) and hydro chlorofluorocarbons (HCFC) which are used in cooling systems that accelerate global warming, have harmful effect to the ozone layer, and have a negative impact on the environment. Hydro fluorocarbons (HFCs) are

obtained by synthesis from natural gases such as chlorine-free ethane and methane, which substitute hydrogen for chlorine and are therefore defined as relatively more environmentally friendly. Natural refrigerants that do not affect global warming and do not harm the ozone layer are undoubtedly the most important alternatives in this process. CO_2 gas is one of the natural gases used for cooling. Supermarkets and cold stores require cooling at very low temperatures. Cooling at very low temperatures is either impossible or very difficult with single-stage cooling systems. However, in the low-temperature range of cascade systems, halogenated hydrocarbons are not the first choice that comes to mind because of their relatively insufficient thermo physical properties. Thus, there is a tendency to use carbon dioxide at the low-temperature stage. The superior heat transfer capability and large volumetric capacity of carbon dioxide make it possible to use in the cascade cooling systems with the low-temperature range. Furthermore, the environmental harm of carbon dioxide and its impact on global warming are less than that of artificial refrigerants. This is another factor that makes carbon dioxide the preferred one instead of others (Çerkezoğlu, 2010).

In this study, R717/R744 refrigerant cascade refrigeration system with R717 refrigerant is used as an alternative to the existing refrigeration system with single-stage mechanical compression, to freeze the ice cream in a factory producing ice cream in addition to the studies in the literature. Thermodynamic analysis of the used cascade cooling and the single-stage cooling systems were made, with the help of the Coolpack program and the systems were compared with each other. The study is thought to be useful in the selection of cooling systems used in the ice cream production.

2. MATERIAL AND METHODS

2.1. Introduction of Cooling Systems

The working principle of the vapor cycle cooling system is as follows. The refrigerant vaporized in the evaporator enters the compressor in the vapor phase and is compressed to a certain pressure in the compressor. The temperature of the gas, whose pressure increases, also increases spontaneously. The compressed gas in the compressor then enters the condenser. Condensation occurs at constant pressure in the condenser. The liquid exiting the condenser is subjected to constant enthalpy expansion as it passes through the throttling valve. The refrigerant from the expansion valve is in the form of a liquid-vapor mixture and this mixture enters the evaporator again. The same operations are repeated throughout the cycle (Çerkezoğlu, 2010). A schematic representation of the cycle is shown in Figure 2.

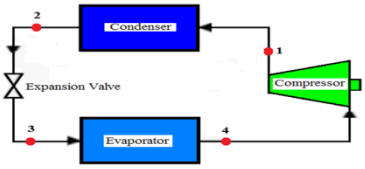

Fig. 2. The single-stage mixture refrigeration cycle

In the cycle shown in the Figure 2, the processes occur respectively as follows.
4-1 Adiabatic compression (in compressor)
1-2 Condensation at constant pressure and temperature (in condenser)
2-3 Pressure decrease in constant enthalpy (in expansion valve)
3-4 Evaporation at constant temperature and pressure (in evaporator).

The cascade refrigeration cycle is a cooling cycle consisting of two cycles with two different fluids that do not mix. One of the two cycles is usually the compression cycle, in which heat is transferred to the outside. In these systems, mainly R717 (NH_3, ammonia), R404A and other suitable HFC fluids are being used (Vestergaard, 2007). In this type of systems, the working pressure is around 40-45 bar (Onbaşıoğlu, 2010). The schematic representation of the system is shown in Figure 3 and the ln P-h diagram of the cycle is shown in Figure 4.

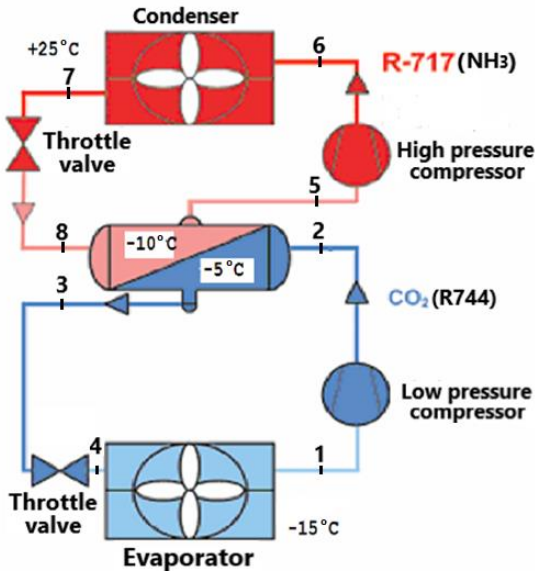

Fig. 3. The Cascade cycle diagram(Vestergaard, 2007)

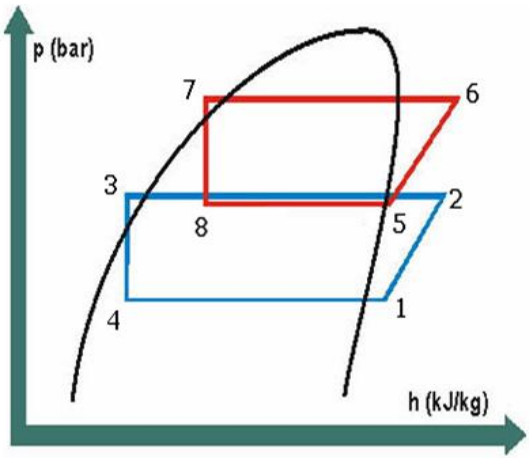

Fig. 4. Ln P - h diagram of the Cascade Cycle (Kasap et al.,2011)

The state changes occurring in the cascade cycle diagram shown in Figure 3 and Figure 4 are as follows, respectively.
1–2 Isentropic compression in the CO_2 compressor
2–3 Condensation of CO_2 at constant pressure in the cascade condenser (barrel type)

3–4 Expansion of liquid CO_2 in the expansion valve
4–1 Evaporation at constant pressure in the evaporator
5-6 Isentropic compression in the R717 compressor
6-7 Condensation at constant pressure in the R717 condenser
7-8 Expansion on constant enthalpy in the R717 expansion valve
8–5 Evaporation of NH_3 at constant pressure in the cascade condenser (barrel type)

2.2. Determination of Cooling Load

Assumptions made in calculations;
*The compressors in the systems perform adiabatic compression.
*The expansion of the throttling valves takes place at constant enthalpy.
*Kinetic and potential energy changes were neglected.
*Evaporation temperature is -15ºC, condensation temperature is 25ºC, isentropic efficiency of compressors is 70% and heat loss rates of compressors are taken as 10%.
*The annual production capacity of the factory is $50x10^6$ liters.
*Density of ice cream is 490 g/Lt
*Mass flow of ice cream is 0.777 kg/s.
*The specific heat of the milk (c_{milk}) is 0.94 kcal/kgºC at 20ºC, 0.90 kcal/kgºC at 4ºC.
*10 people work 20 hours a day around the ice cream machine. The heat emitted by a person; room temperature was accepted as 215 kcal/h for 20°C.
*In order to illuminate the cooled area, 15 piece 100W fluorescent luminaires have operating 24 hours a day.
*Evaporator has 6 piece fan motors.
*The diameters of the two surfaces of the rotary type hopper are 0.2286 m and 0.240 m, respectively.

The following formulas were used to determine the heat load.

Depending on the room temperature, the heat load from the cooling of the ice cream was determined with the aid of Equation 1.

$$Q = m.c.\Delta T \quad (1)$$

In Eq. 1, Q is the cooling load (kW), c is the specific heat of the milk (kcal/kgºC), ΔT is the temperature difference (ºC).

The heat load from working people and lighting fixtures is obtained with the help of Eq. 2.

$$Q = n.W.H \quad (2)$$

In Eq. 2, n is the number of elements, W is element strength (Watt) and H is the working time of the element.

The heat load caused by electric motors is calculated using Eq. 3.

$$Q = n.W.q\ H \quad (3)$$

In this Equation, q is the heat load from the electric motor. If the engine power is between 1/8 - 1/2 HP and the engine and driven elements are in the cold room, this value is taken as 1070 (kcal/hHP).

The heat load resulting from the temperature of the rotary freezer was determined with the help of Eq. 4.

$$Q = U.A.\Delta T \quad (4)$$

In this Equation, U is the total heat transfer coefficient ($W/m^{2o}C$) and A is the cross-sectional area of the rotor (m^2).

The formulas used in the selection of system elements for the single-stage cooling system are given below, respectively.

Evaporator Selection,

$$Q_e = \dot{m}_{717}(h_4 - h_3) \quad (5)$$

Condenser Selection,

$$Q_c = \dot{m}_{717}(h_1 - h_2) \quad (6)$$

Compressor Selection,

$$Q_{comp} = \dot{m}_{717}(h_1 - h_4) \quad (7)$$

The formulas used in the selection of system elements for the two-stage cooling system (Cascade) are listed below.

For the high temperature part (HT)

Evaporator Selection,

$$Q_{e,HT} = \dot{m}_{717}(h_7 - h_6) \quad (8)$$

Condenser Selection,

$$Q_{c,HT} = \dot{m}_{717}(h_3 - h_5) \quad (9)$$

Compressor Selection,

$$Q_{comp,HT} = \dot{m}_{717}(h_2 - h_8) \quad (10)$$

For the low temperature part (HT)

Evaporator Selection,

$$Q_{e,LT} = \dot{m}_{744}(h_8 - h_6) \quad (11)$$

Condenser Selection,

$$Q_{c,LT} = \dot{m}_{744}(h_3 - h_5) \quad (12)$$

Compressor Selection,

$$Q_{comp,LT} = \dot{m}_{744}(h_8 - h_2) \quad (13)$$

Moreover, the cooling performance of the system was calculated with equation 14 and the second law efficiency was calculated with equation 15.

Cooling performance of systems,

$$COP = \frac{Q_e}{W_{net}} = \frac{Q_e}{W_{HT}+W_{LT}} \quad (14)$$

Second law efficiency of systems,

$$\eta_{II} = \frac{COP}{COP_{tr}} \quad (15)$$

3. FINDINGS and DISCUSSION

The findings obtained from the researches performed on the systems with the help of the equations given above are presented in Table 1 and 2.

Table 1. Cooling Load of System

The heat load from the cooling of the ice cream (Eq.1)	$Q_{1@20^oC}$ = 48.84 kW
	$Q_{2@4^oC}$ = 26.30 kW
The heat from lighting fixtures (Eq.2)	$Q_{lighting}$ = 1.54 kW
The heat from humans (Eq.2)	Q_{human} = 2.27 kW
The heat from electric motors (Eq.3)	$Q_{fan\ motors}$ =2.2 kW
The heat from the rotary freezer (Eq.4)	$Q_{freezer}$ =10.67 kW
TOTAL	Q_{total}=91.82 kW

In the area where the ice cream machine is located, the total heat load was 91.82 kW and it was assumed that the total heat load was 101.3 kW with a 10% safety margin. In this case, the capacities of the selected system elements for both systems are presented in Table 2.

Table 2. Selection of system elements

For the single-stage cooling system	
h_1 = 1723.6 kJ/kg = 412.35kcal/kg	
$h_2 = h_3$ = 291 kJ/kg = 69.62 kcal/kg	
h_4 = 1439.6 kJ/kg = 344.40 kcal/kg	
$\dot{m}_{717}$ = 0.08819 kg/s	
Evaporator Selection	$Q_e = Q_{total}$ $Q_e = \dot{m}717$ x (1439.6 – 291) = **101.3 kW**
Condenser Selection	Q_c = 0.08819 x (1723.6 – 291) = **126.4 kW**
Compressor Selection	Q_{comp} = 0.08819 x (1723.6 – 1439.6) = **25.1 kW**
For the two-stage cooling system (Cascade)	
High Temperature Part (HT)	
$h_5 = h_6$ = 291 kJ/kg = 69.62 kcal/kg	
h_7 = 1448.6 kJ/kg = 345.992 kcal/kg	
h_8 = 1451.2 kJ/kg = 346.613 kcal/kg	
$\dot{m}_{717}$ = 0.0875 kg/s	
Evaporator Selection	$Q_e = Q_{total}$ = **101.3 kW** $Q_e = \dot{m}_{717}(h_7-h_6)$ $\dot{m}_{717}$ = 0.0875 kg/s
Condenser Selection	Q_c = 0.0875 x (1682 – 291) = **121.7 kW**
Compressor Selection	Q_{comp}= 0.0875 x (1681.8 – 1451.2) = **23.06 kW**
Low Temperature Part (LT)	
Evaporator Selection	$Q_e = Q_c$ $\dot{m}_{744} = \dot{m}_{717}\frac{(h_7-h_6)}{(h_3-h_5}$ $\dot{m}_{744}$ = 0.36 kg/s $Q_{e,LT}$ =0.36x(-58.5-(-323.5)) = **95.4 kW**
Condenser Selection	Q_c = **101.3 kW**
Compressor Selection	Q_{comp} = 0.36 x (42.4-(-58.5)) = **16.1 kW**

The accuracy of the values obtained after the theoretical calculations were compared with the CoolPack cooling analysis program. The analyzes of the systems were given in Figure 5-6 and the found values in Table 3-6 respectively.

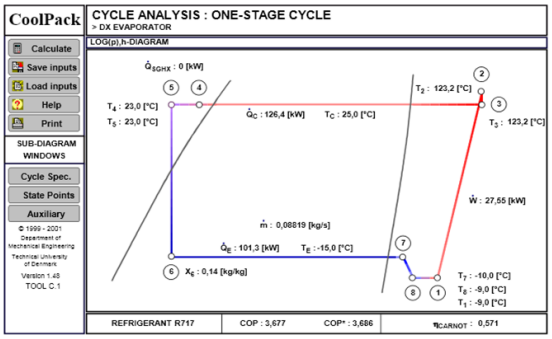

Fig. 5. Input values of the single-stage cycle examined in the CoolPack

Table 3. Values at each point of the single-stage cycle

State Point	Temperature (ºC)	Pressure (kPa)	Enthalpy (kJ/kg)	Density (kg/m³)
1	-9.0	231.2	1442.4	1.9
2	123.2	1021.6	1723.6	5.5
3	123.2	1006.0	1724.0	5.4
4	23.0	1006.0	291.0	605.8
5	23.0	1006	291.0	605.8
6	-15.0	236.2	291	-
7	-10.0	236.2	1439.6	1.9
8	-9.0	231.2	1442.4	1.9

Furthermore, it has been seen that the COP value of the single stage refrigeration cycle was 3.67, the pressure ratio (P_2 / P_1) was 4.418, the $T_{2.1s}$ value was 98ºC and the $T_{2,w}$ value was 135ºC. In this expression, $T_{2.1s}$ value is the temperature of the discharge gas assuming eversible and adiabatic compression. In the same way, $T_{2,w}$ value is the temperature of the discharge gas assuming real and adiabatic compression.

Table 4. Supporting information on the single-stage cycle

Cooling Capacity		
Q_e=101.3 kW	Q_c=126.4 kW	$\dot{m}$=0.08819 kg/s
Compressor Performance		
Isantropic efficiecy, η_{1s} =0.7		W_{comp}=27.55 kW
Compressor Heat Loss		
Heatloss factor f_Q = 10%	T_2 =123.2 ºC	Q_{loss}=2.755 kW
Suction Line		
Unuseful superheat	Q_{sL}=0.249 kW	T_s=-9 ºC

For the two-stage cascade coolig system

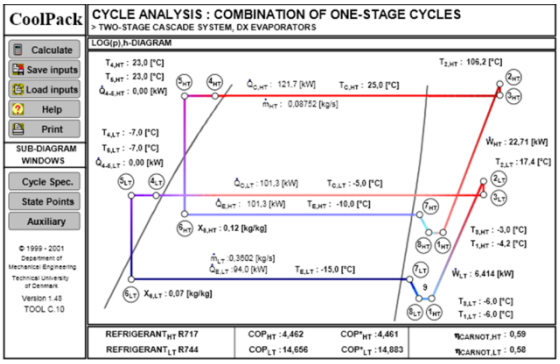

Fig. 6. Input values of the cascade cycle examined in CoolPack

Table 5. Values at each point of the cascade cycle

High Temperature (HT)				
State Point	Temperature (°C)	Pressure (kPa)	Enthalpy (kJ/kg)	Density (kg/m³)
1	-4.2	288.6	-4.2	2.3
2	106.2	1012.2	1681.8	5.7
3	106.2	1006.0	1682.0	5.7
4	23.0	1006.0	291.0	605.8
5	23.0	1006.0	291.0	605.8
6	-10.0	290.9	291.0	-
7	-4.0	290.9	1448.6	2.3
8	-3.0	288.6	1451.2	2.3
9	-4.2	288.6	1448.3	2.3
LowTemperature (LT)				
State Point	Temperature (°C)	Pressure (kPa)	Enthalpy (kJ/kg)	Density (kg/m³)
1	-6.0	2277.2	-58.5	55.9
2	17.4	3062.5	-42.4	69.1
3	17.4	3045.8	-42.2	68.7
4	-7.0	3045.8	-323.5	968.3
5	-7.0	3045.8	-323.5	968.3
6	-15.0	2290.7	-323.5	-
7	-9.0	2290.7	-62.5	57.7
8	-6.0	2277.2	-58.5	55.9
9	-	-	-	-

Table 6. Supporting information on the cascade cycle

Cycle Capacity		
High Temperature (HT)		
$Q_{e,HT}$=101.3 kW		$\dot{m}$=0.08752 kg/s
Compressor Performance		
Isantropic efficiecy, η_{1s} =0.7		W_{HT}= 22.71 kW
Compressor Heat Loss		
Heat loss factor f_Q = 10%	T_2 =106.2 °C	Q_{loss}=2.3 kW
Suction Line		
Unuseful superheat	Q_{sL}=0.228 kW	T_s=-3 °C
Low Temperature (LT)		
$Q_{e,LT}$=94 kW		$\dot{m}$=0.3602 kg/s
Compressor Performance		
Isantropic efficiecy, η_{1s} =0.7		W_{LT}= 6.414 kW
Compressor Heat Loss		
Heat loss factor f_Q = 10%	T_2 =17.4 °C	Q_{loss}=0.6 kW
Suction Line		
Unuseful superheat	Q_{sL}=1.456 kW	T_s=-6 °C
For the whole system; Total compressor power		W_{tot}= 29.12 kW

If Figure 4-6 and Table 3-6 are examined, lower and upper stage evaporation and condensation temperatures of each cycle, heating and cooling capacities, compressor powers, heat loss rates of compressors, overcooling, overheating, unuseful superheating temperature differences and pressure losses can be seen.

4. CONCLUSIONS

In this study, a single-stage cooling system with R717 refrigerant and a cascade cooling system with R717/R744 system were compared with each other. As a result of the calculations, an evaporator load of 101.3 kW was found and a comparison was made for a system operating in the temperature range (25°C, -15°C) following the freezing production steps.

The calculations were made both manually and with the Coolpack program and the results were confirmed. As a result of the calculations, the COP value of the single-stage system was calculated as 3.67, the Carnot efficiency 0.57, the second law efficiency 0.19 and the power required to operate the compressor was 27.55 kW. In the cascade cooling system, the COP value was 4.46, the Carnot efficiency 0.59 and the compressor power 22.7 kW at the high-temperature part, the COP value was 14.656, the Carnot efficiency 0.58 and the compressor power 6.4 kW at the low-temperature part. For the whole cascade system, the COP 3.24 and the second law efficiency were found to be 0.43. When the results compared, it was seen that the COP values of the high and low-temperature parts of the cascade system were higher than the single-stage ammonia system, but when evaluated for the whole system, the COP value was less than 0.43 points. However, the usage of the cascade system is important when considering the fact that the cooling system will be used in the food sector and reducing environmental damage, as well as reducing the heat and losses emitted by decreasing compressor pressure rates.

Besides, considering both the climatic conditions of our country and the thermo physical properties of carbon dioxide gas, it was seen that the most suitable design that can use carbon dioxide gas is the cascade cooling system. Usage of the carbon dioxide in the low-temperature cycle of the cascade system eliminates the disadvantage of high pressure caused by the low triple point (31°C) and increases its usability in this system since carbon dioxide has a positive effective pressure even at temperatures as low as -55°C. The minimum temperature that can be achieved when ammonia used in a low-temperature cycle is -35°C. The pressure of ammonia gas below this temperature falls below the atmospheric pressure and it circulates with the air-fluid, causes damage to the equipment due to moisture in it, leads leakage, and poisoning. However, carbon dioxide does not have such disadvantages and provides optimum operation at -10°C. In conclusion, the overall superiorities of carbon dioxide make it a highly suitable secondary refrigerant for the cascade system.

REFERENCES

Alan, A. (2011). The effect of expansion turbine usage on energy potential in dual stage CO_2 cooling systems, MSc Thesis, University of Süleyman Demirel, Isparta, Turkey.

Bingming, W., Huagen, W., Jianfeng, L., Ziwen, X. (2009). "Experimental investigation on the performance of NH3/CO2 cascade refrigeration system with twin-screw compressor." *International Journal of Refrigeration*, Vol. 32, No. 6, pp. 1358–1365.

Çerkezoğlu, B. (2010). Analysis of Cascade Cooling System Using Co_2, MSc Thesis, Istanbul Technical University, Istanbul, Turkey.

Dopazo, J. A., Fernández-Seara, J., Sieres, J., Uhía, F. J. (2009). "Theoretical analysis of a CO– NH cascade refrigeration system for cooling applications at low temperatures." *Applied Thermal Engineering*, Vol. 29, No. 8-9, pp. 1577–1583.

Dopazo, J. A., Fernández-Seara, J. (2011). "Experimental evaluation of a cascade refrigeration system prototype with CO2 and NH3 for freezing process applications." *International Journal of Refrigeration*, Vol. 34, No. 1, pp. 257–267.

Getu, H. M., Bansal, P. K. (2007). "Modeling and performance analysis of evaporators in frozen food supermarket display cabinets at low temperatures." *International Journal of Refrigeration*, Vol. 30, No. 7, pp. 1227-1243.

Kasap, F., Acül, H., Canbaz, H., Erbil, S. (2011). "R744 (CO_2) Refrigerant cooling systems, finned tube R744 (CO_2) evaporator and gas cooler design principles." *X. National Installation Engineering Congress*, İzmir, Turkey, pp. 391-410.

Onbaşıoğlu, H. (2010). "An Overview of Vapour Compression System Using Natural Refrigerant CO_2". *İSKİD ACV&R Journal of Turkey*, Vol.2, pp.48-64.

Özyurt, A., Erdönmez, N., Yilmaz, B., Yilmaz, D., Sevindir, M. K., Mançuhan, E. (2014). "Thermodynamic Analysis and Performance Evaluation of CO2 / NH3 Cascade Cooling System." 15th *International Refrigeration And Air Conditioning Conference*, Plant Egineering, Purdue, Indiana pp. 2598-2608.

Rezayan, O., Behbahaninia, A. (2011). "Thermoeconomic optimization and exergy analysis of CO2/NH3 cascade refrigeration systems." *Energy*, Vol. 36, No. 2, pp. 888–895.

Vestergaard, N. P. (2007). "Danfoss Refrigeration and Air Conditioning Division, CO_2 Refrigerant for Industrial Refrigeration". Danfoss A/S (RA Marketing/MWA), DKRCI.PZ.000.C1.02 / 520H2242.

Turkish Journal of Engineering

Turkish Journal of Engineering (TUJE)
Vol. 5, Issue 2, pp. 69-72, April 2021
ISSN 2587-1366, Turkey
DOI 10.31127/tuje.653061
Research Article

GRAPHENE PRODUCED WITH USING SURFACTANT FROM EXPANDED GRAPHITE

Ali Sönmez [1], Ömer Güler [2], Öyküm Başgöz *[3] and Seval Hale Güler [4]

[1] Mersin University, Engineering Faculty, Metalurgical and Material Eng. Dept., Mersin, Turkey, alisnmezz@gmail.com

[2] Mersin University, Engineering Faculty, Metalurgical and Material Eng. Dept., Mersin, Turkey, oguler@mersin.edu.tr

[3] Mersin University, Engineering Faculty, Metalurgical and Material Eng. Dept., Mersin, Turkey, oykumbasgoz@hotmail.com

[4] Mersin University, Engineering Faculty, Metalurgical and Material Eng. Dept., Mersin, Turkey, shguler@mersin.edu.tr

* Corresponding Author
Received: 29/11/2019 Accepted: 09/03/2020

ABSTRACT

Graphene is a single layer of graphite with hexagonal structure which have stacked layers. Graphene has recently been recognized by its researchers due to it have sp2 bonds in hexagonal lattice, the two-dimensional structure of a single atomic thickness, and its superior electrical, electrochemical, optical, thermal, mechanical properties and lightness. Liquid phase exfoliation (LPE) is the most promising method of graphene research to produce high quality graphene in the production of single or low layer graphene layers. In addition, LPE is an easy and inexpensive method as well as enables the production of higher capacity graphene. LPE method in the production of graphene is the use of surfactant mainly to make water suitable as a means of exfoliation. Furthermore, graphene adsorbable surfactants provide an effective charge by electrostatic repulsion to prevent the re-aggregation of graphene sheets, thus providing stabilization against the recombination of suspended graphene layers. Because 1,2-Dichlorobenzene or ortho-dichlorobenzene (O-DCB) is both effective as solvent for graphene synthesis, it is one of the best production of graphene by the liquid phase exfoliation method. In this study, graphite powders were mixed in an acid solution of H_2SO_4 and HNO_3 for 12h. The resulting powder was washed with distilled water until a neutral pH was obtained and then subjected to thermal treatment to obtain expanded graphite. The resulting powder was then mixed in an ultrasonic homogenizer in a mixture of O-DCB for 2h using 50 % strength and then it was examined by Transmission electron microscope (TEM) and X-ray photoelectron spectroscopy (XPS).

Keywords: *Graphene, ortho-dichlorobenzene, Expanded Graphite, LPE.*

1. INTRODUCTION

Graphene is known as a surprising material in recent years due to its new features related to its two-dimensional structure (Monajjemi, 2017). Its intriguing properties such as high strength, an optical transmittance of 97,7 %, carriermobility as high as 200,000 cm2 V^{-1} s^{-1} at room temperature and a Young's modulus of 0.5–1 TPa, perfect electrical conductivity and high thermal conductivity make it promising for various applications (Arao *et. al*., 2017). Due to these features of graphene, flexible devices, high-frequency transistors, energy storage and transducers, sensors, biomedical applications and the production of new generation composites have been demonstrated that graphene can be made easily (Wei, *et. al*, 2015). Today, the most widely used methods in the production of graphene; mechanical exfoliation, chemical method (reduction of graphene oxide), chemical vapor deposition (CVD), epitaxial growth in silicon carbide, liquid phase exfoliation method (LPE), electrochemical exfoliation, the solvothermal method, arc discharge (Lee, *et. al*., 2019)

Commercialization of graphene-oriented applications is inevitable, but cost-effective and high-quality serial production is needed (Xu, *et. al*., 2014). Since the first day it was found and applied, the liquid phase exfoliation method has been proposed as the most promising method of graphene research to produce high quality single or low layer graphene sheets in solvent dispersion forms. The main advantage of this process is a simple and sizable process in which pure graphite or expanded graphite is applied directly to a solvent process to weaken the Van Der Waals tensile forces between graphene interlayers (Durge, *et. al*., 2014). Many successes have been achieved in the production of graphene by liquid phase exfoliation method by using numerous solvent systems and suitable surfactants (Huo , *et. al*., 2015). Although the Liquid Phase Exfoliation Method is a relatively easy and inexpensive method, the quality of the products produced is higher than the products produced by other methods (Zhu, *et. al*., 2013).

In this study, graphite powders were mixed in an acid solution of H_2SO_4 and HNO_3 for 12h. The resulting powder was washed with distilled water until a neutral pH was obtained and then subjected to thermal treatment to obtain expanded graphite. The resulting powder was then mixed in an ultrasonic homogenizer in a mixture of O-DCB for 2h using 50 % strength. The main purpose of this study is to investigate the effects of O-DCB which is used as solvent in graphene synthesis by liquid phase exfoliation method in graphene production.

2. EXPERIMENTAL PROCEDURE

Hexagonal graphite powders were dried at 90 °C for 2 hours to remove moisture. The dried graphite powder was mixed for 12 hours in saturated acid containing H_2S0_4 and $HN0_3$. After this process, this formed structure is called graphite intercalation compound (GIC). It was carefully washed with distilled water. Then, GIC was heated at 1000 ^oC to form expanded graphite (EG).

The graphene layers are bound by weak van der Waals forces at some points of the EG and these bonds need to be broken. Therefore, EG was subjected to ultra-sonication in O-DCB solvent. The suspension of 0.07 mg/ml concentration of EG with O-DCB was prepared. The solution of EG was kept at multi-frequency ultrasonication homogenizer for 1h. Then, the mixture was centrifuged at 5000 rpm for 8 hours to remove O-DCB. The low density material suspended at the top layer of centrifuged solution was collected for further characterization. Transmission electron microscope (HRTEM) (JEOL Jem 1100) was used to investigate the microstructure of graphene samples. The samples were chractersized via X-ray photoelectron spectroscopy (XPS) (Specs-Flex) and Raman Spectroscopy (WITech alpha 300-R 512 nm wavelenght).

3. RESULTS AND DISCUSSION

The layers include a weak Van Der Waals bond. The aim of this study is to produce the graphene by breaking the Van Der Waals bonds between the graphite layers lined up. A solvent is required to separate the layers. Since the atomic diameters of the solvents that will allow the layers to separate are larger than the distance between the graphite layers, they cannot enter between the layers. For this reason, the distance between the layers of hexagonal graphite is first expanded by acid and thermal treatment. After these processes, the gap between the hexagonal layers widen and the weak bonds between the layers easily break through the incoming solvent atoms.
In previous our studies, different solvents (Such as DMF, NMP eg.) were used for graphene synthesis via Liquid Phase Exfoliation (LPE). It was shown in literature that O-DCB also is suitable a solvent because of its surface properties.

TEM images of samples were given after LPE process by using O-DCB as solvent. As can be seen in the figure, the exfoliation process was carried out successfully as planned and the layers were separated from each other. The width of the layers is over 200 nm. In Figure 1.a there is a dark colored fouling. Contamination is believed to be solvent residues during the production of amorphous carbon or graphene.

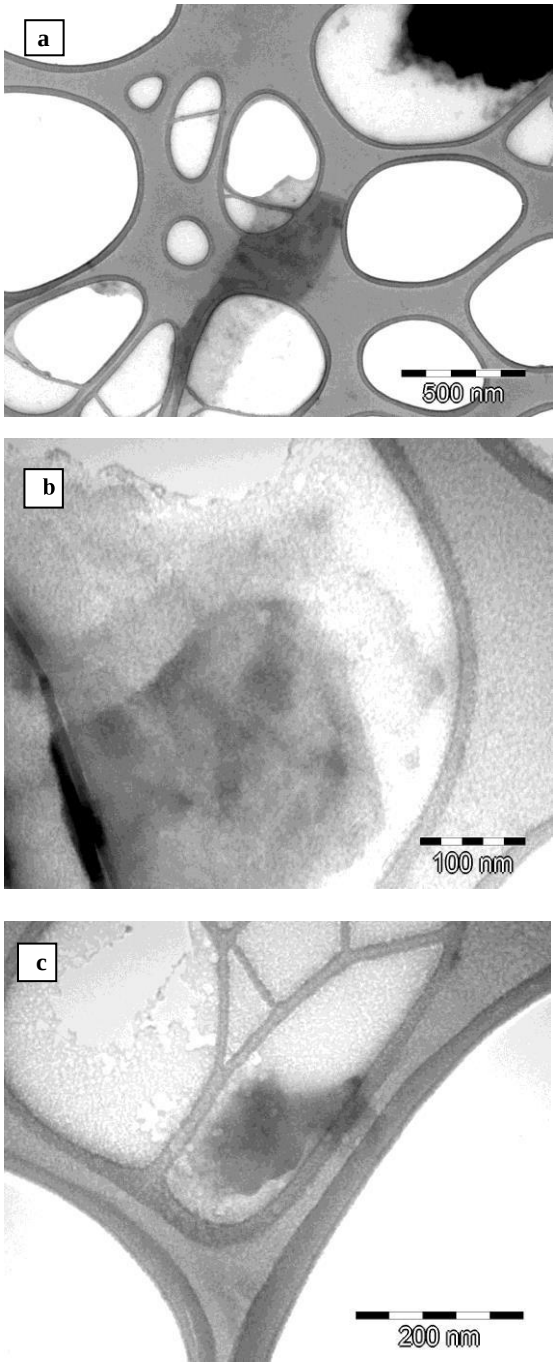

Fig. 1. (a),(b),(c) TEM micrographs of high magnification of synthesized graphene layers

In figure 2, XPS spectra analysis of samples were given. Figure 2a. shows general XPS spectra, Figure 2b. shows fitting of XPS peaks. As the figure shows that, synthesized graphenes contain C-C bonds over 80 %. In addition, C-O bonds exist in samples. We think that C-O bonds formed when EG was produced. Because, graphite powders were treated with acids and powders were heated to high temperature.

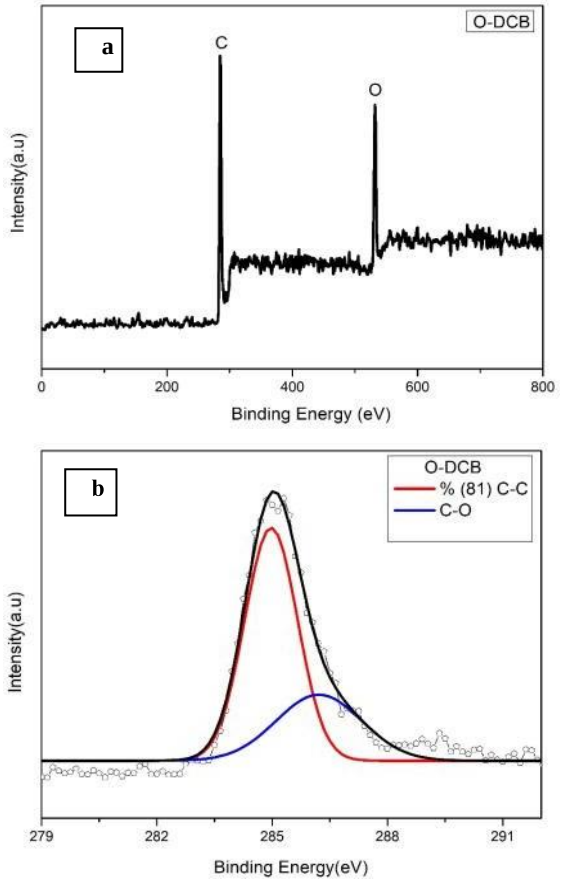

Fig. 2.(a) General XPS spectra, (b) XPS spectra fitting of synthesized Graphene layers

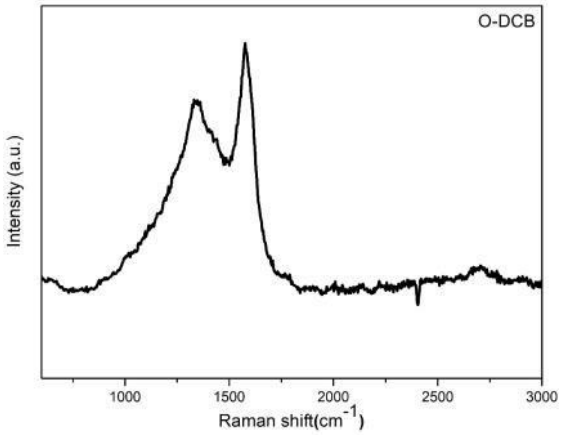

Fig. 3. Raman Spectra of synthesized graphene layers

In this study, the analyzes show that production of graphene nanosheets were achieved with Liquid-Phase Exfoliation method by using O-DCB as solvent.

Figure 3 shows the Raman spectra of synthesized graphenes. In Raman spectra of graphenes, 3 characteristic peaks were shown. D peak (at 1350 cm^{-1}) relate to defects in graphenes (in sheets basal plane or sheet edges). G peak (at 1582 cm^{-1}) relates to C atoms vibrations having sp^2 hibritazition in hexagonal lattice.

2D peak (at 2700 cm^{-1}) indicates graphenes existence in powders. In Raman spectra of our samples, these peaks exist. The intensity of 2D peak is weak. This show that not only graphene exist in samples but also graphene

nanosheets. The intensity of D peak is comparatively high. This show that defects exist in synthesized powders. We think that these defect formed during ultrasonic process.

4. CONCLUSION

In this study, O-DCB was used as solvent in graphene synthesis via LPE method. In first step, EG was produced. Subsequently, EG was sonicated in O-DCB in order to synthesis graphene. It shown that graphene was synthesized by using O-DCB. But, graphene nanosheets also form together with graphene in samples.

ACKNOWLEDGEMENTS

We would like to acknowledge the financial support from Mersin University Department of Scientific Research Projects (Project No: 2018-3-TP2-3085).

REFERENCES

Arao, Y., Mori, F., & Kubouchi, M. (2017). "Efficient solvent systems for improving production of few-layer graphene in liquid phase exfoliation." *Carbon*, Vol. 118, pp. 18-24.

Dhakate, S. R., Chauhan, N., Sharma, S., Tawale, J., Singh, S., Sahare, P. D., & Mathur, R. B. (2011). An approach to produce single and double layer graphene from re-exfoliation of expanded graphite. *Carbon, 49*(6), 1946-1954.

Durge, R., Kshirsagar, R. V., & Tambe, P. (2014). "Effect of sonication energy on the yield of graphene nanosheets by liquid-phase exfoliation of graphite."*Procedia Engineering*, Vol. 97, pp. 1457-1465.

Huo, C., Yan, Z., Song, X., & Zeng, H. (2015). "2D materials via liquid exfoliation: a review on fabrication and applications." *Science Bulletin*, Vol. 60, pp. 1994-2008.

Lee, X. J., Hiew, B. Y. Z., Lai, K. C., Lee, L. Y., Gan, S., Thangalazhy-Gopakumar, S., & Rigby, S. (2019). "Review on graphene and its derivatives: Synthesis methods and potential industrial implementation."*Journal of the Taiwan Institute of Chemical Engineers*, Vol. 98, pp. 163-180.

Monajjemi, M. (2017). "Liquid-phase exfoliation (LPE) of graphite towards graphene: An ab initio study*." Journal of Molecular Liquids*, Vol. 230, pp. 461- 472.

Narayan, R., & Kim, S. O. (2015). Surfactant mediated liquid phase exfoliation of graphene. *Nano Convergence*, *2*(1), 20.

Novoselov, K. S., Geim, A. K., Morozov, S. V., Jiang, D., Zhang, Y., Dubonos, S. V., ... & Firsov, A. A. (2004). Electric field effect in atomically thin carbon films. *science*, *306*(5696), 666-669.

Wei, Y., & Sun, Z. (2015). "Liquid-phase exfoliation of graphite for mass production of pristine few-layer graphene." *Current opinion in colloid & interface science*, Vol. 20, pp. 311-321.

Xu, J., Dang, D. K., Liu, X., Chung, J. S., Hur, S. H., Choi, W. M., ... & Kohl, P. A. (2014). "Liquid-phase exfoliation of graphene in organic solvents with addition of naphthalene." *Journal of colloid and interface science*, Vol. 418, 37-42.

Zhu, L., Zhao, X., Li, Y., Yu, X., Li, C., & Zhang, Q. (2013). "High-quality production of graphene by liquid phase exfoliation of expanded graphite." *Materials Chemistry and Physics*, Vol. 137, pp. 984-990.

Turkish Journal of Engineering

Turkish Journal of Engineering (TUJE)
Vol. 5, Issue 2, pp. 73-79, April 2021
ISSN 2587-1366, Turkey
DOI 10.31127/tuje.674021
Research Article

REMOVAL OF COD AND SURFACTANTS FROM GREY WATER BY FENTON TYPE PROCESSES

Serkan Şahinkaya*[1], Gamze Özgüroğlu[2]

[1] Nevsehir Haci Bektas Veli University, Engineering and Architecture Faculty, Department of Environmental Engineering, Nevsehir, Turkey
ORCID ID 0000-0002-0176-4198
e-mail: serkansahinkaya@gmail.com

[2] Nevsehir Haci Bektas Veli University, Engineering and Architecture Faculty, Department of Environmental Engineering, Nevsehir, Turkey
ORCID ID 0000-0003-3133-3310
e-mail: gamzeozguroglu.go@gmail.com

* Corresponding Author
Received: 13/01/2020 Accepted: 04/04/2020

ABSTRACT
Grey water is a kind of domestic wastewater including shower, bath, lavatory and laundry waters. Grey waters without faecal waste can be considered as alternative water sources in the place where water resources are limited. In the present study, the removals of COD, anionic and non-ionic surfactants from grey water via conventional (CFP) and modified (MFP) Fenton oxidation processes was experienced. It was determined that pH adjustment to acidic values is not required in CFP. The optimum operating conditions were determined as $[Fe^{2+}]$ = 50 mg/L, $[H_2O_2]$ = 50 mg/L at pH 7.6 (original pH) in CFP and [ZVI] = 50 mg/L, $[H_2O_2]$ = 50 mg/L at pH 3 in MFP, respectively. As a result, the CFP has been found to be a more efficient alternative treatment method for the treatment of grey water, compared to MFP.

Keywords: *COD, Fenton, Grey water, Oxidation, Surfactant.*

1. INTRODUCTION

Domestic wastewater is evaluated in two streams: grey water and black water. Generally, water from the shower, bath, washbasin, washing and dishwashers is defined as grey water (Bani-Melhem *et al.*, 2015). The remaining toilet water is defined as black water. The grey water includes 80–85% of household wastewater (Bani-Melhem *et al.*, 2015). The re-use of this kind of wastewaters is considered as an alternative to the reduction of clean water consumption. However, there is no legal regulation in many countries for the re-use of grey waters after treatment. On the other hand, there is an increasing interest in this issue with the increasing water scarcity. The low organic matter and pathogen content of grey waters further increase this interest for reusability. The fact that grey waters can contain heavy metal and synthetic chemical structure micro pollutants such as pharmaceuticals, detergents, etc., cause us to seek alternatives other than conventional biological treatment systems. Therefore, the treatment of grey wastewaters by Fenton process and its modification has been evaluated in this study.

Conventional Fenton process (CFP) is intended to generate hydroxyl (OH•) radicals by catalyzing hydrogen peroxide (H_2O_2) with ferrous (Fe^{2+}) ions under strongly acidic conditions (Eq. (1)) (Pignatello *et al.*, 2006). OH• radicals are very strong oxidants and can easily decompose organic matters. Oxidation of organic substances by hydroxyl radicals (OH•) is generally achieved by the following chain reactions. (Eq. 1-4) (Vorontsov, 2019; Zhu *et al.*, 2019).

$$\boldsymbol{Fe^{2+} + H_2O_2 \rightarrow Fe^{3+} + OH^- + OH^{\bullet}} \quad (1)$$

$$Fe^{2+} + OH^{\bullet} \rightarrow Fe^{3+} + OH^- \quad (2)$$

$$RH + OH^{\bullet} \rightarrow H_2O + R^{\bullet} \quad (3)$$

$$H_2O_2 + OH^{\bullet} \rightarrow H_2O + HO_2^{\bullet} \quad (4)$$

In the Fenton process, instead of ferrous iron (Fe^{+2}), iron powder (zero valent iron, ZVI, Fe^0) can also be utilized (Jaafarzadeh *et al.*, 2017). This modification of the process is called the modified Fenton process (MFP). In order to achieve the oxidation reaction in MFP, the ZVI must first be dissolved in strongly acidic conditions in accordance with Eq. 5 (Bremner *et al.*, 2006). The reaction will then be carried out as in the conventional Fenton process (Eq. 2). In addition, Fenton oxidation reactions can occur on the surface of ZVI (Eq. 6) (Bergendahl and Thies, 2004). In this respect, the MFP is more dependent on pH than CFP.

$$\boldsymbol{Fe^0 + 2H^+ \rightarrow Fe^{2+} + H_2} \quad (5)$$

$$\boldsymbol{Fe^0 + H_2O_2 \rightarrow Fe^{2+} + 2OH-} \quad (6)$$

The main advantage of the usage of ZVI in the Fenton process is that ferric ions can be converted to ferrous ions on the surface of the ZVI (Eq. 7) (Bremner *et al.*, 2006). This conversion will cause the usage of less amount of iron than the conventional Fenton process. Reduction of iron consumption will reduce both the cost of treatment and the reduction of inert chemical sludge.

$$\boldsymbol{Fe^0 + 2Fe^{3+} \rightarrow 3Fe^{2+}} \quad (7)$$

In the literature, there are several studies on the successful treatment of grey water with Fenton process. For example, in the study conducted by Hossain (2015), the use of grey water treated by Fenton process as toilet wash water was investigated. In the study which examined biochemical oxygen demand (BOD), chemical oxygen demand (COD), total solids (TS), turbidity and total carbon parameters, it was seen that the treated grey water provided with high efficiency through the classical Fenton process met the relevant standards in USA, Canada and Japan in order to be used as toilet wash water. In another study by Thirugnanasambandhama and Sivakumar (2015), 90% COD and 85% total suspended solid (TSS) removal was obtained by electro-Fenton process. In another study on grey water, Fenton process, starbon adsorption and a combination of the two were tested [10]. The combined use of both processes resulted in a 93% COD removal efficiency by using less Fenton reagents. However, these studies on the treatment of grey water with the Fenton process focused on COD removal with the classical Fenton process. Therefore, in the literature, there is no study comparing the classical and modified Fenton processes on the treatment of grey water and comparing them. In addition, when the studies in the literature are examined, it is observed that the common parameter for the grey waters is COD. In the studies in the literature, it has been determined that surfactant removal is not investigated and these studies are carried out via COD.

The main aim of this study is to investigate the influences of operating parameters in the conventional and modified Fenton processes on the removals of anionic and non-ionic surfactants and COD as the main target parameters. In order to optimize the operating conditions, Fenton experiments were carried out under various pH, iron (Fe^{2+}/ZVI) and hydrogen peroxide dosages. Besides, kinetical analyses for the anionic and non-ionic surfactant and COD removals were performed in the present study.

2. MATERIALS AND METHODS

Grey water was synthetically prepared within 10 L with tap water in this study as summarized in Table 1. The synthetic grey water had a pH of 7.6, COD of 590 mg/L, anionic surfactant of 9 mg/L and non-ionic surfactant of 22 mg/L.

Table 1. Content of synthetic grey water (for 10 L)

Amount in 10 L	*Composition*
0.64 g	Synthetic soap
8 ml	Hair shampoo
0.1 ml	Sunflower oil
24 ml	Secondary effluent

All chemicals were of analytical grade, purchased from Merck (Germany) and were used as bought without any further purification. Ultra-pure water was utilized in the preparation of all solutions.

CFP and MFP experiments were performed with 500

mL volume using a standard jar test equipment at room temperature. These experiments were done in three steps. pH value of the grey water was first adjusted to the desired value by using 0.1 N and 6 N H_2SO_4 solutions. The second step was the addition of Fe^{2+} (as $FeSO_4.7H_2O$) in CFP and ZVI (as solid Fe^0 dust, < 50 µm size) in MFP. Then, the final step is the addition of H_2O_2 into the grey water. After the addition of H_2O_2 into the reaction solution, it was assumed that the oxidation reaction was begun. During the 1-h oxidation period, the grey water was mixed at 90 rpm. At the end of the oxidation period, the reaction solution was neutralized and pH value was adjusted to about 7.5 using 6 N and 0.1 N NaOH solutions. After the pH adjustment, the solution was stirred for 5 min at 30 rpm to form iron (oxy)hydroxide ($Fe(OH)_3$) flocs. It was stand still to precipitate $Fe(OH)_3$ for 30 min. After the precipitation, 25 mL sample was taken from the supernatant for the analyses.

Manganese dioxide (MnO_2) can decompose H_2O_2 to H_2O and O_2 as a catalyst (Tony *et al.*, 2016). Therefore, MnO_2 was dosed into the sample in order to quench the residual H_2O_2 to avoid the positive interference of H_2O_2 on COD analysis (Özdemir *et al.*, 2011). The decomposition of residual H_2O_2 was tested by peroxide test strips (Macherey Nagel, Germany). Before the analyses, all samples were filtered through 0.45 µm membranes to remove $Fe(OH)_3$ and MnO_2. The pH measurement was conducted by a multi-parameter (Hach Lange, Germany). COD analyses were conducted in accordance with Standard Methods (APHA/AWWA/WEF, 2005). The concentrations of anionic and non-ionic surfactants were analyzed calorimetrically by using Hach Lange cuvette tests (Germany).

3. RESULTS AND DISCUSSION

3.1. Effects of Initial pH on COD and Surfactants Removals

Since the solution pH affects both the type and the solubility of catalyst iron, pH has an important effect on the oxidation efficiency (Özdemir *et al.*, 2011; Kwon et al., 1999). The stability of hydrogen peroxide also depends on the medium pH. For these reasons, optimization of the initial pH of the reaction medium is vital to determine the effects of the Fenton process on the OH• radical production efficiency. In this study, optimization of the initial pH was carried out between pH 2 and the original pH 7.6. In both experiments, catalyst iron concentration and H_2O_2 concentration were kept constant at 100 mg/L.

The effect of initial pH on removal of COD, anionic and non-ionic surfactants is shown in Fig. 1. As can be seen from Fig. 1, the MFP process is much more dependent on ambient pH. Therefore, CFP process achieved oxidation at a much higher yield than MFP. Maximum removal efficiencies were obtained in pH 2 in MFP and in pH 5 in CFP. This advantage of the CFP process is due to the addition of catalyst iron in dissolved form to the system. In the MFP process, the iron supplied to the system in powder form must first dissolve in solution medium. Another reason for this result is that the Fenton process causes the ambient pH to decrease. This is mainly due to the low buffering capacity of the reaction medium. The iron sulfate heptahydrate used in the CFP process was acidic in character and the introduction of hydrogen ion into the medium during the rapid Fenton process caused the pH to decrease during the 1-hour reaction. In the MFP process, the iron powder used was neutral and the dissolution time of the reaction medium caused a negligible change in pH.

Strong acidic conditions are required in the reaction medium for oxidation to occur in the Fenton process. In the literature, the optimum pH range for the Fenton process is 3 - 4. When COD and surfactant removal efficiencies were examined in Fig. 1, a decrease in yield was observed in pH 2 in CFP process. This is due to the effect of OH• radical scavenging of the excess H^+ ions in the medium (Verma and Haritash, 2019). Other causes are the iron (II) hydroxide ($Fe(OH)^{2+}$) reacting more slowly with hydrogen peroxide and the conversion of hydrogen peroxide to the more stable $H_3O_2^+$ (Kwon et al., 1999). In the CFP process, the highest yield was obtained at pH 5 and slightly decreased at higher pH. This is due to the low buffering capacity and the pH of the reaction medium to 3.5 - 4 levels. In the original pH of grey water, 7.6, the yield decreased to 74% due to the radical scavenging effect of the excess OH• radical in the environment. In the MFP process, the catalyst solid iron must first dissolve. As the solubility of the iron decreased as the pH increased, the yield decreased with increasing pH. As a result, the optimum pH for CFP was 7.6, which was the original pH, and 2 for the MFP process.

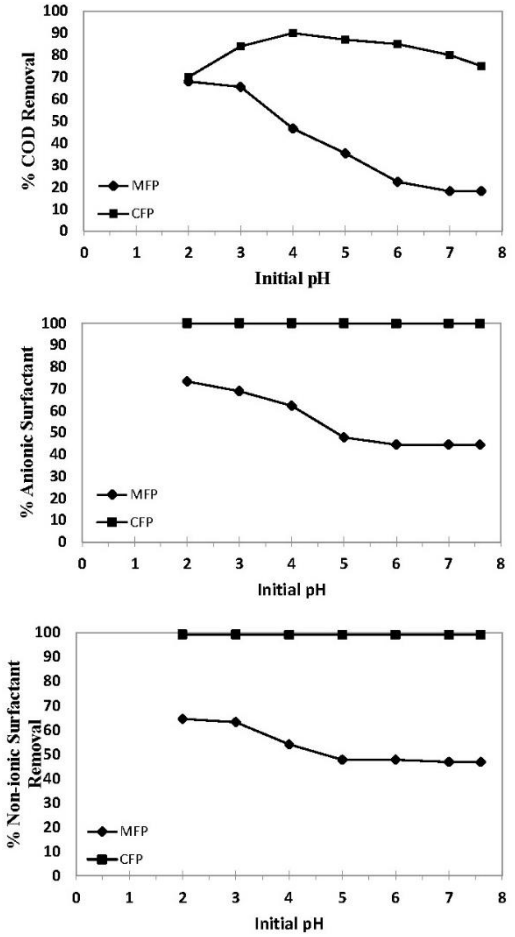

Fig. 1. Effects of initial pH on COD and surfactants

removals [Experimental conditions: [Fe^{2+}] = 100 mg/L and [H_2O_2] = 100 mg/L in CFP; [ZVI] = 100 mg/L and [H_2O_2] = 100 mg/L in MFP].

3.2. Effects of H_2O_2 Dosage on COD and Surfactants Removals

Optimization of H_2O_2 is crucial to both increasing the oxidation efficiency and reducing the cost of the Fenton process. Because the H_2O_2 used is the main source of OH• radicals produced in the system, its limited amount in the system will result in a decrease in efficiency. On the other hand, overdosing H_2O_2 into the system will also result in sweeping of the generated OH• radicals, reducing the yield and increasing the cost of treatment. In addition, the presence of residual H_2O_2 in treated water will lead to positive interference in COD analysis, leading to higher results (Şahinkaya, 2013).

H_2O_2 optimizations for CFP and MFP processes were performed at a constant iron concentration of 50 mg/L. Before the experiments, the initial pH was adjusted to 7.6 in the CFP process and the initial pH to 3 in the MFP process. Doses of H_2O_2 in both processes were examined in the range of 10 - 300 mg/L. As can be seen from Fig. 2, the removal efficiency increased rapidly when the H_2O_2 dose was increased up to 50 mg / L in both processes. In doses ranging from 50 to 200 mg / L, the yield was also negligible. In the CFP process, COD removal efficiency does not change at doses above 200 mg/L, while in the MFP process there is a slight decrease in yield due to the radical scavenging effect of excess H_2O_2 in the system (Eq. 4) (Zhang *et al.*, 2019). The oxidation of the CFP process was found to be much higher than the MFP. This is due to the fact that the type of iron supplied to the system is in dissolved form ready to react in the CFP process. The optimum H_2O_2 dose for both CFP and MFP processes was determined to be 50 mg/L. At this optimized dose, COD, anionic and non-ionic surfactant removal efficiencies were 76, 100 and 99, respectively, for the CFP process. For the MFP process, it was measured as 61, 85 and 97% respectively.

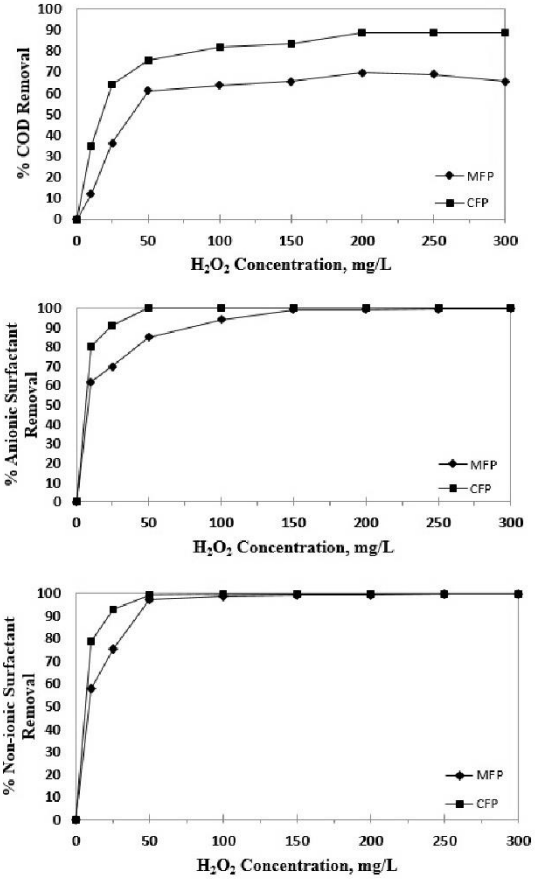

Fig. 2. Effects of H_2O_2 dosage on COD and surfactants removals [Experimental conditions: pH = 7.6 and [Fe^{2+}] = 50 mg/L in CFP; pH = 3 and [ZVI] = 50 mg/L in MFP].

3.3. Effects of Fe^{2+}/ZVI Dosage on COD and Surfactants Removals

Excessive usage of iron in the process will increase the operating cost. In addition, excess iron in the reaction mixture will have a radical scavenging effect (Eq. (2)), resulting in reduced oxidation efficiency. On the other hand, depending on the type and amount of iron used, the amount of chemical sludge resulting from the Fenton process is also increased. The sludge management increases the total cost of the process. Therefore, optimization of both type and amount of catalyst iron is very important for a feasible oxidation process.

In the experiments performed to optimize iron concentration in CFP and MFP processes, the dose of H_2O_2 was kept constant at 100 mg / L. Iron optimization studies were carried out at the original pH value of 7.6 and CFP process at 7.6 and MFP at pH 3. While iron sulfate heptahydrate was utilized as the catalyst iron source in the CFP process; ZVI was the catalyst iron in the MFP process. The amount of iron used in both processes was investigated in the range of 10 - 300 mg / L. Because anionic and non-ionic surfactants are readily degraded; process optimization was performed according to COD parameter. As seen from the experimental results presented in Figure 3, the increase in iron content in both processes led to a continuous improvement in COD removal. This is due to the reaction occurring in accordance with the reaction equation given in Eq. 1. In

the MFP process, since the ZVI had to first dissolve in the reaction medium, the reaction yield was lower than CFP. As a result, the optimum iron dose for both processes was 50 mg/L.

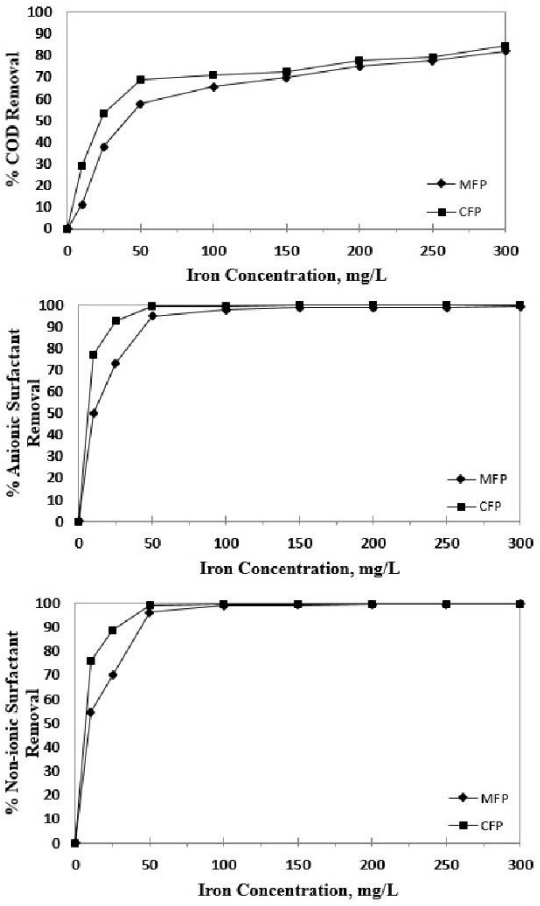

Fig. 3. Effects of Fe^{2+}/ZVI dosage on COD and surfactants removals [Experimental conditions: pH = 7.6 and $[H_2O_2]$ = 50 mg/L in CFP; pH = 3 and $[H_2O_2]$ = 50 mg/L in MFP].

3.4. Kinetic Study

Since COD, anionic (AS) and non-ionic surfactants (NS) are the most important pollutant parameters in the grey water, kinetic study was performed separately for all these parameters under the optimized conditions (summarized in Table 2).

Table 2. Optimum conditions and reaction efficiencies for CFP and MFP processes.

	pH	[Fe^{2+} / ZVI] mg/L	[H_2O_2] mg/L	Removal, %		
				COD	AS	NS
CFP	7.4	50	50	75	99.9	99.4
MFP	3	50	50	69	99.8	99.3

The experimental results are presented in Figures 4 and 5. As understood from these graphs, The CFP process completed the oxidation in a much shorter time than the MFP process. In the CFP process, it is understood that the reaction is carried out rapidly in accordance with Eq. 1 and completed in 1 minute. This was due to the fact that Fenton reagents were supplied ready to the reaction medium. Figure 4 shows that the reaction in the CFP process takes place in two stages: the rapid oxidation stage in the first 1 minute and the slow oxidation stage. In the CFP process, as the reaction was carried out rapidly in the first 1 minute and the reagents were depleted, the reaction continued for a further 59 minutes. In the MFP process, the reaction proceeded more slowly as the ZVI must first be dissolved in the reaction medium as shown in Eq. 5. On the other hand, removal within the first few minutes may have occurred on the surface of the ZVI in accordance with the reaction in Eq. 6.

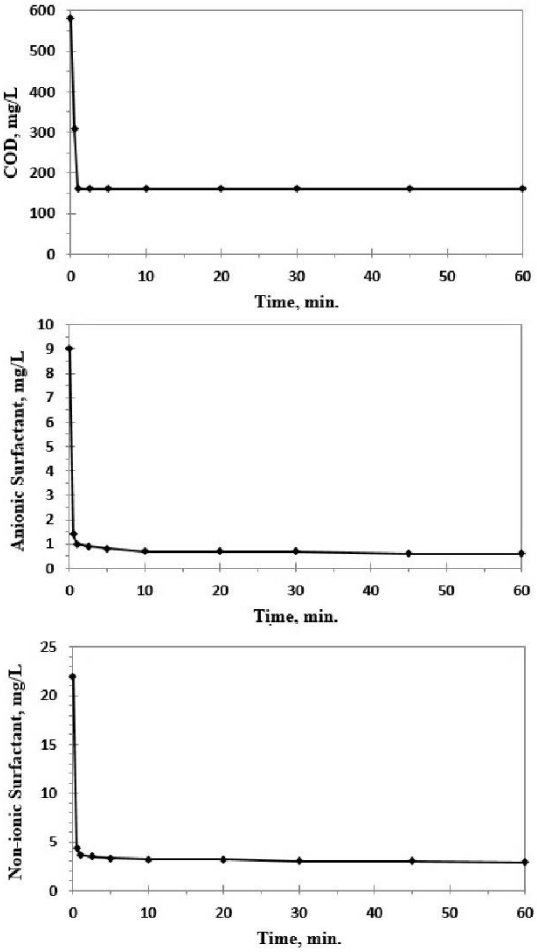

Fig. 4. COD and surfactant removal curves of CFP.

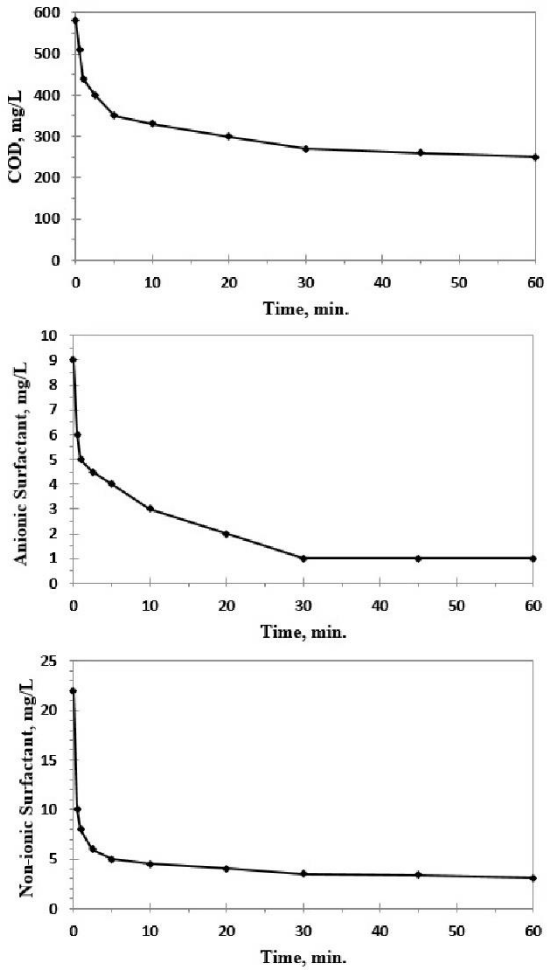

Fig. 5. COD and surfactant removal curves of MFP.

Experimental results presented in Eq. 4 and 5 are firstly applied to the basic kinetic models. But the results were found to be incompatible with the zero, first and second order kinetic models. Thus, a mathematical model kinetic model was used. The equation of this mathematical model is given in Eq. (8) and (9) (Behnajady *et al.*, 2007).

$$\frac{C}{Co} = 1 - \left(\frac{t}{m+bt}\right) \quad (8)$$

Where, C_0, is the initial concentration; C, is the concentration at time t; b and m are reaction kinetics and maximum oxidation capacity of the process, respectively. Eq. 8 is linearized to apply the model, and its linearized form is shown in Eq. 9.

$$\frac{t}{1-\left(\frac{C}{Co}\right)} = m + bt \quad (9)$$

According to Eq. 9, b, m and R^2 (determination coefficient) values obtained from kinetics data are summarized in Table 3. As seen in this table, high R^2 values demonstrated that the experimental kinetics data were in a perfect agreement with the kinetic model applied in this study. Moreover, according to this model, 1/m means the initial decay rate and the highest 1/m value is obtained in the CFP. Dimensionless constant b shows theoretical maximum removal fraction. As a result of the kinetic analyses, CFP is more rapid and effective process compared with MFP.

Table 3. Kinetic constants and R^2 values of the mathematical model.

Process	b	m	R^2
	COD Removal		
CFP	0.7252	0.058	1
MFP	0.5833	2.4885	0.998
	Anionic Surfactant Removal		
CFP	0.999	0.0015	1
MFP	0.9985	0.0161	1
	Nonionic Surfactant Removal		
CFP	0.995	0.0031	1
MFP	0.9946	0.0136	1

4. CONCLUSIONS

In this study, both CFP and MFP were experienced for the removal of COD, anionic and non-ionic surfactants from grey water. The main conclusions are obtained in the following;

- The influences of important operational conditions were experienced in both processes. Operating parameters were optimized as $[Fe^{2+}]$ = 50 mg/L, $[H_2O_2]$ = 50 mg/L and pH 7.6 that is the original pH value of the grey water in CFP, [ZVI] = 50 mg/L, $[H_2O_2]$ = 50 mg/L and pH 3 in MFP.
- pH adjustment is not required in CFP because of the rapid drop in the grey water pH after additions of the Fenton's reagents. On the other hand, since the modified Fenton process uses metallic iron powder in solid form, the pH adjustment to the acidic values is needed in order to solve the solid iron. The pH adjustment to the acidic values is required for the best yield in the modified Fenton process.
- It was seen that less the chemical treatment sludge was produced in MFP.
- The experimental data were fitted perfectly to the applied mathematical model. According to both the kinetic analyses and the applied model, CFP was more rapid and efficient process for the treatment of grey water because of the usage of ferrous ion as the catalyst, compared to the MFP.
- Both Fenton type processes can be used for the treatment of grey water in order to re-use in the water scarce regions.

REFERENCES

APHA/AWWA/WEF, 2005. In: Clesceri LS, Greenberg AE, Eaton AD. (Eds.), *Standard Methods for the Examination of Water and Wastewater*, 21st ed. American Public Health Association, American Water Works Association, and Water Environment Federation, Washing-ton, DC.

Bani-Melhem, K., Al-Qodah, Z., Al-Shannag, M., Qasaimeh, A., Qtaishat, M.R., Alkasrawi, M. (2015). "On the performance of real greywater treatment using a submerged membrane bioreac-tor system". *Journal of Membrane Science*, vol. 476: pp. 40-49.

Behnajady, M.A., Modirshahla, N., Ghanbary, F. (2007). "A kinetic model for the decolorization of C.I. acid yellow 23 by Fenton Process". *Journal of Hazardous Materials*, vol. 148, pp. 98–102.

Bergendahl, J.A., Thies, T.P. (2004). "Fenton's oxidation of MTBE with zero-valent iron". *Water Re-search*, vol. 38, pp. 327–334.

Bremner, D.H., Burgess, A.E., Houllemare, D., Namkung, K.C. (2006). "Phenol degradation using hydroxyl radicals generated from zero-valent iron and hydrogen peroxide". *Applied Catalysis B*, vol. 63, pp. 15–19.

Choi, Y.H., Son, S.U., Lee, S.S. (2004). "A micropump operating with chemically produced oxygen gas". *Sensors and Actuators A: Physical*, vol. 111, pp. 8–13.

Jaafarzadeh, N., Barzegar, G., Ghanbari, F. (2017) "Photo assisted electro-peroxone to degrade 2, 4-D herbicide: the effects of supporting electrolytes and determining mechanism". *Process Safety and Environmental Protection*, vol. 111, pp. 520–528.

Hossain, M.S. (2015). Domestic grey water treatment by Fenton's reagent for re-use in toilet flushing, M.Sc. Thesis. Bangladesh University of Engineering and Technology, Dhaka, Bangladesh.

Kwon, B.G., Lee, D.S., Kang, N., Yoon, J. (1999). "Characteristics of p-chlorophenol oxidation by Fen-ton's reagent". *Water Research*, vol. 33, pp. 2110-2118.

Özdemir, C., Öden, M.K., Şahinkaya, S., Güçlü, D. (2011). "The sonochemical decolorisation of textile azo dye CI Reactive Orange 127". *Coloration Technology*, vol. 127, pp. 268 - 273.

Pignatello, J.J., Oliveros, E., MacKay, A. (2006). "Advanced oxidation processes for organic contaminant destruction based on the Fenton reaction and related chemistry". *Critical Reviews in Environmental Science and Technology*, vol. 36, pp. 1-84

Şahinkaya, S. (2013). "COD and color removal from synthetic textile wastewater by ultrasound as-sisted electro-Fenton oxidation process". *Journal of Industrial and Engineering Chemistry*, vol. 19, pp. 601 – 605.

Thirugnanasambandhama, K., Sivakumar, V. (2015). "Optimization of treatment of grey wastewater using electro-Fenton technique – Modeling and validation". *Process Safety and Environmental Protection*, vol. 95, pp. 60–68.

Tony, M.A., Parker, H.L., Clark, J.H. (2016) "Treatment of laundrette wastewater using Starbon and Fenton's reagent". *Journal of Environmental Science and Health. Part A, Toxic/hazardous Sub-stances & Environmental Engineering*, vol. 51, pp. 974-979.

Verma, M., Haritash, A.K. (2019). "Degradation of amoxicillin by Fenton and Fenton-integrated hybrid oxidation processes". *Journal of Environmental Chemical Engineering*, vol. 7, pp. 102886.

Vorontsov, A.V. (2019). "Advancing Fenton and photo-Fenton water treatment through the catalyst design". *Journal of Hazardous Materials*, vol. 372: pp. 103–112.

Zhang, M., Dong, H., Zhao, L., Wang, D., Meng, D. (2019). "A review on Fenton process for organic wastewater treatment based on optimization perspective". *Science of the Total Environment*, vol. 670, pp.110–121.

Zhu, Y., Zhu, R., Xi, Y., Zhu, J., Zhu, G., He, H. "Strategies for enhancing the heterogeneous Fenton catalytic reactivity: A review". *Applied Catalysis B: Environmental*, vol. 255, pp. 1-16.

Turkish Journal of Engineering

Turkish Journal of Engineering (TUJE)
Vol. 5, Issue 2, pp. 80-86, April 2021
ISSN 2587-1366, Turkey
DOI 10.31127/tuje.679377
Research Article

AN APPLICATION TO ERROR AND UNCERTAINTY ANALYSIS IN INDUSTRIAL TYPE DRYER EXPERIMENTS

Ahmet Erhan AKAN*[1], Fatih ÜNAL[2]

[1] Tekirdag Namık Kemal University, Department of Machinery and Metal Technology, Tekirdag, Turkey
ORCID ID 0000-0003-1806-7943
aeakan@nku.edu.tr

[2] Mardin Artuklu University, Department of Machinery and Metal Technology, Mardin, Turkey
ORCID ID 0000-0001-6660-9984
fatihunal@artuklu.edu.tr

* Corresponding Author
Received: 23/01/2020 Accepted: 02/03/2020

ABSTRACT
In this study, information is given about the driers commonly used in the industry and the experimental errors and uncertainties that will be encountered in the experiments using these driers are tried to be explained by using the data obtained from the experiments carried out in an 8 chambers hot oil heated stenter, which is a conveyor type convection dryer. The fabric used in the experiments is the Thessaloniki type fabric, containing 67% cotton and 37% polyester. The experiments were carried out at a drying air temperature of 160 ºC and a fabric advance rate of 23 m/h (0.383 m/s). Thus, the example of error analysis in such experimental studies is provided and criteria that may cause an error for drying systems are discussed. As a result of the uncertainty analysis, the largest uncertainty in the system occurred in temperature measurements at ±0.367 - ±0.568 ºC values and the error rate for the whole system was found to be 4.08%. In terms of conducting the experiments in real production conditions and the materials and methods used in the experiments, this study is thought to will be help researchers that working on drying systems in their experimental studies.

Keywords: *Convection Dryer, Error Analysis, Uncertainty Analysis, Drying Test, Stenter*.

1. INTRODUCTION

Although drying is considered to be the removal of water or other liquids from gases, liquids or solids; the most common use is defined as the process of removing water or other volatile substances from solids utilizing thermal methods (Güngör et al., 1997). Factors such as material type, structure, ambient conditions, air quality, and speed of drying air are effective in drying processes (Akarslan, 2002). Drying is a complex process involving simultaneous heat, mass, and momentum transfer (Haghi et al., 2008). It is perhaps the oldest and most common method used by mankind to protect their food (Doymaz, 2004). Drying is known to facilitate the usage of the product, provide microbial protection and prolong the shelf life of the product (Koyuncu et al., 2007). However, the drying process is not limited to the food industry (Akan et al., 2015). It is an important process in the industrialized world in the chemical, agricultural, biotechnology, polymer, ceramic, perfumery, paper, mining, and wood industries. The use of hot air in the drying process, which is the most common, has caused these processes to be the most energy-consuming in the industry due to the high evaporation temperature and the inefficiency of the hot air used. While the drying process consumes a lot of energy, large amounts of CO_2 are released into the environment (Mujumbar, 2006). In many industrial enterprises, the energy consumed for drying has an important share in the total energy consumption of the establishment. This rate can reach 6% in chemistry, 5% in textile, 11% in ceramic and other construction materials production, 11% in timber drying, 12% in food and agricultural products, and 33% in the paper industry (Güngör, 2013). This makes it necessary to use drying systems as efficiently as possible. Therefore, it is inevitable that the drying systems are chosen for their purpose. Table 1 shows the energy consumed by the different types of dryers per unit of water removed from the material to be dried.

Table 1. Energy consumed per water removed from the product by dryer types (Güngör, 2013; Basaran, 2004).

Dryer Type	Evaporating water (MJ / kg)
Heat pump dryer	0.5 – 0.8
Direct exhaust gas dryer	3.2 – 3.8
Air-operated dryer between 70 - 100 ºC	4.5 – 5.5
Desiccant operating with exhaust gases from the boiler (400 ºC)	5.0 – 6.0
Desiccant operating with exhaust gases from the boiler (200 ºC)	9.0 – 12.0
Reverse flow, with Tray - Belt	8.0 – 16.0
Reverse flow, with Shelf - Tunnel	6.0 – 16.0
Cross-flow, with Tray-Band	5.0 – 12.0
Vacuum, with Tray - Belt - Plate	3.5 – 8.0

For the material to be dried, the following points should be considered in the selection of the drying method (Doğanay, 2009);
a- Drying behavior of the material to be dried: Amount of moisture before drying, type of moisture (bound water or unbound water), moisture content after drying, drying temperature, and drying time.
b- Properties of dry matter to be obtained: Particle size, concentration, moisture content, brittleness, etc. properties.
c- Processes related to drying operation: Continuous or batch drying preference, pre- or post-drying process requirement, drying time, drying temperature, position and movement in the dryer, and the capacity of the dryer.
d- Operating conditions of the dryer: The environment of the dryer, the dimensions of the dryer, thermodynamic properties and cleaning of the drying air, and vibration and noise of the dryer.

Accordingly, the drying methods used in the industry are presented in Table 2 (Doğanay, 2009).

Table 2. Drying methods

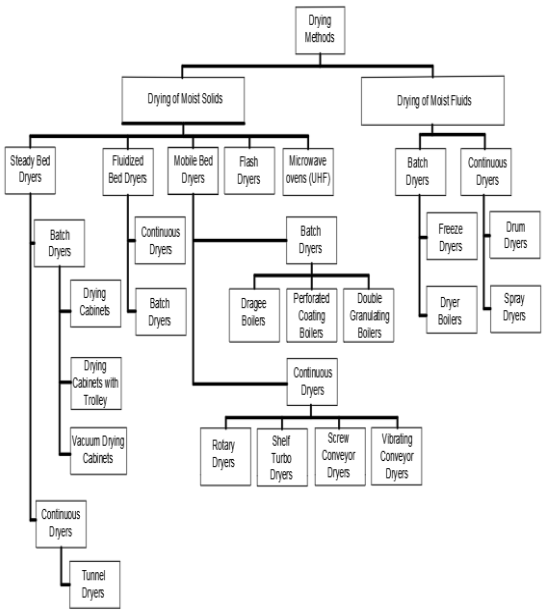

Experimental studies on the above-mentioned drying systems have always given researchers more precise and more accurate information than theoretical studies (Akpınar, 2006). However, the information obtained from the experimental studies also depends on the conducting of the experiment, the selection of measuring instruments, the calibration, and the reading of the obtained values. In general, such parameters that affect the accuracy of experimental data are called experimental errors. Another factor is the accuracy of the measuring instruments, which is called uncertainty. In general, two kinds of errors are encountered in the data obtained from the experiments. The first is the test set and measuring devices, and the second is the error caused by the person or persons experimenting. The first of these errors can be lowered by correctly calibrated test equipment with high sensitivity values and test devices established by standards, the latter can be reduced to the extent possible by the experience of the person performing the experiments, but completely accurate results still cannot be achieved. These error amplitudes are generally not known and are called errors in the literature (Akpınar, 2006; Midilli, 2001; Akpınar, 2002). It is also possible to divide the faults originating

from the so-called first type of errors, which are the test set and measuring devices into three main groups (Holman, 1971). The first is the errors caused by the manufacture of machinery, equipment, and devices used in the tests, the second is the fixed errors that occur during the re-reading of the same magnitude of unknown reason, and the third is the random errors caused by random electronic oscillations, friction, heat loss, etc. It is difficult to distinguish between many fixed errors and random errors (Akpınar, 2006; Holman, 1971). However, since the fixed errors are always read at the same values during the experiment, these errors can be corrected by using correctly calibrated test equipment.

Numerous experimental studies are possible in the literature. However, it is seen that it does not have an error analysis, which shows how accurate the experiment is in most of them. This study aims to present an example of error analysis in drying systems, especially for researchers working on drying systems.

2. MATERIALS AND METHOD

The experimental data obtained in this study were obtained from an 8-chamber hot oil heating ram machine used in a textile factory in Corlu/Tekirdağ (Akan et al., 2007). The schematic representation of the ram machine is presented in Figure 1. The fabric used in the experiments is the Thessaloniki type fabric, containing 67% cotton and 37% polyester. The dry weight of the fabric was kept at 20 ºC in 65% relative humidity (standard weather conditions) for 24 hours in the ELECTRO-MAG M3025P oven and the arithmetic average was determined as 320 gr/m^2, after which 5 samples taken from the fabric with DVT D100 circular sample cutter were measured with DESIS THB 600 precision scales. Before starting the tests, the fabric thickness was determined as 1.2 mm with the help of the TESTEX TF121 fabric thickness measuring device. Also, before the drying operation, the relative humidity of the fabric was determined as 80% with HYGRO FASTER EKV fabric moisture measuring device and the wet fabric weight was determined as 576 g/m^2 with the help of precision scales. The fabrics to be dried in the ram machine were washed in the foulard part before they enter the drying cabinets and were purified from unwanted foreign materials and subjected to the pre-drying process by crushing them between the rollers in the same part (Figure 1). After pre-drying, fabric surface temperature was measured as 30 ºC by using DIGITRON THERMAPRO 2 data logger with K Type Probe.

The experiments were carried out at a drying air temperature of 160 °C and a fabric advance rate of 23 m/d (0.383 m/s). The nozzles in each cabinet were selected from 3 nozzle units and the drying air velocity was measured as 35 m/s with the help of TESTO 350 M/XL portable gas analyzer. During the drying operation, the fabric surface temperatures were determined by DIGITRON THERMOPRO 2 data logger at the inlet and outlet points of each cabin, and the relative humidity and temperature values of the humid air around the boundary layer on the fabric were determined by DELTA OHM HD2301 humidity and temperature measuring device. Figure 2 shows the schematic representation of the measurement locations on the ram machine.

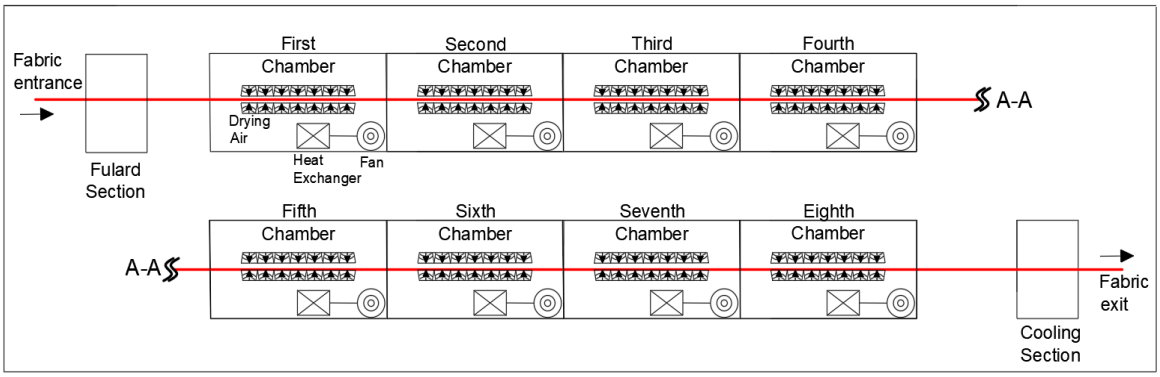

Fig. 1. Schematic representation of the ram machine.

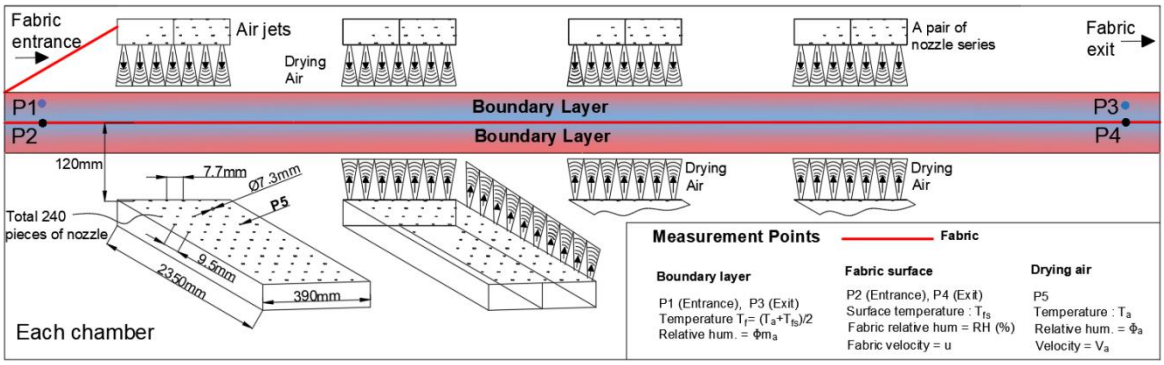

Fig. 2. Schematic representation of measuring points on the ram machine (Akan et al., 2019).

The measurement devices used during the experiments and their sensitivity are given in Table 3 and the values of the experimental data obtained are given in Table 4.

Table 3. Brands and accuracy values of measuring devices.

Measurement Devices Brands and Models	Sensitivity
TESTO 350M/XL, Portable gas analyser (Air velocity measurement)	5% (m/s)
HYGRO FASTER EKV (Fabric moisture measurement)	0.8% (RH)
DELTA OHM HD 2301 (Moist air, humidity – temperature)	0.1% (RH, °C)
HP475AC1R Model Probe (Moist air, humidity – temperature)	±1.5 - 3%[RH]
DIGITRON THERMAPRO 2 (K type probe, Fabric surface temp.)	0.5% (°C)
DESIS THB 600 Precision scales	0.01[g]
ELEKTRO-MAG M3025P (Drying-oven)	±1 °C
TESTEX TF121 (Fabric thickness measurement)	0.01 mm
DVT 100 (Circular sample cutter)	4% (cm^2)

3. ERROR AND UNCERTAINTY ANALYSIS

Assumptions made when determining experimental error analysis are given below:

* The test set-up was a dryer operating under actual production conditions established by the standards.
* The measuring devices were correctly calibrated.
* It was assumed that there were no errors in the production of measuring devices.
* The determined error values include both fixed errors and random errors.

According to this; the expression that gives the total error that may occur due to fixed errors, random errors and manufacturing errors that may occur in the measurement of the experiments can be written as in Equation 1 according to Kline and McClintock (Akpınar, 2006; Holman, 1971).

$$W_R = \left[\left(\frac{\partial R}{\partial_{x1}} w_1\right)^2 + \left(\frac{\partial R}{\partial_{x2}} w_2\right)^2 + \cdots \left(\frac{\partial R}{\partial_{xn}} w_n\right)^2\right]^{\frac{1}{2}} \quad (1)$$

or

$$\frac{W_R}{R} = \left[\left(\frac{w_{x1}}{x_1}\right)^2 + \left(\frac{w_{x2}}{x_2}\right)^2 + \cdots \left(\frac{w_{xn}}{x_n}\right)^2\right]^{1/2} \quad (2)$$

Table 4. Experimental data.

Measured values									Values
Dry fabric weight									320 [g/m^2]
Wet fabric weight									576 [g/m^2]
Wet fabric thickness									1.2 [mm]
Wet fabric dryer inlet temperature									30 [°C]
Wet fabric dryer input relative humidity									80% [RH]
Surrounding (environment) relative humidity									65% [RH]
Surrounding (environment) temperature									30 [°C]
Fabric feed rate									0.383 m/s
Drying air velocity									35 m/s
Drying air temperature									160 °C
Chamber	1	2	3	4	5	6	7	8	
	Entry-Exit	Entry-Exit	Entry-Exit	Entry-Exit	Entry-Exit	Entry-Exit	Entry-Exit	Entry-Exit	
Fabric relative humidity % [RH]	80-71	63-61	43-33	23-15	13-10	8-6	5-3	3-2	
Fabric outlet temperature (°C)	58.7	63.4	64.8	72.7	88.2	97.1	114.5	122.7	
Humidity of the circulating air (kg water / kg air)	0.074	0.102	0.107	0.067	0.049	0.025	0.015	0.009	

Here, R, x_1, $x_2 \ldots x_n$ is a given function of the independent variables, w_1, w_2, …, w_n is the uncertainty of the independent variables. The errors that can be made in the drying tests, considering the independent variables that may create the above-mentioned error, are given in Table 5 and the values of these errors are given in Table 6.

Table 5. Possible errors that can be made in drying experiments.

Error constituents parameters	Error	Symbol	Unit
Possible errors in fabric thickness measurement			
Error caused by the fabric thickness measurement	±0.01	W_{ft}	mm
Possible errors in circular sample cutter measurement			
Error caused by the circular sample cutter measurement	±0.04	W_{fct}	cm^2
Possible errors in temperature measurement			
Error caused by thermocouples	±0.25-0.50	W_{ther}	ºC
Error caused by connection elements and locations	±0.1	W_{cel}	ºC
Error that can be made in temperature measurement at dryer entry-exit points	±0.25	W_{tm}	ºC
Error that can be made to measure drying air nozzle output temperature	±0.01	W_{not}	ºC
Error in measuring moist air (exhaust) temperature	±0.01	W_{mat}	ºC
Error in measuring ambient air temperature	±0.01	W_{ait}	ºC
Error in measuring fabric surface temperature	±0.005	W_{fst}	ºC
Possible errors in the time measurement			
Error caused by the time meter	±0.1	W_{Tm}	s
Reader-induced error	±0.1	W_{trie}	s
Possible errors in the measurement of mass losses			
Error caused by precision scale	±0.01	W_{pc}	g
Reader-induced error	±0.01	W_{mrie}	g
Error caused by fabric	±0.25	W_f	g
Possible errors caused by velocity measurement			
Error caused by anemometer sensitivity	±0.05	W_{as}	m/s
Error caused by drying airflow leaks	±0.1	W_{fl}	m/s
Error caused by fabric speed settings	±0.015	W_{fss}	m/s
Possible errors in the relative humidity measurement			
Error caused by the sensitivity of thermohygrometer	±0.015-0.03	W_{hmst}	RH
Error caused by the placement of the thermohygrometer around the boundary layer	±0.1	W_{hbl}	RH
Reader-induced error	±0.1	W_{hrie}	RH
Possible errors that may occur in determination of fabric moisture content			
Error caused by the sensitivity of the moisture analyser	±0.008	W_{sma}	g
Reader-induced error	±0.001	W_{fmcrie}	g
Other errors			
Error from reading table values of physical properties	±0.1-0.2	W_{vpp}	%

The elements that may cause error shown in Table 5 were calculated with the help of Equation 1 and Table 6 was obtained.

Table 6. Errors that may occur in experiments.

Error constituents parameters	Total error	Unit
Possible errors in fabric thickness measurement	±0.01	mm
Possible errors in circular sample cutter measurement	±0.04	m^2
Possible errors in temperature measurement	±0.367 - ±0.568	ºC
Possible errors in the time measurement	±0.141	s
Possible errors in the measurement of mass losses	±0.250	g
Possible errors caused by velocity measurement	±0.112	m/s
Possible errors in the relative humidity measurement	±0.142 - ±0.147	RH
Possible errors that may occur in determination of fabric moisture content	±0.008	g
Other errors	±0.1-0.2	%

As can be seen from Table 6, the biggest uncertainties in the system can be detected immediately by using uncertainty analysis. This shows the superiority of uncertainty analysis. The greatest uncertainty in the system occurred at ± 0.367 - ± 0.568 ºC in temperature measurements. It can then be seen that the determination of the mass of water evaporated from the fabric occurs with an uncertainty value of ± 0.250 g. If the error value of the entire system is to be investigated, this result can be reached by using the values given in Table 7 and one of the equations given above.

Table 7. Parameters and sensitivities of measurement.

Parameter		Unit	Sensitivities	Measured min.-max. values	Measured average values
Velocity	Air	[m/s]	0.05	21.85-48.15	35
	Fabric		0.015	0.383	0.383
Temperature	Fabric	[°C]	0.005	27-152	89.5
	Drying air		0.01	152-168	160
	Moist air		0.01	52-102	77
	Environment		0.01	26.3-33.78	30
Relative Humidity	Moist air	%RH	0.015-0.03	59-61	60
	Environment		0.015-0.03	5.1-72	60
Moisture Content	Fabric	%RH	0.008	3.27-63	31.6
Weight	Fabric	[g]	0.01	300-550	425
Time	Fabric	[s]	0.5	60-66.98	62.66
Thickness	Fabric	[mm]	0.01	1.0-1.4	1.2
Square Measure	Fabric	[cm^2]	0.04	98-102	100

The error analysis of the whole system was found to be 4.08%. This value is among the acceptable values in the literature.

4. CONCLUSIONS

In this study, experimental error and uncertainty analysis of drying systems that are running on to give an example in order to researchers, 8 chambers hot oil heated convection type dryer machine which is a ram machine using the data obtained from the experiments, error and uncertainty analysis was conducted. In general, error elements that can be encountered in drying systems experiments have been discussed. As a result of uncertainty analysis, the largest uncertainty in the system occurred in temperature measurements with ± 0.367 - ± 0.568 °C values and error rate for the whole system was 4.08%. When determining the error rate, it was assumed that vulgar errors caused by personal errors or unexpected events such as making an arithmetic processing error or writing (-) instead of (+) did not occur. At the same time, the values of method errors, device and measurement device errors in the systematic error group were evaluated by taking into account the sensitivity values of the measurement devices used. It is inevitable that the total error rate will be reduced further by selecting those with more appropriate sensitivity values for the measurement devices used. On the other hand, the constant change of test conditions due to the conduct of experiments under actual production conditions has been seen to result in a large increase in the values of random errors caused by unknown, uncontrollable errors. As a result, it was concluded that experimental data closer to the actual values would be obtained when experimental conditions were kept under control and sensitivity values specific to the experiments were used by high-sensitivity devices.

REFERENCES

Akan A. E., Özkan D. B. (2019). "Experimental examination and theoretical modelling of drying behaviour in the ram machine." *Drying Technology*, Doi: 10.1080/07373937.2019.1662436.

Akan A. E., Özkan D. B. and Ünal F. (2015). "Energy and Exergy Analysis of Hot Oil Heated Convection Dryer." *ULIBTK'15 20. National Thermal Science and Technique Congress*, 02-5 September, Balıkesir, Turkey.

Akarslan, F. (2002). Effect of textile product properties on drying activity, Msc. Thesis, Institute of Science and Technology, University of Süleyman Demirel, Isparta, Turkey.

Akpınar E. K. (2002). Development of a Cyclone Type Dryer for Agricultural Products, PhD Thesis, University of Fırat, Elazığ, Turkey.

Akpinar, E. K. (2006). "An example of error analysis in experimental studies: error analysis in drying experiments.", *Engineer and Machine*, Vol. 46, No. 540, pp. 41-50.

Basaran, B., Bitlisli, B. O., Sari, Ö., Özbalta, N. and Güngör, A. (2004). "New technologies in leather drying: Heat Pump Dryers." *I. National Leather Symposium*, University of Ege, İzmir, Turkey. pp. 633-648.

Doğanay, T. (2009). Drying, *Modern Pharmaceutical Technology*, TEB Pharmacy Academy Publications, Ankara, Turkey.

Doymaz, I. (2004). "Drying kinetics of white mulberry." *Journal of Food Engineering*, Vol. 61, No. 3, pp.341-346.

Gügör, A., Özbalta, N. (1997). *Industrial drying systems*. III. National Installation Engineering Congress Proceedings Book, İzmir, Turkey.

Güngör A. (2013). "Dryers and Drying Technologies

Used in Vegetable and Fruit Drying." *11th National Installation Engineering Congress*, İzmir, Turkey, pp. 43-63.

Haghi, A. K., Amanifard, N. (2008). "Analysis of heat and mass transfer during microwave drying of food products." *Brazilian Journal of Chemical Engineering*, Vol. 25, No. 3, pp.491-501.

Holman J. P. (1971). *Experimental Methods for Engineers*, McGraw-Hill, New York, USA.

Koyuncu, T., Pinar, Y. and Lule, F. (2007). "Convective drying characteristics of azarolered (Crataegus monogyna Jacq.) and yellow (Crataegus aronia Bosc.) fruits." *Journal of Food Engineering*, Vol. 78, pp. 1471-1475.

Midilli A. (2001). Distillation of Wastewater by Natural Vacuum Technique, PhD Thesis, University of Karadeniz Technical, Trabzon, Turkey.

Mujumdar, A. S. (2006). *Hand book of industrial drying*. CRC Press, Lodz, Poland.

Turkish Journal of Engineering

Turkish Journal of Engineering (TUJE)
Vol. 5, Issue 2, pp. 87-94, April 2021
ISSN 2587-1366, Turkey
DOI 10.31127/tuje.693103
Research Article

HONEY FORMATION OPTIMIZATION: HFO

Zeki Yetgin *[1] and Mustafa Şamdan [2]

[1] Mersin University, Faculty of Engineering, Department of Computer Engineering, Mersin, Turkey
ORCID ID 0000 – 0001–5918 – 6565
zyetgin@mersin.edu.tr

[2] Mersin University, Faculty of Engineering, Information Technologies Research and Application Center, Mersin, Turkey
ORCID ID 0000 – 0003 – 4079 – 4565
msamdan@mersin.edu.tr

* Corresponding Author

Received: 23/02/2020 Accepted: 21/04/2020

ABSTRACT
In this paper, a new optimization framework, namely Honey Formation Optimization (HFO), is proposed. In contrary to the Artificial Bee Colony Optimization (ABC) variants in literature, the HFO considers food sources consisting of many components and model the honey formation inside bees as a process of mixing the components with their special enzymes during chewing up the food source. We believe that bees analyze the amounts of components inside the food source and attempt more to collect weaker (less amount) components to improve the honey formation process. Thus, each time a worker exploits a food source it selects a component in such a way that weaker components are more frequently selected. The approach requires decomposing the solution into components where each component is evaluated by a component fitness function. The honey formula maps the component fitness to honey amount and considered as the equivalence of the fitness function. The worker bee uses the fitness of the selected component to evaluate the food source and does local search only around the selected component. The HFO and ABC Frameworks are compared on the basis of 9 benchmark functions. The result shows that HFO performs better than the ABC.

Keywords: *ABC, bee colony algorithm, honey formation, function decomposition*

1. INTRODUCTION

Artificial Bee Colony (Karaboga 2005) is inspired by the intelligent behavior of honey bees. Scout, worker and onlooker bees form a colony and cooperatively search for food source positions. In ABC algorithm, scouts find initial positions of the food sources and then they are converted to workers. Workers exploit these sources and announce the information about them to onlooker bees in hive. Onlooker bees pay more visits to the better food sources and exploit them in the same way as workers do. Exploiting a food source means local search around the source and keeping track of the better food source. ABC algorithm has an increasing popularity in scientific community. It has been applied in solving many problems, such as image enhancement (Chen, Li & Yu 2017), compression(Ismail & Baskaran 2014), motion estimation (Cuevas et al. 2013), network attacks(Lozano et al. 2017), intrusion detection (Aldwairi, Khamayseh & Al-Masri 2015), training neural networks (Karaboga, Akay & Ozturk n.d.), feature selection (Keles & Kilic 2018), clustering(Karaboga & Ozturk 2011), and among many others(Akay & Karaboga 2015; Liu, Ma & Yang 2017; Apalak, Karaboga & Akay 2014; Abro & Mohamad-Saleh 2014; Kang, Li & Ma 2013). In literature, ABC algorithm is initially proposed for optimization of numeric functions (Karaboga 2005). Since then many ABC variants(Karaboga et al. 2014; Jia, Duan & Khan 2015; Huang, Wang & Yang 2016) have been proposed for various type of optimizations such as constrained, multi objective, continuous and combinatorial design problems. Karaboga and his friends provided a comprehensive survey (Karaboga et al. 2014) that analyses these problems with the focus on ABC drawbacks. According to the survey studies, the great potential of ABC seems very clear with its good exploration capability but also a strong need to alleviate the weakness in exploitation capability (local search).

Majority of the ABC versions in literature focus on the exploit phase (Gao & Liu 2012; Wang, Guo & Liu 2019; Han, Gong & Sun 2015; Shah et al. 2014; Cheng & Jiang 2012; He et al. 2015; Chen, Sarosh & Dong 2012; Kang, Li & Ma 2011),which improve the local search capability of bees (workers or onlookers). The original bees search around the current solution for a random neighbor towards to one of the existing solutions. Some articles (Gao & Liu 2012) (Shah et al. 2014) allow bees to search around the best solution of the current population. Although such approaches enable bees to converge the optimal solution very soon, they increases possibility of local stuck around the near optimal solution. Thus, (Gao & Liu 2012) also improves exploration ability of the scout bees by using chaotic and opposition based initialization(Sun, Chen & Zhang 2018) allows bees to search around a random existing solution for random neighbor towards to current solution, which is quite opposite of the original approach. Authors claim that this approach can expand the search range of new solution and further improve the exploration ability of ABC algorithm.

All the aforementioned ABC algorithms assume single component inside a food source and no honey formation inside bees. We considered that the honey formation starts when the bees chew up the food source, e.g. nectar, with their special enzymes and meanwhile they can analyze which components are needed to improve the quality of honey. The HFO Algorithm is actually a framework that can be applied to any ABC algorithms. It requires four major changes from existing ABC versions: i) solution decomposition into components where the component fitness function is composed from the cost function ii) honey formula mapping the component fitness to the solution fitness iii) a selection strategy for worker bees to select the weaker component randomly iv) applying local update only to the selected component. No change in onlooker phase is required. However optionally, instead of using fitness function, honey formula could still be used in onlooker phase. Also when the number of component is one, HFO becomes equal to original ABC algorithm.

The article is organized as follows. Next section provides the original ABC. Third section provides the proposed HFO algorithm. The fourth section provides the experimental results and the last section gives concluding remarks and future directions.

2. ABC ALGORITHM

The basic ABC algorithm requires few parameters, such as the number of food sources denoted as NS, maximum iterations denoted as *MaxIter*, and the *trial* limit denoted as *limit*. As given in Algorithm 1, the ABC algorithm has three phases. In first phase, scout bees randomly explore the food space to find initial food sources, which are the initial solutions denoted as X=($\boldsymbol{x_1}$, $\boldsymbol{x_2}$,…,$\boldsymbol{x_{NS}}$) and formulated in Eq. (1).

$$x_i(j) = x_{\min(j)} + rand(0,1).\left(x_{\min(j)} + x_{\max(j)}\right) \quad (1)$$

where $\boldsymbol{j}$ is the updating dimension $\in$ $\boldsymbol{\{1, 2,\ldots,D}$, $\boldsymbol{x_{min}}$ and $\boldsymbol{x_{max}}$ are upper and lower bound solutions respectively. Any scout discovering the food source, source $\boldsymbol{x_i} \in R^D$ becomes a worker bee with its associated food source in its memory. The bees measure the quality of the source $\boldsymbol{x_i}$ using the fitness function, formulated on basis of the cost function $\boldsymbol{f(x)}$ in Eq. (2).

$$fitx_i = fitness(x_i) = \begin{cases} 1/(1+f(x_i)), & f(x_i) > 0 \\ 1 + abs(f(x_i)), & f(x_i) \le 0 \end{cases} \quad (2)$$

In second phase, each worker $\boldsymbol{i}$ locally updates its food source $\boldsymbol{x_i}$ as a result of randomly searching its neighbourhood for a better solution. This phase is equivalent to local update procedure defined in Eq. (3-4), which forms a candidate $\boldsymbol{v_i} \in R^D$ by updating a randomly selected dimension j of the solution $\boldsymbol{x_i}$ towards one of the existing solution $\boldsymbol{x_k} \neq \boldsymbol{x_i}$ formulated in Eq. (3). The workers replace the source $\boldsymbol{x_i}$ with the candidate $\boldsymbol{v_i}$ if later is better, formulated in Eq. (4). Local update procedure also updates a trial counter. If worker $\boldsymbol{i}$ cannot (update) improve its current solution$\boldsymbol{x_i}$, the trial counter $\boldsymbol{c_i}$ will be incremented, otherwise the counter is reset to zero.

$$v_i(j) = x_i(j) + rand(-1,1).\left(x_i(j) - x_k(j)\right) \quad (3)$$

$$\begin{cases} x_i = v_i, \quad c_i = 0, & fitv_i > fitx_i \\ c_i = c_i + 1, & fitv_i \le fitx_i \end{cases} \quad (4)$$

where $k \in \{1, 2, \ldots, NS\}$ is the randomly chosen indice and $k \neq i$,$j \in \{1, 2, \ldots, D\}$ indicates a random dimension selected to be updated. In third phase, workers announce the information about the food sources such as nectar amount and position by dancing in the hive. Onlooker bees watch the dances of these bees and select a random food source among the sources in such a way that better sources have more chance to be selected.

Algorithm 1. Basic ABC Algorithm (MaxIter, NS, limit): return Best

(1) Generate random NS solutions (Eq. 1)
(2) for iter =1 to MaxIter do
(3) for each worker:
(4) - apply local update procedure to the associated solution of the worker (Eq. 3-4)
(5) P←selection probabilities of solutions proportional to their fitness values(Eq.2, 5)
(6) for each onlookers:
(7) - select a random solution according to selection probability P
(8) - apply local update procedure to it (Eq. 3-4)
(9) for each scouts:
(10) - replace the associated solution with a random solution if the solution is not I updated for limit iteration (Eq. 1)
(11) keep track of Best solution so far

The selection probabilities, $P = (p_1, p_2, \ldots, p_{NS})$, are formulated in Eq. (5) where p_i is the selection probability of the source x_i.

$$p_i = \frac{fitx_i}{\sum_{k=1}^{NS} fitx_k} \quad (5)$$

Then, they exploit their food sources in the same fashion as workers do (local update procedure). Thus, onlookers mostly gather around globally better solutions to make global improvements. All bees keep track of the best food sources during searching for the sources. Any bee that cannot exploit its food source (improve its solution) within some trial limit becomes scout again and finds a random food source throughout the space. The algorithm repeats worker-onlooker-scout phases until the maximum cycles are completed. When algorithm terminates one of the bees in current population is expected to have the best food source in its memory.

3. HFO FRAMEWORK

The proposed HFO framework is given in Algorithm 2 below. HFO generalizes the ABC algorithm where single component assumption equalizes the both. The main difference is that the HFO assumes food sources each consisting of K components and worker bees attempting more to search for components that are needed according to current honey form inside bees. Every food source $\boldsymbol{x_i}$ has its own honey form produced from it. Thus, the food source and its honey form are associated.

Algorithm 2. HFO Framework (MaxIter, NS, limit, K): return Best

(1) Generate random NS solutions (Eq.1)
(2) for iter =1 to MaxIter do
(3) for each worker:
(4) - P ← selection probabilities of components in current solution, inversely proportional to their component fitness (Eq. 8)
(5) - select a random component according to selection probability P
(6) - apply local update procedure to the selected component (Eq. 9-10)
(7) P← selection probabilities of solutions, proportional to their fitness (Eq. 5, 12)
(8) for each onlookers:
(9) - select a random solution according to selection probability P
(10) - apply local update procedure (Eq. 3, 11)
(11) for each scouts:
(12) - replace the associated solution with a random solution if the solution is not updated for limit iteration (Eq.1)
(13) keep track of Best solution so far

The honey form or equivalently the food source is considered as a solution and the components of the food source are sub solutions. The HFO finally finds the source that produce the best honey form. HFO uses cost-based approach: instead of using fitness, cost values are used when comparing solutions or components. The HFO defines three design concepts:

i) Component Design that require to decompose the solution into components where *c.* component of the solution x_i is denoted as $x_i{}^c$

ii) Component Fitness Design that deals with how to approximately measure each component fitness in a given solution. Normally, in HFO Framework, component fitness design is required for each component. However, the design of component and its fitness depends on the problem. Here, we assume original cost function f as component fitness functions where the fitness of the component $x_i{}^c$ is denoted as $fitx_i{}^c$ while its cost is denoted as $f(x_i{}^c)$

iii) Honey Formula Design (Optional): If the solution fitness can be expressed as function of component fitness such that this function shows equivalence / approximation to the original fitness function, then we call this function as Honey Function. If there is no way for Honey Function, one can use the original fitness function as Honey Function. One advantage of using honey function is that the solution cost is computed in terms of component cost values $f(x_i{}^c)$ that are already computed during local update procedure. This reduces the complexity of HFO.

One major form for component design is given in Eq. (6) where a solution $x_i \in R^D$ is decomposed into K non-overlapping sub solutions, causing a shift from the space R^D to $R^{D/K}$, with D/K as the dimension of components. Components are separated by pipe symbols in Eq. (6) just for visualization.

$$x_i = \left[\underline{x_{i1}}^1, \underline{x_{i2}}^1, \ldots \underline{x_{i(D/K)}}^1 \,\middle|\, \underline{x_{i(D/K+1)}}^2, \underline{x_{i(D/K+2)}}^2 \ldots \underline{x_{i(2D/K)}}^2 \,\middle|\, \ldots \right]$$
$$= \left[x_i^1 \,\middle|\, x_i^2 \,\middle|\, \ldots \right] \quad (6)$$

Among many forms of solution decomposition, following shows an overlapping form of components where half of each component is overlapped with the neighbor components.

$$x_i = [\ \underbrace{x_i^1 \quad \overbrace{x_i^2}}\ \ \underbrace{x_i^3}\ , \ldots] \tag{7}$$

The solution should be decomposed into components in such a way that the honey formula can bind the component fitness to the original fitness function.

According to HFO, the worker *i* evaluates the components of x_i and more probably modify (local update) the weaker component due to the fact that the component in less amount are more vital and more needed to improve the current honey form. Let $x_i{}^c \subseteq x_i$ be the *c.* component of x_i.The selection probability of component *c* for the worker ***i***, denoted as P_i^c, is inversely proportional to its fitness, formulated in Eq. (8) where the component cost $f(x_i{}^c) = cost x_i{}^c$ naturally measures the inverse fitness of the component *c* of x_i.

$$P_i^c = \left\{ \begin{array}{ll} \frac{f(x_i{}^c)+1}{\sum_{j=1}^{K}\left(f(x_i{}^j)+1\right)} & if\ f(x)\ is\ in\ positive\ domain \\ \\ \frac{f(x_i{}^c)-\min_{k=1..K}\left(f(x_i{}^k)\right)+1}{\sum_{j=1}^{K}\left(f(x_i{}^j)-\min_{k=1..K}\left(f(x_i{}^k)\right)+1\right)} & otherwise \end{array} \right\} \tag{8}$$

The local update procedure for worker bees is applied on component basis, which is formulated in Eq. (9-10) where *c* is the selected component and *j* is the updating dimension of the component *c* during local search around x_i. Note that the proposed local update procedure can be applied to any ABC variant not limited to Eq. (9-10). The idea here is the workers modifies the selected component according to their local search strategies.

$$v_i{}^c(j) = x_i{}^c(j) + rand(-1,1).\left(x_i{}^c(j) - x_k{}^c(j)\right) \tag{9}$$

$$\left\{ \begin{array}{ll} x_i = v_i, c_i = 0, & f(v_i{}^c) < f(x_i{}^c) \\ c_i = c_i + 1, & otherwise \end{array} \right\} \tag{10}$$

When comparing two solutions x_i and v_i in onlooker phase, we also prefer to use cost function rather than fitness function since the fitness definition in original ABC may cause implementation issue related to infinite precision requirement at the term 1/(1+cost). Thus, the local update procedure for onlooker is modified using Eq. (11) as follows

$$\left\{ \begin{array}{ll} x_i = v_i, c_i = 0, & F(v_i) < F(x_i) \\ c_i = c_i + 1, & otherwise \end{array} \right\} \tag{11}$$

where the $F(x)$ is the cost form of honey formula, formulated in Eq.(12). Honey formula F(x) is an approximation to the original cost function f(x) or must have equivalence relation with the f(x). Here as honey function we adapt summation operator.

$$F(x_i) = \sum_{c=1}^{K} f(x_i{}^c) \cong f(x_i) \tag{12}$$

The cost function approximation using the summation of component cost values are one form of honey formula, among many others.

The fitness form of honey formula $F_{fit}(x_i)$ is given in Eq.(13) that is only used in Eq.(14) to compute the selection probabilities p_i of solutions for onlookers.

$$F_{fit}(x_i) = \left\{ \begin{array}{ll} \frac{1}{F(x_i)+1} & if\ f(x)\ in\ positive\ domain \\ \frac{1}{F(x_i)-\min_{k=1..NS} F(x_k)+1} & otherwise \end{array} \right\} \tag{13}$$

$$p_i = \frac{F_{fit}(x_i)}{\sum_{k=1}^{NS} F_{fit}(x_k)} \tag{14}$$

HFO does not require any change in onlooker bees except using cost function f(x) when comparing two solutions. However, the approximated version of cost function F(x) could optionally be used to benefit from cost function decomposition. Cost functions may not be easily decomposed into component cost functions. Some cost functions are separable and easily expressed in terms of component costs. Thus, one can consider cost function approximation if it allows cost function decomposition on components.

3.1. Some Forms for Component Design

The component cost functions $f(x_i{}^c)$ and component itself $x_i{}^c$ must be considered together in design. Component design is problem specific and must be done for each benchmark functions. Here we propose some design strategies for component and its cost functions. Let the cost function f(x) expressed as f(x) = g(x) + h(x), 3 forms of component design are defined as follows:

1. Form: $x_i{}^c$ is non-overlapped and partition on f(x) as follows: $f(x_i{}^c) = g(x_i{}^c) + h(x_i{}^c)$

2. Form: $x_i{}^c$ is non-overlapped and partition on g(x) as follows: $f(x_i{}^c) = g(x_i{}^c) + h(x)/K$

3. Form: $x_i{}^c$ is overlapped and partition on f(x) as follows: $f(x_i{}^c) = g(x_i{}^c) + h(x_i{}^c)$

4. EXPERIMENTAL RESULTS

ABC and HFO algorithms are compared based on 9 benchmark functions given in Table 1. The benchmark functions have different characteristics such as multimodal and non-convex (Ackley, Qing, Egg-Crate, Xin-She Yan, Rosenbrock), multimodal and convex(Rastrigin), unimodal and non-convex(Griewank), unimodal and convex(Brown, Sphere). The functions are tested for the maximum number of iterations *MaxIter = 5000*, the number of food sources *NS=60*, the problem dimension *D=50*, and the parameter *limit=NS×D* and the number of components *K=10* for HFO.

However with this limit setting, the Rastrigin function is reached to global min zero for both ABC and HFO, thus the *limit = 0.1xNS x D* is considered only for Rastrigin function. The colony has equal number of worker bees and onlooker bees, considered equal to NS. Each experiment for the same parameter settings repeated 20 times and the average values are used to compute the performance metrics, such as min, max and mean of cost function values. The component design for each benchmark functions are provided in Table 3 where the details of component design is given in previous section.

Table 2. Typical benchmark functions

Name	Function	Range	Min
Ackley	$f_1 = -20exp(-0.2\sqrt{\frac{1}{n}\sum_{i=1}^{n} x_i^2}) - exp(\frac{1}{n}\sum_{i=1}^{n} cos(2\pi x_i)) + 20 + e$	(−32.768, 32.768)	0
Brown	$f_2 = \sum_{i=1}^{n-1} (x_i^2)^{(x_{i+1}^2+1)} + (x_{i+1}^2)^{(x_i^2+1)}$	(−4, 4)	0
Griewank	$f_3 = 1 + \sum_{i=1}^{n} \frac{x_i^2}{4000} - \prod_{i=1}^{n} cos(\frac{x_i}{\sqrt{i}})$	(−600, 600)	0
Qing	$f_4 = \sum_{i=1}^{n} (x_i^2 - i)^2$	(−10,10)	0
Rastrigin*	$f_5 = 10n + \sum_{i=1}^{n} (x_i^2 - 10cos(2\pi x_i))$	(-5.12, 5.12)	0
Sphere	$f_6 = \sum_{i=1}^{n} x_i^2$	(−100, 100)	0
Egg Crate	$f_7 = \sum_{i=1}^{n} x_i^2 + 25 \sum_{i=1}^{n} sin^2(x_i)$	(−500, 500)	0
Xin-SheYan	$f_8 = \left(\sum_{i=1}^{n} sin^2(x_i) - e^{-\sum_{i=1}^{n} x_i^2}\right) e^{-\sum_{i=1}^{n} sin^2\sqrt{\lvert x_i \rvert}}$	(−10,10)	-1
Rosenbrock	$f_9 = \sum_{i=1}^{n-1} [100(x_{i+1} - x_i^2)^2 + (1 - x_i)^2]$	(−50, 50)	0

Table 3. Component design for benchmark functions

Objective Functions	Component Overlapped	Component Cost Function Form#	Partition on g(x) or f(x)
Ackley	No	1	f(x)
Brown	Yes(1 element)	3	f(x)
Griewank	No	1	g(x)= $\sum_{i=1}^{n} \frac{x_i^2}{4000}$
Qing	No	1	f(x)
Rastrigin*	No	1	f(x)
Sphere	No	1	f(x)
EggCrate	No	2	g(x)= $\sum_{i=1}^{n} x_i^2$
Xin-SheYang	No	1	f(x)
Rosenbrock	Yes(1 element)	3	f(x)

The experimental results are provided in Table 4 and Figs. 1-9 where the table demonstrates the comparison of the objective performances with achieved min, max and mean cost values and the figures show the evolution curves of ABC and HFO. The Table 4 clearly shows that HFO is superior to original ABC for all functions. Particularly, for unimodal and convex problems the HFO performs best. However, for many difficult functions such as Rosenbrock, Egg-Crate, and Xin-She Yan that are multimodal and non-convex the HFO also performs well.

The evolution curves of mean cost values across the iterations are given in Figs. 1-9. The figures clearly show that the HFO converge speed is also better than ABC. The ABC sometimes early converges to a mean cost value around 1.0e-16 due to its weak local search strategy. With ABC local search, the solution is randomly updated and this causes improvement in less speed. HFO causes more correct solution update by updating only the worse component of the moment.

For each benchmark functions the behaviors of ABC and HFO varies. In general, ABC early maturates for all functions except Ackley where HFO performs better but converged earlier than ABC. Looking the Figure 1, around the iteration 3800-4000 HFO becomes saturated, however, ABC continue to improve. Due to early maturation for Ackley, all solutions in the population have sufficient time to reach the best value. Thus, the best and worst values are converged to each other for Ackley.

Table 4.Performance comparison : ABC versus HFO

Objective Functions	ABC			HFO		
	Best	Mean	Worst	Best	Mean	Worst
Ackley	5.1e-14	6.3e-14	6.8e-14	8.0e-15	**8.0e-15**	8.0-15
Brown	7.5e-16	9.6e-16	1.2e-15	9.4e-48	**3.2e-47**	1.1e-46
Griewank	0	9.4e-17	1.1e-16	0	**0**	0
Qing	9.6e-16	2.7e-15	1.3e-14	2.3e-17	**7.1e-16**	7.2e-15
Rastrigin*	0	2.3e-14	1.1e-13	0	**0**	0
Sphere	7.7e-16	9.4e-16	1.1e-15	2.8e-44	**1.7e-43**	4.1e-43
EggCrate	6.5e-16	7.9e-16	9.9e-16	1.1e-34	**5.8e-34**	2.7e-34
Xin-SheYang	7.7e-17	9.7e-17	1.1e-16	3.5e-37	**5.6e-33**	3.1e-32
Rosenbrock	0.5e-02	0.2	0.8	2.2e-06	**1.2e-05**	4.4e-05

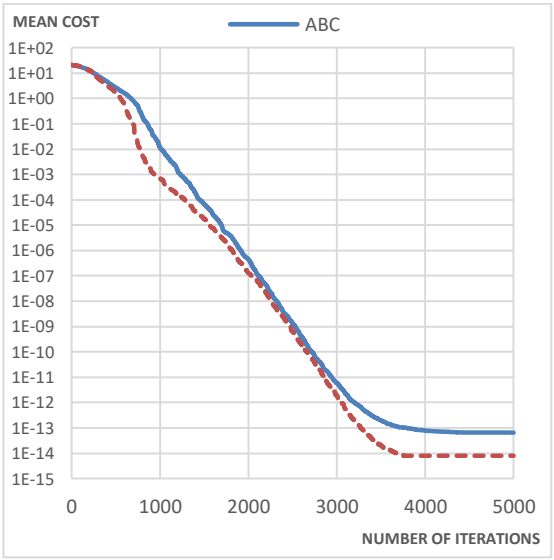

Fig. 1. Evolution curves for Ackley

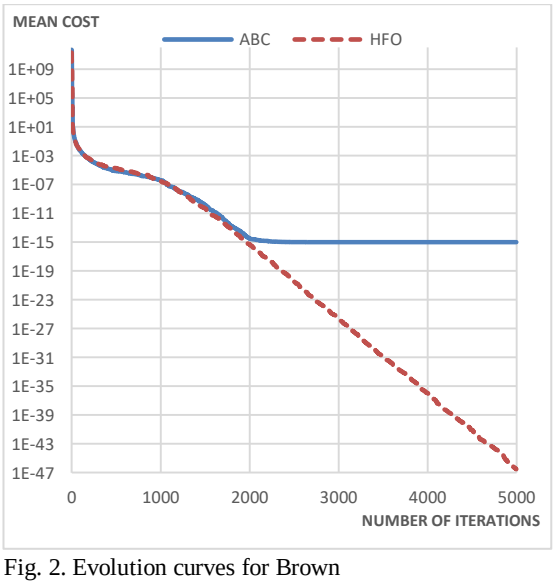

Fig. 2. Evolution curves for Brown

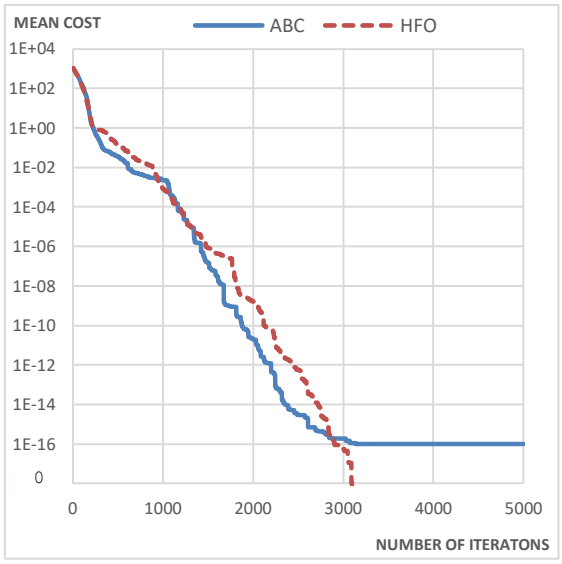

Fig. 3. Evolution curves for Griewank

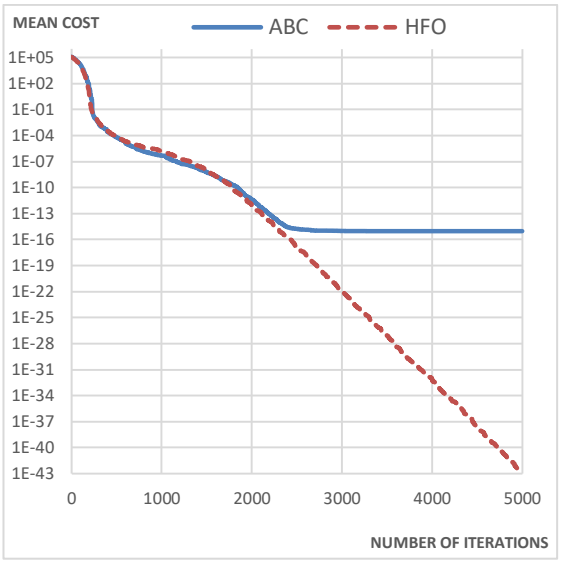

Fig. 6. Evolution curves for Sphere

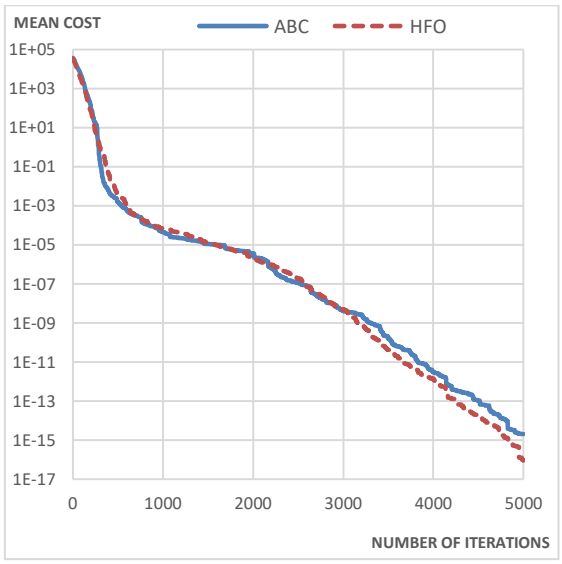

Fig. 4. Evolution curves for Qing

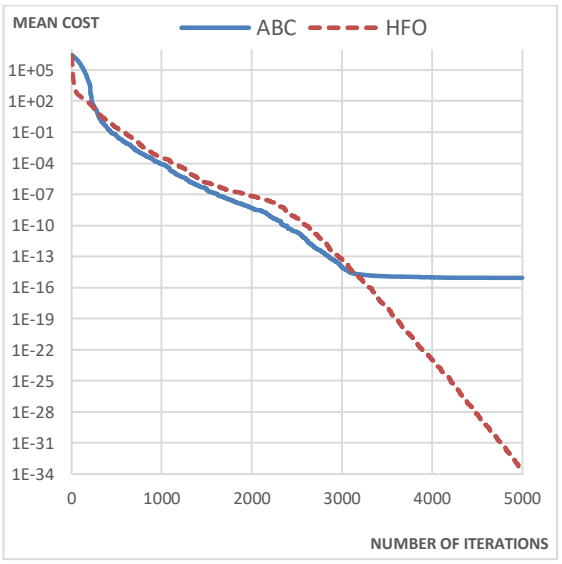

Fig. 7. Evolution curves for Egg Crate

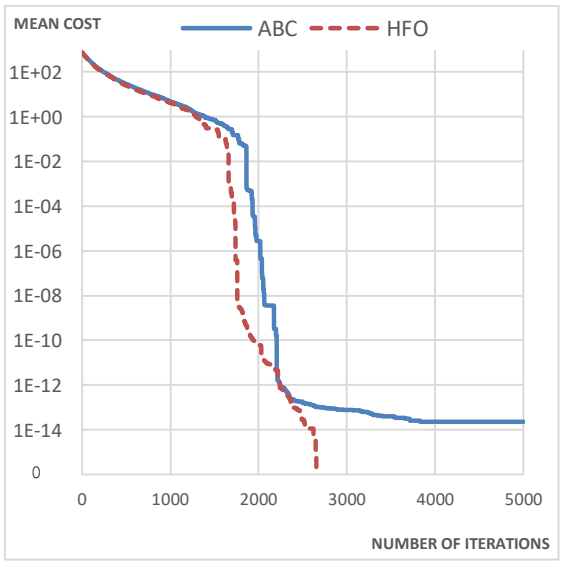

Fig. 5. Evolution curves for Rastrigin

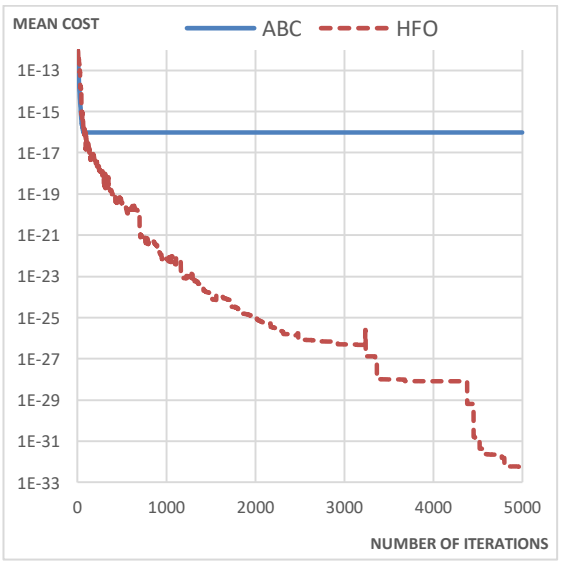

Fig. 8. Evolution curves for Xin-SheYang

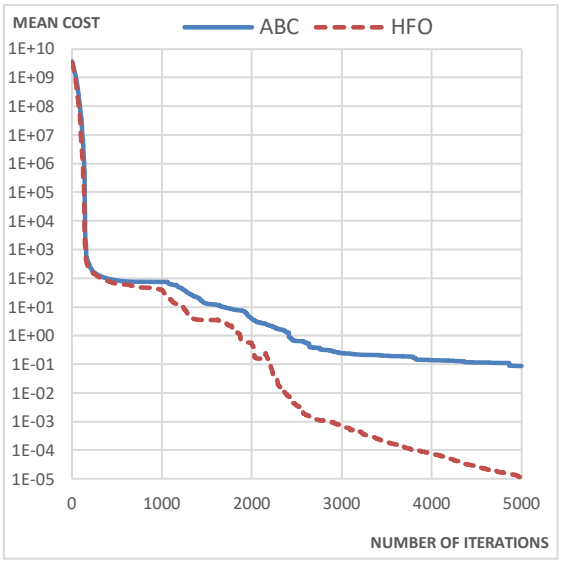

Fig. 9. Evolution curves for Rosenbrock

The Figure 3 and Figure 5 shows similar behaviors where there is a limit around 1e-15 and 1e-17 for Griewank and Rastrigin respectively and exceeding the limit causes their converge to zero. Another reason for similar behavior for both function is their similar function definitions where $\boldsymbol{g(x)} = \sum_{i=1}^{n}(x_i^2/4000)$ and $h(x) = 1 - \prod cos(xi/\sqrt{i})$ are used for Griewank function where h(x) is defined in terms of cosine function and g(x) and h(x) could be zero. When we look at the Rastrigin where $g(x) = \sum_{i=1}^{n}(x_i^2)$ and $\boldsymbol{h(x)} = 10n - \sum_{i=1}^{n} 10cos(2\pi x_i)$ could be considered, h(x) is again defined in terms of cosine function, and g(x) and h(x) could be zero. Rastrigin seems simple for both ABC and HFO. ABC is also reaching to zero with normal limit parameter. Thus, we reduced the limit L for only Rastrigin.

5. CONCLUSION

In this article, a new optimization framework namely Honey Formation Optimization (HFO) is introduced. HFO extends the Artificial Bee Colony Algorithm by considering multiple components in food sources and worker bees searching more frequently for the components in less amount due to fact that the component in less amount more limits the honey formation process and thus more vital for worker bees. For single component assumption, HFO and ABC become equal. The proposed optimization is a framework that could be applied to any ABC variant. The components are considered as sub solutions and honey formation process mix up the components towards better honey fitness. The experimental results demonstrates that HFO can performs better and converge earlier than the ABC. However, HFO uses honey formula that requires design for both solution decomposition and cost function decomposition together. Thus, some functions are difficult or even impossible to decompose perfectly. In such cases new approaches are required to partition functions on the basis of component design.

REFERENCES

Abro, AG & Mohamad-Saleh, J (2014), "Enhanced probability-selection artificial bee colony algorithm for economic load dispatch: A comprehensive analysis", *Engineering Optimization*, Vol. 46, No. 10, pp. 1315–1330.

Akay, B & Karaboga, D (2015), "A survey on the applications of artificial bee colony in signal, image, and video processing", *Signal, Image and Video Processing*, vol. 9, pp. 967–990.

Aldwairi, M, Khamayseh, Y & Al-Masri, M (2015), "Application of artificial bee colony for intrusion detection systems", *Security and Communication Networks*, Vol. 8, No. 16, pp. 2730–2740.

Apalak, MK, Karaboga, D & Akay, B (2014), "The Artificial Bee Colony algorithm in layer optimization for the maximum fundamental frequency of symmetrical laminated composite plates", *Engineering Optimization*, Vol. 46, No. 3, pp. 420–437.

Chen, J, Li, C & Yu, W (2017), "Adaptive Image Enhancement Based on Artificial Bee Colony Algorithm", *in Proceedings of the International Conference on Communication and Electronic Information Engineering (CEIE 2016)*, Atlantis Press, Paris, France.

Chen, S-M, Sarosh, A & Dong, Y-F (2012), "Simulated annealing based artificial bee colony algorithm for global numerical optimization", *Applied Mathematics and Computation*, Vol. 219, No. 8, pp. 3575–3589.

Cheng, X & Jiang, M (2012), "An Improved Artificial Bee Colony Algorithm Based on Gaussian Mutation and Chaos Disturbance", *in Springer*, Berlin, Heidelberg, pp. 326–333.

Cuevas, E, Zaldívar, D, Pérez-Cisneros, M, Sossa, H & Osuna, V (2013), "Block matching algorithm for motion estimation based on Artificial Bee Colony (ABC) ", *Applied Soft Computing*, Vol. 13, No. 6, pp. 3047–3059.
Gao, W & Liu, S (2012), "A modified artificial bee colony algorithm", *Computers & Operations Research*, Vol. 39, No. 3, pp. 687–697.

Han, YY, Gong, D & Sun, X (2015), "A discrete artificial bee colony algorithm incorporating differential evolution for the flow-shop scheduling problem with blocking", *Engineering Optimization*, Vol. 47, No. 7, pp. 927–946.

He, X, Wang, W, Jiang, J & Xu, L (2015), "An Improved Artificial Bee Colony Algorithm and Its Application to Multi-Objective Optimal Power Flow", *Energies*, Vol. 8, No. 4, pp. 2412–2437.

Huang, F, Wang, L & Yang, C (2016), "A new improved artificial bee colony algorithm for ship hull form optimization", *Engineering Optimization*, Vol. 48, No. 4, pp. 672–686.

Ismail, MM & Baskaran, K (2014), "Hybrid Lifting Based Image Compression Scheme Using Particle Swarm Optimization Algorithm and Artifical Bee Colony Algorithm".

Jia, D, Duan, X & Khan, MK (2015), "Modified artificial bee colony optimization with block perturbation strategy", *Engineering Optimization*, Vol. 47, No. 5, pp. 642–655.

Kang, F, Li, J & Ma, Z (2011), "Rosenbrock artificial bee colony algorithm for accurate global optimization of numerical functions", *Information Sciences*, Vol. 181, No. 16, pp. 3508–3531.

Kang, F, Li, J & Ma, Z (2013), "An artificial bee colony algorithm for locating the critical slip surface in slope stability analysis", *Engineering Optimization*, Vol. 45, No. 2, pp. 207–223.

Karaboga, D (2005), "An idea based on Honey Bee Swarm for Numerical Optimization", technical report-tr06, Erciyes university, engineering faculty, computer engineering department, vol. 200, pp. 1-10.

Karaboga, D, Akay, B & Ozturk, C "Artificial Bee Colony (ABC) Optimization Algorithm for Training Feed-Forward Neural Networks", *in Modeling Decisions for Artificial Intelligence*, Springer Berlin Heidelberg, Berlin, Heidelberg, pp. 318–329.

Karaboga, D, Gorkemli, B, Ozturk, C & Karaboga, N 2014, "A comprehensive survey: Artificial bee colony (ABC) algorithm and applications", *Artificial Intelligence Review*, Vol. 42, No. 1, pp. 21–57.

Karaboga, D & Ozturk, C (2011), "A novel clustering approach: Artificial Bee Colony (ABC) algorithm", *Applied Soft Computing*, Vol. 11, No. 1, pp. 652–657.

Keles, MK & Kilic, U (2018), "Artificial Bee Colony Algorithm for Feature Selection on SCADI Dataset", *in 2018 3rd International Conference on Computer Science and Engineering (UBMK)*, IEEE, pp. 463–466.

Liu, Y, Ma, L & Yang, G (2017), "A Survey of Artificial Bee Colony Algorithm", *in 2017 IEEE 7th Annual International Conference on CYBER Technology in Automation, Control, and Intelligent Systems (CYBER)*, IEEE, pp. 1510–1515.

Lozano, M, García-Martínez, C, Rodríguez, FJ & Trujillo, HM 2017, "Optimizing network attacks by artificial bee colony", *Information Sciences*, Vol. 377, pp. 30–50.

Shah, H, Herawan, T, Naseem, R & Ghazali, R (2014), "Hybrid guided artificial bee colony algorithm for numerical function optimization", *Lecture Notes in Computer Science (including subseries Lecture Notes in Artificial Intelligence and Lecture Notes in Bioinformatics)*, Vol. 8794, No. 7, pp. 197–206.

Sun, L, Chen, T & Zhang, Q (2018), "An Artificial Bee Colony Algorithm with Random Location Updating", Scientific Programming, Vol. 2018, pp. 1–9.

Wang, S, Guo, X & Liu, J (2019), "An efficient hybrid artificial bee colony algorithm for disassembly line balancing problem with sequence-dependent part removal times", *Engineering Optimization*, pp. 1–18.

Turkish Journal of Engineering

Turkish Journal of Engineering (TUJE)
Vol. 5, Issue 2, pp. 95-101, April 2021
ISSN 2587-1366, Turkey
DOI 10.31127/tuje.698856
Research Article

WIND POWER PLANT LAYOUT OPTIMIZATION USING PARTICLE SWARM OPTIMIZATION

İbrahim Çelik *[1], Ceyhun Yıldız [1] and Mustafa Şekkeli [2]

[1] Kahramanmaraş İstiklal University, Elbistan Vocational School, Department of Electricity, Kahramanmaraş, Turkey
ORCID ID 0000 – 0001 – 5923 – 554X
ibrahim.celik@istiklal.edu.tr

[2] Kahramanmaraş İstiklal University, Elbistan Vocational School, Department of Electricity, Kahramanmaraş, Turkey
ORCID ID 0000 – 0002 – 5498 – 4127
ceyhun.yildiz@istiklal.edu.tr

[3] Kahramanmaraş Sütçü İmam University, Engineering Faculty, Electrical and Electronics Engineering Department, Kahramanmaraş, Turkey
ORCID ID 0000 – 0002 – 1641 – 3243
msekkeli@ksu.edu.tr

* Corresponding Author
Received: 04/03/2020 Accepted: 08/04/2020

ABSTRACT
The use of wind energy has rapidly increased in recent years. In parallel with this rapid increase, Wind Power Plant (WPP) installation has become an important research topic. The selection of wind turbine location in WPP installation effects turbine output power. If the appropriate turbine position is not selected, the total generation of WPP is decreased. The purpose of this study was to determine the locations that wind turbines can achieve the highest energy generation. In this study, an optimization model was proposed to achieve the best WPP layout. In the first stage, field data and Wind Atlas Analysis and Application Program (WAsP) software were used to obtain wind speed distributions in the region where the WPP will be installed. . These distributions were used in the developed optimization model in MATLAB. The actual power curve of a wind turbine was used in the model to calculate energy generation. In the second stage, the locations of the wind turbine were determined by particle swarm optimization (PSO) method. In the final stage, the results of developed MATLAB model were compared with WASP to check accuracy. The difference between MATLAB model and WAsP software was found as 0.04%. This result showed that this model performed a calculation with acceptable accuracy. In addition, it was seen that wind turbines were located to the high wind velocity regions with the solution of the developed optimization model.

Keywords: *Micro-siting, Wind Power Plant, Particle Swarm Optimization, WAsP, Weibull distribution*

1. INTRODUCTION

In recent years, there has been a rapid development in the installation of wind power plants (WPP) all around the world. There has been a lot of studies about wind energy and WPP installation (Sekkeli et al., 2015a; Feng and Shen, 2015; Long and Zhang 2015; Sekkeli et al., 2015b; Karadöl et al., 2017; Abdelsalam and El-Shorbagy, 2018; Yang et al., 2019; Celik et al., 2019). Due to this rapid increase in WPP installation, wind turbines micro-siting has been an important research topic. Because turbine positions have an important effect on the output power of the wind turbines.

In literature, it is seen that wind turbine micro-siting has been considered as an optimization problem in WPP installation (Turner et al., 2014; Chen et al., 2015; Gao et al., 2015; Parada et al.,2017; Celik et al., 2018; Wang et al., 2018; Sun, Yang and Gao, 2019). Generally, in modeling studies to solve the optimization problem has been used to the theoretical wind speed -power curve (Mosetti, Poloni and Diviacco 1994; Grady, Hussaini and Abdullah, 2005; Marmidis, Lazarou and Pyrgioti, 2008; Wan et al., 2010; Kusiak and Song, 2010; Emami and Noghreh, 2010). Only a few studies have been used the experimental wind speed - power curve (Garcia et al., 2009; González et al.,2010; González et al.,2011; Pagnini et al.,2015). Also, the theoretical climate data has been used in models (Changshui, Guangdong and Jun, 2011; Chen et al., 2013; Brusca, Lanzafame and Messina, 2014; Yang et al., 2015; Chen et al., 2016).

In this study, an experimental turbine power curve was used to obtain more realistic results. Also, field data and industry standard WAsP software were used to develop optimization model. The analyzed WPP installation area was in southern region of Argentine. Wind speed and direction data were site measurements of installation area.

After modeling the wind distributions of WPP installation area and wind turbines power generations, the developed model was solved by using Particle Swarm Optimization (PSO). PSO method has been one of the most popular methods using to determine the location of the wind turbine (Pookpunt and Ongsakul, 2013; Hou et al.,2015; Pookpunt and Ongsakul, 2016; Song, Chen and Wang, 2018). This method provides the highest possible benefit from the wind energy.

This study aims to develop an optimization model for WPP installation. For this purpose, the optimization model was developed and solved in MATLAB environment. The solution of this model was obtained by the PSO method. This solution was the locations of the wind turbines, which could generate the highest power output. The detailed description of the model was given in Section 2. The PSO method was given in Section 3. Finally, the model outputs and WAsP outputs were compared to check the accuracy of the developed model.

The contribution of this study to the literature has been the use of the PSO, which is an effective method, with real field data and a real turbine power curve in WPP layout optimization.

This study consists of five sections. In the first section, the subject was generally explained. Also, used method and the summary of the literature was mentioned in this section. In the second section the theoretical background of the developed optimization model. In the section three, PSO method was described. In the fourth section, the field data and the wind turbine were presented. In the fifth section, the results of MATLAB model which was solved with the PSO method and the WAsP results of a commercial software were compared. In the last section, the results were evaluated.

2. THEORETICAL BACKGROUND OF OPTIMIZATION MODEL

In this study, an optimization model is developed to determine the highest generation locations of the wind turbines in a WPP installation. The constraints of model are given from the eq. (1) to (4). These constraints prevent to site the wind turbines to the same locations. The objective function is presented in eq. (5). In here, CRES and GRES represent the annual cost of a WPP and the annual total generation of a WPP.

$$\sqrt{\left(X_j - X_i\right)^2 + \left(Y_j - Y_i\right)^2} > 0 \tag{1}$$

$$1 \leq i \leq 10 \; \forall \, i \in N \tag{2}$$

$$1 \leq j \leq 10 \; \forall \, j \in N \tag{3}$$

$$i \neq j \;\; \forall \, j, i \in N^+ \tag{4}$$

$$f_{obj} = \left(\frac{G_{WPP}}{C_{WPP}}\right) \tag{5}$$

The objective function is aimed to maximize the annual total generation. The number of wind turbines is kept constant in the developed model. Therefore, only increasing the annual total generation is meaningful in the objective function

The annual total generation of WPP is calculated using eq. (6). In this equation, N_z is the number of the wind turbines. The cut in wind speed (V_{ci}) is the wind speed that the turbine begins to generate power. The cut-out wind speed (V_{co}) is maximum wind speed that the turbine can generate power. Besides, P (V_i) refers to wind turbine power curve. And f(V_i) is Weibull probability density function

$$G_{WPP} = \sum_{i=1}^{i=N_z} 8760 \left[\int_{V_{ci}}^{V_{co}} f(V_i) P(V_i) dv_i\right] \tag{6}$$

The 2-parameter Weibull probability density function is shown in eq. (7). The k and A are shape and scale parameters respectively (Celik et al., 2018). These parameters are obtained from WAsP software.

$$f(v_i) = (k/A)(v_i/A)^{k-1} e^{-\left(\frac{V_i}{A}\right)} \tag{7}$$

In this study, eq. 8 is used to calculate the annual cost of the WPP in objective function (Gao et al., 2015).

$$C_{WPP} = N_z \left(\frac{2}{3} + \frac{1}{3} e^{-0.00174 {N_z}^2}\right) \tag{8}$$

This developed optimization model is solved and optimum settlement locations for wind turbines are

found. PSO method is used in this study to solve the model.

3. PSO METHOD

PSO method, which inspired by the movement of the bird flocks, was developed by Kennedy and Eberhart in 1995. In this method, the initial population is created by random solutions. Then, to obtain the optimum solution this created population is updated from generation to generation. The stopping criteria of the search process is exceeding the number of generations. (Kennedy and Eberhart, 1995; Engelbrecht, 2005).

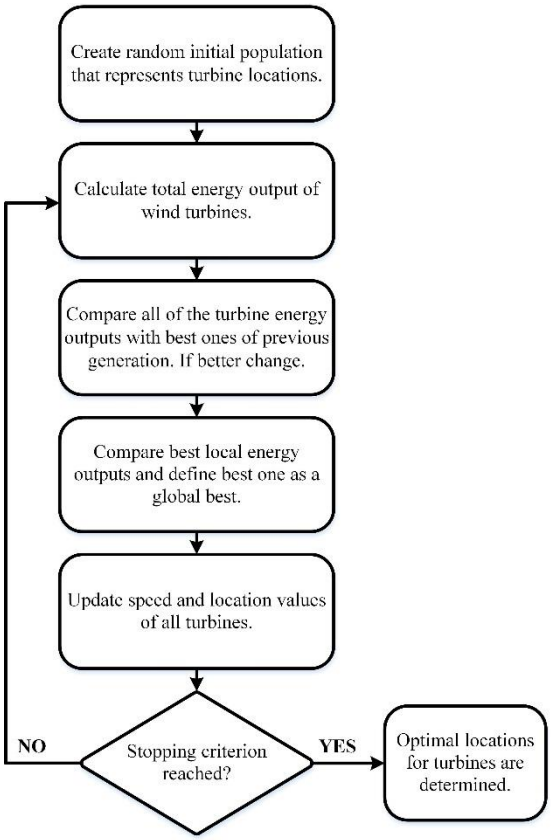

Fig. 1. PSO method operation steps.

The detailed explanation of the PSO method steps are given in Fig.1.

4. FIELD DATA AND WPP INSTALLATION AREA

The installation area of WPP is in the southern of Argentina. This area is shown in Fig. 2. The field data for this area are obtained from WAsP library. This field data are used in all calculations of the developed model.

Fig. 2. WPP installation area.

The average wind velocity map of the installation area is given at the Figure 3. This map is divided into 20 equal parts by accepting the horizontal axis (x) and the vertical axis (y). So, the number of 400 square area is obtained. Each center point of the square is a candidate wind turbine location. The distance between candidate locations is selected as 4 rotor diameters of the wind turbine. There should be an acceptable distance between the turbines which is equal to at least 4 times of the turbine rotor diameter. The wake effect is significantly decreased above this distance. So, the wake effect is negligible of in this study. This map is transferred to the MATLAB environment. The average wind velocity MATLAB map is given at the Fig. 4.

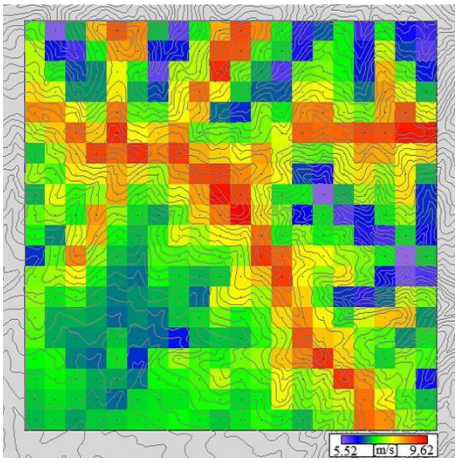

Fig. 3. The average wind velocity map of WAsP.

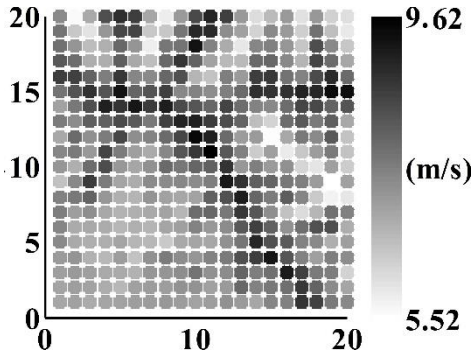

Fig. 4. The average wind velocity map of MATLAB.

In this model, the number of wind turbine is kept constant as equal to ten. Some characteristics of the wind

turbine are summarized in Table 1.

Table 1. Wind turbine characteristics

Brand	Vestas
Model	V-63
Hub height (m)	60
Rotor diameter (m)	63
Cut in wind speed (m/s)	4
Cut out wind speed (m/s)	25

Fig. 5. 1.5 MW wind turbine ("Wind turbine model", 2019).

General view of the turbine is as in Fig. 5. The nominal output power of each wind turbine is 1.5MW.

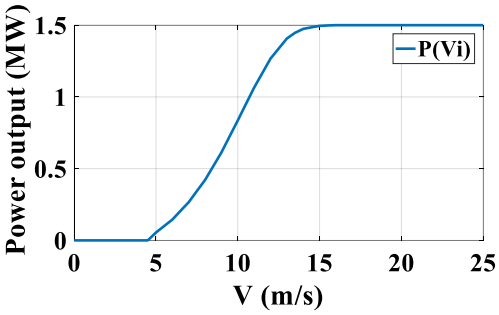

Fig. 6. Wind turbine power curve.

The power curve of the wind turbine is given in Fig. 6. This figure shows the correlation between wind speed and power output.

5. RESULTS

The developed optimization model is solved by the PSO method and the optimal wind turbine locations are determined.. Objective function of this model is division of C_{wpp} and G_{wpp}. C_{wpp} is constant because number of the wind turbine is assumed to be 10. So, the G_{wpp} directly effects the objective function value.

Power generation of first local best solution is find out as 56957 kWh. The annual power generation increase by iteration number is given in Fig.7. The wind turbine positions are given in Fig. 8. Second local best solution value is 57949 KWh. The wind turbine positions of this solution are given in Fig. 9. The annual power generation increase by iteration during the second solution process are given in Fig.10.

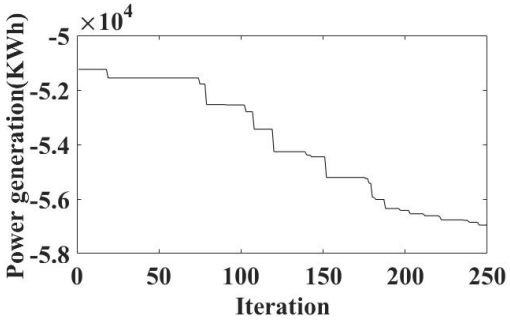

Fig. 7. First power generation increase by iteration number.

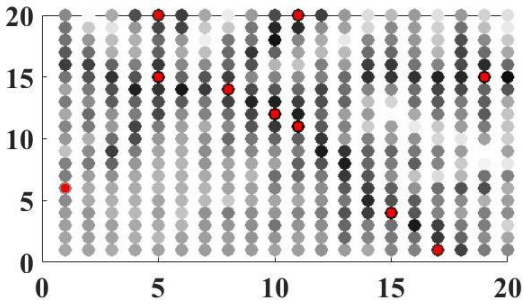

Fig. 8. First local best locations of the wind turbines.

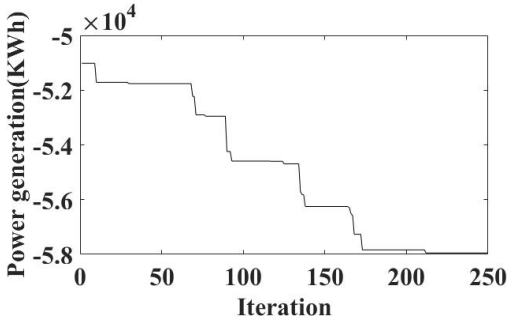

Fig.9. Second power generation increase by iteration number.

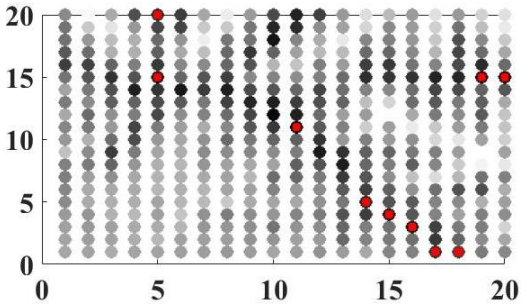

Fig. 10. Second local best locations of the wind turbines.

The global best power generation values for 150 populations and 250 iteration are shown in Fig. 7. Fig. 11. The optimal solution (wind turbine locations) are given in Table 2. The MATLAB model and WAsP power generation results for these locations are compared in

Table 3. Also, the layout of the wind turbines in average wind speed map of WAsP software and MATLAB model are given in Fig.12. and Fig. 13. respectively.

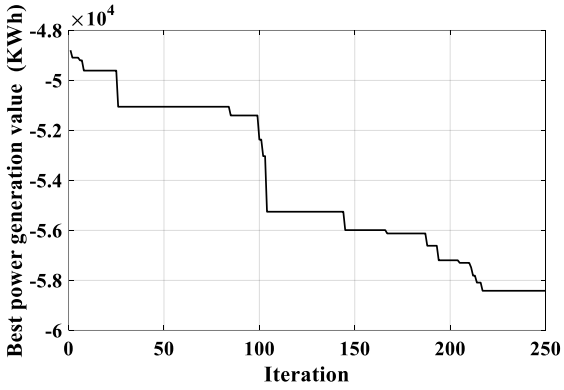

Fig. 11. Best power generations of the developed model.

Table 2. The locations of the wind turbines.

Axis	T1	T2	T3	T4	T5	T6	T7	T8	T9	T10
y	16	15	12	18	11	5	4	3	1	15
x	1	5	10	10	11	14	15	16	17	20

Table 3. The power generation results of the MATLAB model and WAsP model.

Turbine No	WASP (GWh)	MATLAB (GWh)	Error (%)
T1	5.125	5.152	0.52
T2	5.977	5.968	0.15
T3	6.184	6.205	0.34
T4	6.002	6.012	0.16
T5	6.296	6.272	0.38
T6	5.883	5.883	0.00
T7	5.737	5.764	0.47
T8	5.650	5.630	0.35
T9	5.498	5.471	0.49
T10	6.041	6.063	0.36
Total	58.393	58.420	0.04

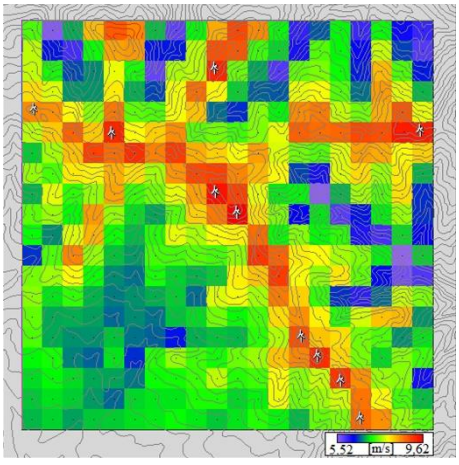

Figure 12. The layout of the wind turbines in average wind speed map of WAsP.

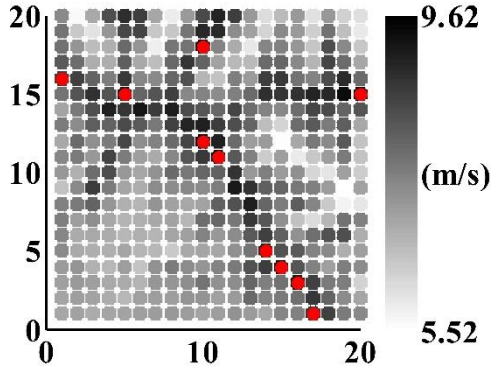

Figure 13. The layout of the wind turbines in average wind speed map of MATLAB model.

6. CONCLUSIONS

Wind turbine location selection is one of the most important subjects in WPP installation. In this study, the effect of settlement locations on wind turbine power output is examined. A WPP layout model is developed based on the relationship between the wind turbine settlement locations and total power output. The PSO method is used to obtain optimal solutions. The optimal locations are shown in Fig. 12 and Fig. 13. In this study, the wake effect is neglected. But wake effect loss of the obtained locations is determined for different best solutions in WAsP. This loss is maximum 0.64%. After that the global best solutions WAsP and MATLAB model results are compared in Table 3. These results showed that developed MATLAB model can calculate the annual power generation of the wind turbines. The maximum error is 0.52%. Also, there is a very small error (0.04%) in total power generation. Furthermore, the PSO method has shown good performance in the developed optimization model for WPP installation.

In this study, 10 wind turbines are tried to be sited in 400 settlement locations. Thus, the solution space is small. If WPP installation optimization is performed at a wide range of area with many of the wind turbines, the solution space will be big. In this case, it is thought that the developed model will gain importance in the WPP installation. Besides, the wind turbine output power is calculated with small errors in the developed model. By this means, it is possible to solve this optimization problem in MATLAB environment with different optimization methods.

REFERENCES

Abdelsalam, A.M., El-Shorbagy, M.A. (2018). "Optimization of wind turbines siting in a wind farm using genetic algorithm based local search", *Renewable Energy*, Vol. 123, pp. 748-755.

Brusca, S., Lanzafame, R., Messina, M. (2014). "Wind turbine placement optimization by means of the Monte Carlo simulation method". *Modelling and Simulation in Engineering*, Vol. 2014, pp. 1-8.

Celik, I., Yildiz, C. and Sekkeli,M. (2018) "An optimization model for wind turbine micro-siting in Wind Power Plant installation", *Gazi University Science*

Journal: PART:C, Vol. 6, No 4, pp. 898-908.

Celik, I., Yildiz, C. and Sekkeli,M. (2019) "Deniz üstü Rüzgâr Enerji Santrallerinde Rüzgâr Türbini Çıkış Gücü Hesabında Temel İz Etkisinin Değerlendirilmesi için Bir Model", *The Black Sea Journal of Science,* Vol. 1, pp. 1-9.

Changshui, Z., Guangdong, H., Jun, W., "A fast algorithm based on the sub- modular property for optimization of wind turbine positioning", *Renewable Energy,* Vol. 36, pp. 2951-2958, 2011.

Chen, Y., Li, H., Jin, K., Song, Q. (2013). "Wind farm layout optimization using genetic algorithm with different hub height wind turbines", *Energy Conversation Management*, Vol. 70, pp. 56-65.

Chen, Y., Li, H., He, B., Wang, P. (2015). "Multi-objective genetic algorithm based innovative wind farm layout optimization method.", *Energy Conversation* Management, Vol. 105, pp. 1318-1327.

Chen K, Song MX, Zhang X, Wang SF. (2016). "Wind turbine layout optimization with multiple hub height wind turbines using greedy algorithm", *Renewable Energy*, 96(676–686), (2016).

Emami, A., Noghreh, P. (2010). "New approach on optimization in placement of wind turbines within wind farm by genetic algorithms". *Renewable Energy,* Vol. 35, pp. 1559–64.

Engelbrecht, A.P. (2005). *Fundamentals of Computational Swarm Intelligence,* John Wiley & Sons, United Kingdom.

Feng, J., Shen, W.Z. (2015). "Solving the wind farm layout optimization problem using random search algorithm", *Renewable Energy*, Vol. 78, pp. 182–192.

Gao, X., Yang, H., Lin, L. Koo, P. (2015). "Wind turbine layout optimization using multi- population genetic algorithm and a case study in Hong Kong offshore", *Journal of Wind Engineering and Industrial Aerodynamics*, Vol. 139, pp. 89-99.

Garcia E., Gonzalez Rouco J.F., Jimenez P.A. (2009). "A comparison of methodologies for monthly wind energy estimation", *Wind Energy*, Vol.12, pp. 640–659.

González, J.S., Rodriguez, A. G., Mora, J. C., Santos, J. R., Payan, M. B. (2011). "Overall design optimization of wind farms". *Renewable Energy,* Vol. 36, pp. 1973–1982.

González, J.S., Rodriguez, A. G., Mora, J. C., Santos, J. R., Payan, M. B. (2010). "Optimization of wind farm turbines layout using an evolutive algorithm", *Renewable Energy*, Vol. 35, pp. 1671-1681.

Grady, S.A., Hussaini, M., Abdullah, M.M. (2005). "Placement of wind turbines using genetic algorithms", *Renewable Energy,* Vol. 30, pp. 259–270.

Hou, P., Hu, W., Soltani, M., Chen, Z. (2015). "Optimized Placement of Wind Turbines in Large-Scale Offshore Wind Farm using Particle Swarm Optimization Algorithm", *IEEE Transactions on Sustainable Energy*, Vol. 6, no. 4, pp. 1272 – 1282.

Karadöl, I., Keçecioğlu, O.F., Açıkgöz, H., Şekkeli, M. (2017). "Examination of Solar and Wind Energy Hybrid System for Kahramanmaraş Region," *KSÜ Mühendislik Bilimleri Dergisi*, Vol. 20, No. 2, pp. 89–96.

Kennedy, J. and Eberhart, R. C. (1995). "Particle Swarm Optimization", *Proc. of the IEEE Int. Conference on Neural Networks*, Piscataway, NJ, USA, pp. 1942-1948.

Kusiak, A., Song, Z. (2010) "Design of wind farm layout for maximum wind energy capture", *Renewable Energy*, Vol. 35, pp. 685-694.

Long, H., Zhang, Z. (2015) "A two-echelon wind farm layout planning model*," IEEE Trans. Sustain. Energy*, Vol. 6, No. 3, pp. 863-871.

Marmidis, G., Lazarou, S., Pyrgioti, E. (2008). "Optimal placement of wind turbines in a wind park using Monte Carlo simulation", *Renewable Energy*, Vol. 33, pp. 1455-1460.

Mosetti, G., Poloni, C., Diviacco, B. (1994). "Optimization of wind turbine positioning in large windfarms by means of a genetic algorithm", *Journal of Wind Engineering and Industrial Aerodynamics*, Vol. 51, pp. 105-116.

Pagnini, L. C., Burlando, M., Repetto M.P. (2015). "Experimental power curve of small-size wind turbines in turbulent urban environment", *Apllied Energy*, Vol. 154, pp. 112–121.

Parada, L., Herrera, C., Flores, P., Parada, V. (2017). "Wind farm layout optimization using a Gaussian-based wake model" ,*Renewable Energy*, Vol. 107, pp. 531–541.

Pookpunt, S., Ongsakul, W. (2016). "Design of optimal wind farm configuration using a binary particle swarm optimization at Huasai district, Southern Thailand", *Energy Conversion and Management*, Vol. 108, No. 2016, pp. 160-180.

Pookpunt, S., Ongsakul, W. (2013). "Optimal placement of wind turbines within wind farm using binary particle swarm optimization with timevarying acceleration coefficients," *Renewable Energy*, Vol. 55, pp. 266–276.

Sekkelı, M., Keçecioğlu, O.F., Açıkgöz, H., Yıldız, C. (2015a). "A Comparison between theoretically calculated and actually generated electrical powers of wind turbines: A case study in Belen wind farm, Turkey", *Academic Platform-Journal of Engineering and Science*, Vol. 1, pp. 41-47.

Sekkeli, M., Yildiz, C., Karik, F., Sözen, A. (2015b). "Wind Energy in Turkey Electricity Market". *Gazi Journal of Engineering Science*, Vol. 1, pp. 253-264.

Song, M. X., Chen, K., Wang, J. (2018). "Three-dimensional wind turbine positioning using Gaussian particle swarm optimization with differential evolution" ,

Journal of Wind Engineering Industrial Aerodynamics, Vol.172, No. 2018, pp. 317-324.

Sun, H., Yang, H., Gao, X. (2019) "Investigation into spacing restriction and layout optimization of wind farm with multiple types of wind turbines", *Energy*, Volume 168, pp. 637-650.

Turner, S.D.O., Romero, D. A., Zhang, P.Y., Amon, C.H., Chan, T.C.Y. (2014). "A new mathematical programming approach to optimize wind farm layouts", *Renewable Energy*, Vol. 63, pp. 674-680.

Wang, Y., Liu, H., Long, H., Zhang, Z., Yang S. (2018). "Differential Evolution with a New Encoding Mechanism for Optimizing Wind Farm Layout", *IEEE Transactıons on Industrıal Informatıcs*, Vol. 14, No. 3, pp. 1040-1054.

Wan, C., Wang, J., Yang, G., Zhang, X. (2010). "Optimal micro-siting of wind farms by particle swarm optimization", *Anonymous advances in swarm intelligence*. *Springer*, Vol. 2010, pp. 198–205.

Wind turbine model, https://en.wind-turbine-models.com/turbines/821-vestas-v63 (Accessed 19 Apr 2019).

Yang, K., Kwak, G., Cho, K., Huh, J. (2019). "Wind farm layout optimization for wake effect uniformity," *Energy*, Vol. 183(C), pp. 983-995.

Yang, J., Zhang R., Sun, Q., Zhang, H. (2015). "Optimal wind turbines micrositing in onshore wind farms using fuzzy genetic algorithm". *Mathematical Problems in Engineering*, Vol. 2015, pp. 1-9.

CONTENTS

ISSN 2587-1366

TURKISH JOURNAL OF ENGINEERING

VOLUME 5 ISSUE 2 APRIL 2021